AD-A255 667

░▌█▌░▌█▌▌▌░▌

②

PL-TR-92-2128

STUDIES IN SEISMIC VERIFICATION

Keith Priestley

S **DTIC**
ELECTE
AUG 2 0 1992
A **D**
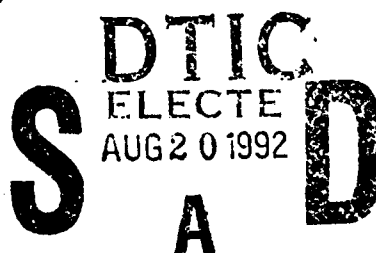
Seismology Laboratory
University of Nevada, Reno
Reno, NV 89557

5 May 1992

Final Report
1 July 1989-31 March 1992

92-23089
▌█▌█▌▌▌█▌▌█▌▌▌▌

92 8 19 016

The views and conclusions contained in this document are those of the authors and should not be interpreted as representing the official policies, either expressed or implied, of the Defense Advanced Research Projects Agency or the U.S. Government.

This technical report has been reviewed and is approved for publication.

JAMES F. LEWKOWICZ
Contract Manager
Solid Earth Geophysics Branch
Earth Sciences Division

JAMES F. LEWKOWICZ
Branch Chief
Solid Earth Geophysics Branch
Earth Sciences Division

DONALD H. ECKHARDT, Director
Earth Sciences Division

REPORT DOCUMENTATION PAGE

1. AGENCY USE ONLY (Leave blank)	2. REPORT DATE	3. REPORT TYPE AND DATES COVERED
	May 5, 1992	Final report (1 Jul 1989-31 Mar 1992)

4. TITLE AND SUBTITLE

Studies in Seismic Verification

5 FUNDING NUMBERS

Contract
F19628-89-K-0022
PE 61101E
PR 9A10 TA DA WU AM

6. AUTHOR(S)

Keith Priestley

7. PERFORMING ORGANIZATION NAME(S) AND ADDRESS(ES)

Seismology Laboratory
University of Nevada, Reno
Reno, Nv 89557

8. PERFORMING ORGANIZATION REPORT NUMBER

9. SPONSORING/MONITORING AGENCY NAME(S) AND ADDRESS(ES)

Phillips Laboratory
Hanscom AFB, Ma 01731-5000

Contract Manager: James Lewkowicz/GPEH

10. SPONSORING/MONITORING AGENCY REPORT NUMBER

PL-TR-92-2128

11. SUPPLEMENTARY NOTES

12a. DISTRIBUTION/AVAILABILITY STATEMENT

Approved for public release
Distribution unlimited

12b. DISTRIBUTION CODE

13. ABSTRACT (Maximum 200 words)

This report describes four related research efforts preformed under contract F19628-89-K-0022, section A reviews P-wave spectral models for earthquakes and explosions to assess their implications for high frequency seismic discrimination and test these on North American and central Asian data sets. Section B describes some simple forward modelling to quantify both the moment and mechanism of the tectonic release of the Soviet JVE. Using 10-20 sec surface wave data the tectonic release moment is found to be 10-20% of the explosion moments and have a strike-slip mechanism. Section C describes a new spectral model for seismic radiation of a circular crack failing in tension. Section D describes a study of the tectonics of the South Caspian region. Earthquake mechanisms show overthrusting of the South Caspian basin from the north, west and south. The combined effect will lead to the eventual destruction of the South Caspian Basin and the possible formation of intermediate depth seismic zone within the continental interior similar to the Hindu Kush.

14. SUBJECT TERMS

U.S.S.R., Kazakhstan, P-wave spectra, Tensile crack, Tectonic release, Caspian Sea

15. NUMBER OF PAGES

138

16. PRICE CODE

17. SECURITY CLASSIFICATION OF REPORT	18. SECURITY CLASSIFICATION OF THIS PAGE	19. SECURITY CLASSIFICATION OF ABSTRACT	20. LIMITATION OF ABSTRACT
unclassified	unclassified	unclassified	SAR

CONTENTS

TECHNICAL REPORT SUMMARY

Sections A-C describe the research forming the Ph.D dissertation of William R. Walter which was supported in part by contract F19628-89-K-0022. Section A (Walter and Priestley, 1991) reviews two of the most widely used P wave spectral models of earthquakes and two leading models of explosions, to assess their implications for high frequency (≥ 1 Hz) seismic discrimination of underground nuclear explosions from earthquakes. The models are then compared with North American events and a limited data set of Soviet Central Asian events. The earthquakes are consistent with a constant stress drop model which decays as ω^{-2} at high frequencies. The deeper (≥ 700 m) Nevada Test Site (NTS) explosions also show a ω^{-2} fall off between 10 and 30 Hz, in contrast with the shallower explosions which have a steeper decay. Near regional recordings of the September 14, 1988 Soviet JVE explosion show a higher corner frequency and lower 1 to 4 Hz P wave spectral ratios than predicted by either explosion model, and than predicted for similar size earthquakes. This high corner frequency may be influenced by source complications such as spall and tectonic release

Section B (Walter and Patton, 1990) describes some simple forward modeling to quantify both the moment and the mechanism of the tectonic release of the Soviet JVE. Using 10-20 second Love and Rayleigh wave data the tectonic release moment is found to be from one fifth to one tenth of the explosion moment. To resolve the ambiguity in tectonic mechanism, synthetics seismograms were computed to compare the relative amplitudes of the SH and SV parts of the SmS phase. Although the character of the SmS phases are not completely matched, the strike slip model proposed for the tectonic release comes closer to matching the observed relative amplitudes than the possible reverse faulting mechanism.

Section C (Walter and Brune, 1992) describes a spectral model for the seismic radiation of a circular crack failing in tension. The model may be a useful first approximation for modeling seismic sources with some volumetric component, such as magma injection, spall, or slip on a non-planar fault.

Section D (Priestley et al, 1992) describes a study of the tectonics of the region surrounding the South Caspian basin, a relatively aseismic block within the Alpine-Himalayan Belt, which is surrounded by zones of high seismicity. Earthquake focal mechanisms and depths were determined for 16 earthquakes in the region and these used to investigate the active tectonics. Earthquakes SW of the Caspian Sea have shallow thrust mechanisms showing that the continental crust of NW Iran is overthrusting the "oceanic-like" crust

1

of the south Caspian Basin. Both high angle reverse faulting and left-lateral strike slip faulting are observed south of the Caspian Sea in northern Iran. These mechanisms show oblique, left-lateral shortening and overthrusting of the south Caspian Basin by north-central Iran, but that this oblique regional convergence is partitioned into pure strike-slip and reverse faulting. Earthquakes east of the Caspian Sea also show a mixture of high angle reverse and strike-slip faulting mechanisms and thus may be another example of the partitioning of oblique slip into strike-slip and thrust motion. Normal faulting mechanisms dominate in the belt of seismicity which extends across the central Caspian Sea. It is improbable that these events represent the motion between the southern Caspian Basin and Eurasia for they imply a sense of motion which is incompatible with the observed topography and folding in the sediments. Two shallow earthquakes in this belt, one a small event and the other a large second event of a multiple earthquake, have thrusting mechanisms suggesting that shortening occurs as the continental crust of the northern Caspian is thrust over the "oceanic-like" crust of the southern Caspian Basin. Shortening is also suggested by the orientations of folds in the sedimentary cover south of the central Caspian Sea seismic belt. The normal faulting events appear to occur in the deep basement of the material being overthrust. We suggest that this shortening does indeed represent a NNE motion of the Caspian Sea relative to Eurasia, but that the motion is slow and has not produced many earthquakes. The combined effect of the overthrusting of the south Caspian Basin in the southwest and south, and north will lead to the eventual destruction of the south Caspian Basin and the possible formation of an intermediate depth, dipping seismic zone within the continental interior, similar to that presently observed in the Hindu Kush.

References

Priestley, K.F., C. Baker, and J.A. Jackson (1992). Active tectonics of the South Caspian basin and surrounding regions, *Geophysical J. Int.*, in review.

Walter, W.R., and H.J. Patton (1990). Tectonic release from the Soviet Joint Verification experiment, *Geophys. Res. Lett.*, *17*, 1517-1520.

Walter, W.R., and K.F. Priestley (1991). High frequency P wave spectra from earthquakes and explosions, AGU Geophysical Monograph 65, Explosion Source Phenomenology, 219-228.

Walter, W.R., and J.N. Brune (1992). The spectra of seismic radiation from a tensile crack, to be submitted to the *Journal of Geophysical Research*.

SECTION A

High-Frequency P Wave Spectra from Explosions and Earthquakes

William R. Walter and Keith F. Priestley

Seismological Laboratory, Mackay School of Mines, University of Nevada, Renu

Abstract

Two explosion P wave spectral models (Sharpe, 1942; Mueller-Murphy, 1971) and two earthquake P wave spectral models (Archambeau, 1968,1972; modified Brune 1970,1971) are reviewed to assess their implications for high frequency (> 1 Hz) seismic discrimination between earthquakes and explosions. The importance of the corner frequency scaling, particularly for models with the same high frequency spectral decay rate, is demonstrated by calculating source spectral ratios (a potentially important regional discriminant) for these models. We compare North American events and a limited data set of Central Asian events with these spectral models. We find North American earthquakes are consistent with a constant stress drop modified Brune model between 10 and 30 Hz. Shallow (< 700 m depth) Pahute Mesa explosions at the Nevada Test Site have a high frequency spectral decay between 10 and 30 Hz greater than the ω^{-2} predicted by the explosion models. Near regional recordings of the Soviet Joint Verification Experiment (JVE) explosion show a higher corner frequency and lower 1 to 4 Hz spectral ratios than predicted by either explosion model. The higher corner frequency of the Soviet JVE appears not to be due to attenuation, or receiver effects, and may represent a need for different corner frequency scaling, or result from source complications such as spall and tectonic release. A regional recording of the Soviet JVE (NEIC $m_b = 6.1$) is shown to have a lower 1 to 4 Hz spectral ratio than a smaller earthquake (NEIC $m_b = 4.6$) recorded on a nearly reciprocal path.

Introduction

The United States and the Soviet Union have been observing the terms of the Threshold Test Ban Treaty (TTBT) and the Peaceful Nuclear Explosion Treaty (PNET) since 1976. These treaties limit the maximum yield of underground nuclear testing to 150 kilotons (kt). Large explosions (>20kt) can be readily detected, and discriminated from earthquakes with seismic waves recorded at teleseismic (>3000 km) distances (cf. Dahlman and Israelson, 1978). Smaller explosions detonated under these treaties or under a future Comprehensive Test Ban Treaty (CTBT) or lower yield TTBT require detection and discrimination using regional (<3000 km) seismic data. Regional waveforms offer the potential of increased signal bandwidth for detection and identification, particularly at high (> 1 Hz) frequencies. Various studies (i.e. Pomeroy et al. 1982; Bennett and Murphy, 1986; and Taylor et al., 1989) suggest that spectral ratios of some regional phases hold promise for discrimination. However, as Taylor et al. (1989) note, "... a number of uncertainties regarding the lack of a physical

4

understanding of how the spectral discriminants work makes their utilization questionable at this point". Under a CTBT or lower yield TTBT there may be a need to detect and identify events from a geographic region in which we have little or no previous experience. In addition it will be necessary to understand under what circumstances a particular detection and identification method might fail. For these reasons it is important to develop a physical understanding of both the source and the propagation characteristics of regional waves.

Separating source and propagation effects can be difficult, particularly for high frequency waves. The observed seismic displacement amplitude spectra $\Omega(\omega)$ can be considered to be the product of a series of linear filters:

$$\Omega(\omega) = S(\omega) A(\omega) G(\omega) I(\omega) \tag{1.1}$$

where $S(\omega)$ is the source spectrum, $A(\omega)$ is the attenuation operator, $G(\omega)$ is the Earth's response, $I(\omega)$ is the instrument response, and $\omega = 2\pi f$ is the angular frequency. While $I(\omega)$ is easily determined, any attempt to uniquely isolate $S(\omega)$ is subject to limitations in our knowledge of $A(\omega)$ and $G(\omega)$. The attenuation operator is given as $A(\omega) = e^{-\omega t / 2 Q(\omega)}$ where t is the travel time and $Q(\omega)$ is a dimensionless measure of the energy lost in each seismic wavelength. In most regions $Q(\omega)$ has been found to be a constant or a slowly increasing function of frequency. At higher frequencies the effect of the attenuation operator becomes increasingly important, strongly trading off with estimates of the source spectral amplitude (cf. Anderson, 1986). Many high frequency (> 1 Hz) studies of P wave attenuation assume a particular form for the source spectrum and determine the attenuation by adjusting $Q(\omega)$ until the observed spectrum matches the assumed source spectrum (e.g. Der et al., 1985, Hough et al., 1988, Sereno et al., 1988). The Earth response $G(\omega)$ is also subject to more uncertainty at high frequencies since shorter wavelength signals are affected by small scale features in the Earth. $G(\omega)$ includes source region effects such as free surface reflections, geometrical spreading which may be frequency dependent for some regional phases (e.g. Sereno, 1990), scattering, and receiver site effects. Recent borehole studies at several hardrock sites have found that attenuation and resonance within a shallow weathered zone (typically tens of meters thick) can have a pronounced effect on observed high frequency P wave spectra (Malin et al., 1988; L. Carroll, J. Fletcher, H. Liu, and R. Porcella, unpublished data, 1990)

As a result of the difficulties of uniquely determining the source spectral amplitude, various models for both earthquakes and explosions have been proposed, each with different implications for the problems of seismic discrimination. For example, the Sharpe (1942) and Mueller-Murphy (1971) explosion source spectral models are richer in high frequency P waves than the Archambeau (1968, 1972) earthquake source spectral model, when normalized to have the same low frequency level. This was the basis for a proposal by Evernden et al., (1986) that the solution to the problem of detection and identification of low-yield underground nuclear explosions was available using high frequency P waves. However, if the Brune (1970) earthquake source spectral model modified for P waves (Molnar et al., 1973) is compared with these

explosion models the source spectral differences are much smaller.

In this paper we will first review these four competing spectral models and their implications for the seismic discrimination issue, then discuss efforts to distinguish between various earthquake and explosion P wave source spectral models using data from western North America. Finally we will compare those results with results from near regional (< 800 km) seismic data collected in the vicinity of the Soviet Union's East Kazakhstan Test Site (KTS). Although data for Central Asia is limited, we find significant differences in high frequency (≥ 1Hz) P wave spectra for Soviet explosions compared with both shallow explosion spectra observed at the Nevada Test Site (NTS) and from explosion spectral models based on North American experience.

Theoretical Models

Simple source spectra are typically characterized by three values: the low frequency asymptote whose level is proportional to the seismic moment (or source strength), the high frequency asymptote whose slope depends on the source displacement time history, and the intersection of these two asymptotes, the corner frequency, f_c, which is related to the source dimension. On a plot of log displacement amplitude versus log frequency the low frequency asymptote has a constant value. The high frequency asymptote is proportional to $\omega^{-\eta}$ where η must be greater than 1.5 to have finite energy. A larger η indicates a greater high frequency decay. Our discussion of spectra for various source models will be in terms of these three parameters.

The generation of seismic waves by an underground nuclear explosion is a complex phenomena. The explosion region can be conceptually modeled with increasing distance from the shot point as a vaporization cavity, a strongly non-linear region characterized by a shock wave, and a linear region (Rodean, 1971). Sharpe (1942) modeled the seismic waves from explosions as an arbitrary pressure function applied to the interior of a spherical surface at an "elastic radius", R_{el}, defined as the distance from the detonation point to the point at which the medium begins to respond linearly (elastically). In the Sharpe model all of the effects of the non-linear region: rock vaporization, cavity expansion, shock wave propagation and decay to an elastic wave, are contained in the form of the pressure function. Sharpe (1942) discussed several pressure histories, but we will follow Evernden et al. (1986), and use a step or Heaviside function in pressure acting at the elastic radius as the "Sharpe" model. The Sharpe far-field displacement amplitude spectrum is given by:

$$\Omega^P(\omega) = \frac{P_o R_{el}^3}{4 \mu R} \left[\frac{\alpha^2}{(\alpha^2 - 0.75 R_{el}^2 \omega^2)^2 + (\alpha R_{el} \omega)^2} \right]^{1/2} \qquad (1.2)$$

where P_o is the amplitude of the pressure step function, μ is the modulus of rigidity, α the P wave velocity, and R is the hypocentral distance. Evernden et al. (1986) give a relationship between the elastic radius and the yield as:

$$R_{el} = 1.61 \times 10^4 \left[\frac{k\,W}{P_o} \right]^{1/3} \quad \text{meters,} \tag{1.3}$$

where P_o is in pascals, k is a coupling constant and W is the explosion yield in kilotons. Evernden et al., (1986) give values of P_o = 20 MPa (200 bars), k = 9 for KTS and P_0 = 13 MPa (130 bars), k = 9.4 for NTS.

Mueller and Murphy (1971) modeled explosions with a different pressure function at the elastic radius. They used a pressure function based on free-field observations of several underground nuclear explosions. This pressure function has the form:

$$P(t) = (P_1 e^{-\gamma t} - P_2) H(t) \tag{1.4}$$

where P_1, P_2, and γ are functions of depth and the shot point geology which have been empirically determined from U.S. explosions. The far-field amplitude spectrum of this model is given by:

$$\Omega^P(\omega) = \frac{R_{el}^3}{4\mu R} \left[\frac{P_1^2 + 2P_1 P_2}{\gamma^2 + \omega^2} + \frac{P_2^2}{\omega^2} \right]^{1/2} \left[\frac{\alpha^2 \omega^2}{(\alpha^2 - 0.75 R_{el}^2 \omega^2)^2 + (\alpha R_{el} \omega)^2} \right]^{1/2} \tag{1.5}$$

If we assume a depth - yield scaling relationship appropriate for the NTS of h = 120 $W^{1/3}$ meters and a granitic medium, then the empirically determined parameters for this model are (Stevens and Day, 1985):

$$R_{el} \approx 2.38 \times 10^3 \frac{W^{1/3}}{h^{0.42}} \quad \text{meters,} \tag{1.6}$$

$$\gamma \approx 1.09 \times 10^4 \frac{1}{R_{el}} \quad \text{hertz,} \tag{1.7}$$

$$P_1 \approx 3.77 \times 10^4 h - P_2 \quad \text{pascals,} \tag{1.8}$$

$$P_2 \approx 3.94 \times 10^{14} \frac{W^{0.87}}{R_{el}^3 h^{1/3}} \quad \text{pascals.} \tag{1.9}$$

Other models for explosions have been based on fitting polynomials to near-field reduced displacement potentials (Haskell, 1967, von Seggern and Blandford 1972, Helmberger and Hadley 1981). The revision of Haskell's (1967) model proposed by von Seggern and Blandford (1972) gives spectra that are nearly identical to the

Mueller-Murphy (1971) model.

The generation of seismic waves by earthquakes has been the subject of many kinematic and dynamic modeling efforts. One the most widely used models of the seismic source spectra is characterized by a single corner frequency and a high frequency decay proportional to ω^{-2} (Aki, 1967, Brune 1970). In this paper we examine a specific ω^{-2} model, proposed by Brune (1970), in which the earthquake is modeled as a circular shear crack that slips instantaneously. Here we assume that the P/S corner frequency ratio is equal to the P/S wave velocity ratio as some studies show (e.g. Molnar, 1973). The far-field displacement amplitude spectrum for this model is given by (Brune, 1970, 1971):

$$\Omega^P(\omega) = R_{\Theta\Phi} \frac{r\sigma\alpha}{3R\mu} \frac{1}{\omega^2 + \omega_c^2}$$

(1.10)

In (1.10) σ is the stress drop, r is the radius of the shear crack, $R_{\Theta\Phi}$ is the radiation pattern factor, and ω_c is the angular corner frequency which is given by $\omega_c = 2.34\,\alpha/r$. We will refer to this model as W2P (ω^{-2} decay for P waves).

Archambeau (1968, 1972) developed a model for earthquakes in which the seismic waves are generated by the relaxation of pre-existing stress over a spheroidal volume. The high frequency decay for the far-field P wave displacement spectrum of this model (with rupture velocity equal or less than the shear wave velocity) is proportional to ω^{-3}. We will refer to this model as W3P. We follow Evernden et al. (1986), in using only the asymptotic values for the far-field spectra of the W3P model. At low frequencies the spectra has a constant low frequency value given by:

$$\Omega_o^P = \frac{5\sigma L^3 R_{\Theta\Phi}}{23\mu\alpha R}$$

(1.11)

from zero frequency up to a corner frequency:

$$f_c^P = \frac{1}{2\pi L}(3\alpha^2 v_r)^{1/3}$$

(1.12)

after which the spectrum decays as ω^{-3}. In equations (1.11) and (1.12) L is the maximum rupture dimension and v_r is the rupture velocity. In deriving equation (1.11) we have assumed a Poisson ratio of 1/4 and set the W3P moment equal to the expression for the zero frequency level of a double-couple point source (Walter et al., 1988).

Making use of equations (1.2 - 1.12) we can compare the high frequency behavior of these models. Figure 1a shows the theoretical far-field amplitude spectra of the Sharpe and Mueller-Murphy (M-M) models calculated for explosions with a yield of 100 kt and 1 kt. For comparison the two earthquake models have also been calculated for the same low frequency values as the Sharpe model. For the W3P model we
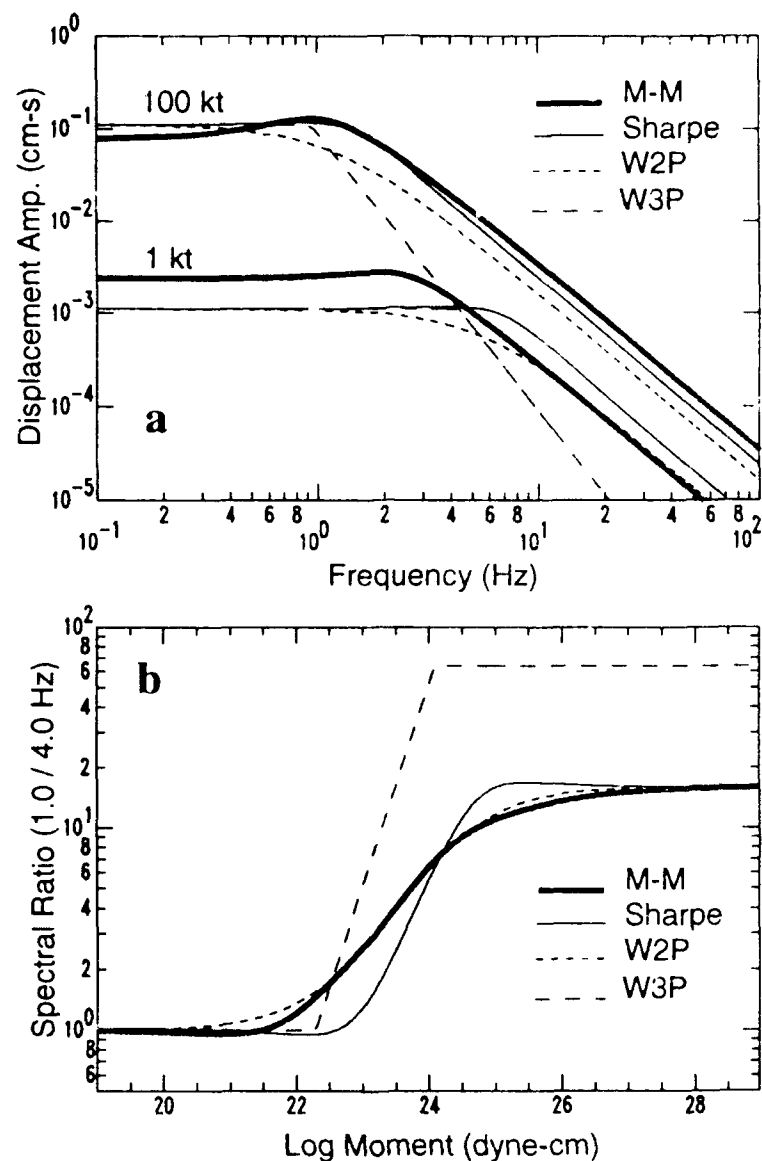
Fig. 1. A comparison of the Mueller-Murphy (M-M) and Sharpe explosion models
with the W2P and W3P earthquake models. (a) Displacement amplitude spectra
calculated for two different low frequency values. The uppermost explosion curves
were calculated for an explosion yield of 100 kt. The lower explosion curves were
calculated for a yield of 1 kt. The earthquake models have the same low frequency
levels as the Sharpe curves. (b) 1.0/4.0 Hz spectral ratio versus moment for the
models. In both figures the explosion models were calculated using equations (1.1)
and (1.5-1.9) with a P wave velocity of 4.6 km/s. For the Sharpe model Po = 200 bars
and k=9 and for the M-M model equations (1.6-1.9) were used. The earthquake
models were calculated using equations (1.10-1.12) with a P wave velocity of 6 km/s
and a stress drop of 100 bars. For (b) a single relation appropriate for the earthquake
source parameters was used to calculate the moment from the low frequency level.

9

have assumed that the rupture velocity is equal to the shear wave velocity. This gives the maximum high frequency values for the W3P model since at higher rupture velocities the spectrum decays as ω^{-2}, and at lower velocities both the corner frequency and spectral amplitudes above the corner frequency decrease (Evernden et al., 1986, Figure 16). (When the W3P model has rupture velocities slower than the shear wave velocity the asymptotic form of the spectral shape is no longer as good an approximation since the transition between the flat spectrum at low frequencies and the ω^{-3} falloff at high frequencies occurs over a wider frequency band). Figure 1a shows the large difference in high frequency (> 10 Hz) energy content between the W3P and explosion models. Differences between the W2P model and the explosion models are smaller and primarily due to slightly higher corner frequencies of the explosion models.

One of the more promising regional discriminants based on studies of Western U.S earthquakes and explosions are spectral ratios of regional phases (Murphy and Bennett, 1982; Bennett and Murphy, 1986, Taylor et al. 1988). The differences in the high frequency falloff between the four models discussed above predict very different source P wave spectral ratios. Figure 1b shows the log of the spectral ratio of 1.0 Hz to 4.0 Hz energy as a function of moment, using the same parameters as Figure 1a. For small moments the ratios are unity since both frequencies are on the constant part of the spectrum. For large moments the ratio is a constant value greater than unity, since both frequencies are on the decaying part of the source spectra. For these higher moments the W3P 1.0 to 4.0 Hz ratio is larger than for the other models due to the ω^{-3} decay rate, and suggest the source spectral ratio would be a reliable discriminant between earthquakes and explosions, assuming the W3P and either explosion model is valid. For moments from about 10^{22} to 10^{26} dyne-cm, the frequencies fall on either side of the source corner frequency, and the behavior of the spectral ratio curves in Figure 1b reflect the different corner frequency scaling of each model. If the W2P model for earthquakes is valid, the corner frequency scaling of both the W2P and either explosion model will play a large role in the success of a spectral ratio discriminant based purely on differences in source spectra.

From equations (1.10 - 1.12) we can find a relation for both the W2P and W3P models between low frequency level, stress drop and corner frequency if we hold the medium dependent parameters and observing distance constant:

$$\Omega^P(\omega \to 0) \propto \frac{\sigma}{(f_c^P)^3} \qquad (1.13)$$

Given two earthquakes with the same moment (i.e. same low frequency level) but different stress drops, the one with the high stress drop has both a higher corner frequency and more high frequency energy than the event with the lower stress drop. A similar relationship can be found for explosions from equations (1.2) and (1.5) with the pressure replacing the stress drop:

$$\Omega^P(\omega \to 0) \propto \frac{P_i}{(f_c^P)^3} \qquad (1.14)$$

10

where i = 0 for the Sharpe model and i = 2 for the Mueller-Murphy model. For explosions the corner frequency is inversely proportional to the elastic radius [Murphy, 1977]:

$$f_c^P = \frac{\alpha}{2\pi R_{el}} \cdot \qquad (1.15)$$

Equations (1.13) and (1.14) show that (for earthquakes and explosions with the same low frequency spectral level) the ratio of explosion corner frequency to earthquake corner frequency depends on the ratio of explosion pressure to earthquake stress drop. For example the Sharpe model with $P_o = 200$ bars will have about the same corner frequency as W2P model high stress drop earthquakes (100 - 200 bars). In this case a spectral ratio discriminant will not work very well (see Figure 1b). For extremely high stress drop events (> 800 bars), the corner frequencies of the W3P and Sharpe model would be about equal, but the difference in falloff slope should still allow a spectral ratio discriminant to work if one of the frequencies chosen is sufficiently higher than the corner frequency. The Mueller-Murphy pressure P_2 given in equation (1.9) depends on both yield and depth complicating any simple comparisons. Nevertheless, it is apparent from Figure 1 that in the range from 1 to 100 kt (for the parameters assumed in Figure 1), high stress drop (100 - 200 bars) W2P earthquakes will not discriminate very well from these Mueller-Murphy explosions on the basis of source spectral ratios.

North American Data

In a previous paper (Walter et al., 1988, included as Appendix A) we tested some of the specific predictions of the W2P, W3P, and Sharpe models with high sample rate digital data recorded at small hypocentral distances (2 - 40 km). The earthquake data consist of events from the San Jacinto strike-slip fault region near Anza, California, the subduction zone near Oaxaca, Mexico and the Long Valley caldera and surrounding area near Mammoth Lakes, California. The explosions are NTS explosions from Pahute Mesa. To minimize the effects of attenuation we compared the variation of the earthquake high frequency amplitude with moment for each region using a constant set of stations and events with similar depths and ray paths. The determination of moment based on low frequency spectral amplitudes is relatively insensitive to attenuation and thus any increase in earthquake high frequency spectral amplitude with moment, within each region, can be attributed to a source effect. When comparing the absolute spectral amplitude of explosions with earthquakes, however, we need to take into account attenuation, site, and path effects.

Figure 2a displays 10 Hz P wave spectral amplitude as a function of moment for a variety of earthquakes and NTS Pahute Mesa underground nuclear explosions. Theoretical curves have been drawn for the Sharpe explosion model and for the W2P and W3P earthquake models. The sigmas denote the stress drop in bars for each earthquake curve. In Figure 2a the earthquake 10 Hz amplitudes are consistent with
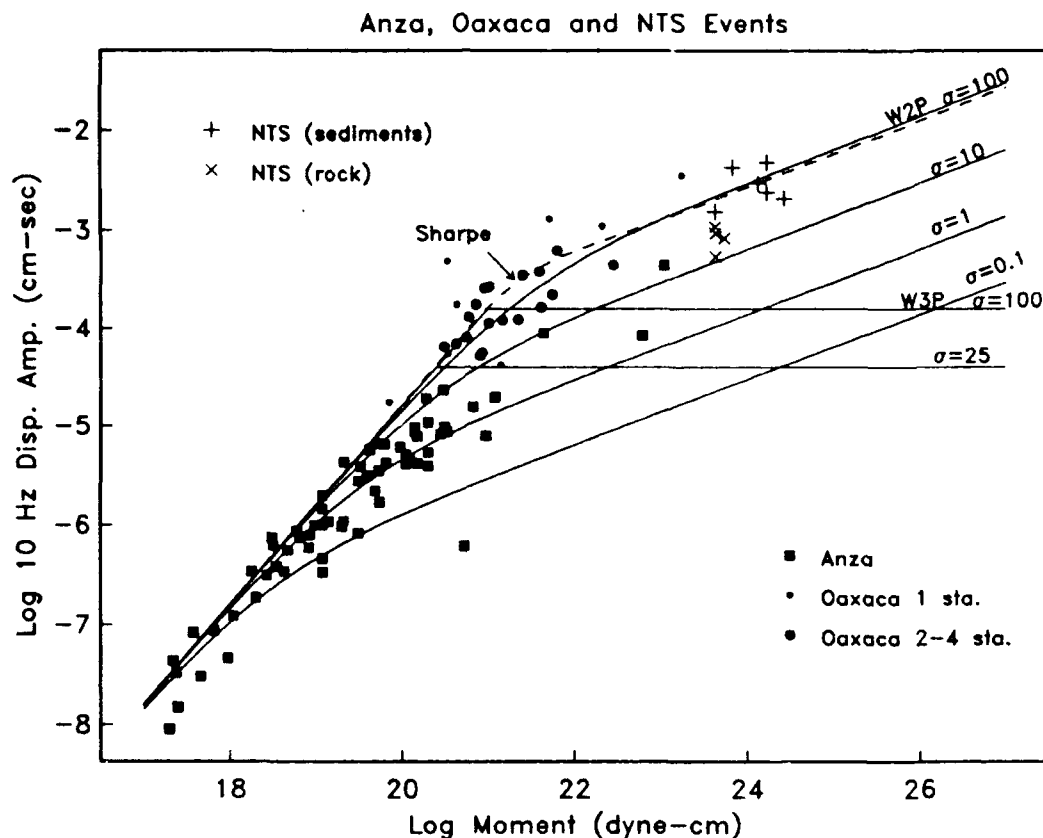
11

Figure 2a. P wave displacement spectral observations of earthquakes (solid symbols) and NTS explosions plotted as a function of moment, and compared with theoretical curves. All symbols and curves are normalized to a hypocentral distance of 10 km. No attenuation correction was applied to the data. Events where more than one station recording was used have reletively larger symbol size. Theoretical curves are for constant stress drop denoted by σ in bars. The W3P model is given for constant rupture velocity equal to the shear wave velocity. The Sharpe curve was calculated assuming Po = 130 bars and k=9.4, values appropriate for NTS. (a) The 10 Hz P wave displacement spectral amplitude as a function of moment. (from Walter et al., 1988)

both earthquake models and the explosions show about an order of magnitude scatter near the theoretical Sharpe amplitude prediction. Figure 2b compares 30 Hz P wave amplitudes versus moment with the same theoretical curves. The earthquakes show a continued increase in 30 Hz amplitude with moment consistent with an ω^{-2} falloff model and in disagreement with an ω^{-3} model for larger moments.

The explosion spectral amplitudes are from both hardrock and borehole sites (hypocentral distances 15 - 25 km) and sediment sites (2 - 12 km). One explosion was recorded on both hardrock and sediment sites; the 10 and 30 Hz spectral amplitudes at the hardrock sites were approximately a factor of two less than at the closer sediment sites. On the basis of limited velocity and attenuation data, Walter et al. (1988) estimated that the sediment recordings should approximate the source spectral amplitude at 10 Hz and underestimate it by about a factor of 3 at 30 Hz. The earthquake amplitudes are all from seismic stations located at hardrock sites (hypocentral distances 5 - 40 km). Based on estimates of the attenuation at Anza by Hough et al. (1988), we expect the 10 and 30 Hz spectral amplitudes to underestimate the source spectral amplitudes by about a factor of 2 to 3. Site effect studies at Anza show an increase in 10 and 30 Hz spectral amplitude by a factor of about 5 above the free surface effect. Therefore we expect the Anza spectral amplitudes shown in Figures 2a and 2b to slightly overestimate the source spectral amplitudes.

The explosions in Figure 2b separate into two groups: one showing two orders of magnitude less 30 Hz P wave energy than predicted by the Sharpe model, the other closer to the Sharpe prediction. The group with less 30 Hz energy was detonated at depths between 600 and 700 m while the group with more 30 Hz energy was detonated at depths of 800 to 1100 m. Thus the shallower group has a high frequency spectral decay between 10 and 30 Hz that is much greater than the ω^{-2} predicted by the Sharpe model. The shallower explosions were detonated near the level of the water table (about 650 m) at Pahute Mesa and we suggested that the location of the explosion relative to the water table may cause the difference in falloff slope between the deep and shallow events (Walter et al., 1988). These results are similar to the change in high frequency slope observed by Denny (1990) and used by Taylor and Denny (1990) to model spectral differences observed between NTS and KTS explosions. Taylor and Denny (1990) show that for weak porous rock the radiated shock wave divides into a two wave system. In terms of the Sharpe model this is equivalent to introducing a rise time in the pressure function at the elastic radius, so the far-field P spectra then decays as ω^{-3} at high frequencies.

Figures 2a and 2b imply that Anza earthquakes have more 30 Hz P wave energy than NTS Pahute Mesa explosions detonated near the water table, in contrast to the Evernden et al. (1986) proposal. Chael (1988) has noted that the slope of the P_g spectra discriminate between NTS explosions and western U.S. earthquakes in the opposite sense of the Evernden et al. (1986) proposal since the explosions had steeper high frequency spectral slopes than the earthquakes. Murphy and Bennett (1982) and Taylor et al., (1988) used low to high frequency spectral ratios for P_n, P_g, and L_g and noted that the NTS explosions had less high frequency energy than the western U. S. earthquakes. In contrast, Taylor and Marshall (1990) compared KTS events to shallow Asian earthquakes and found that the explosions had more high frequency P wave
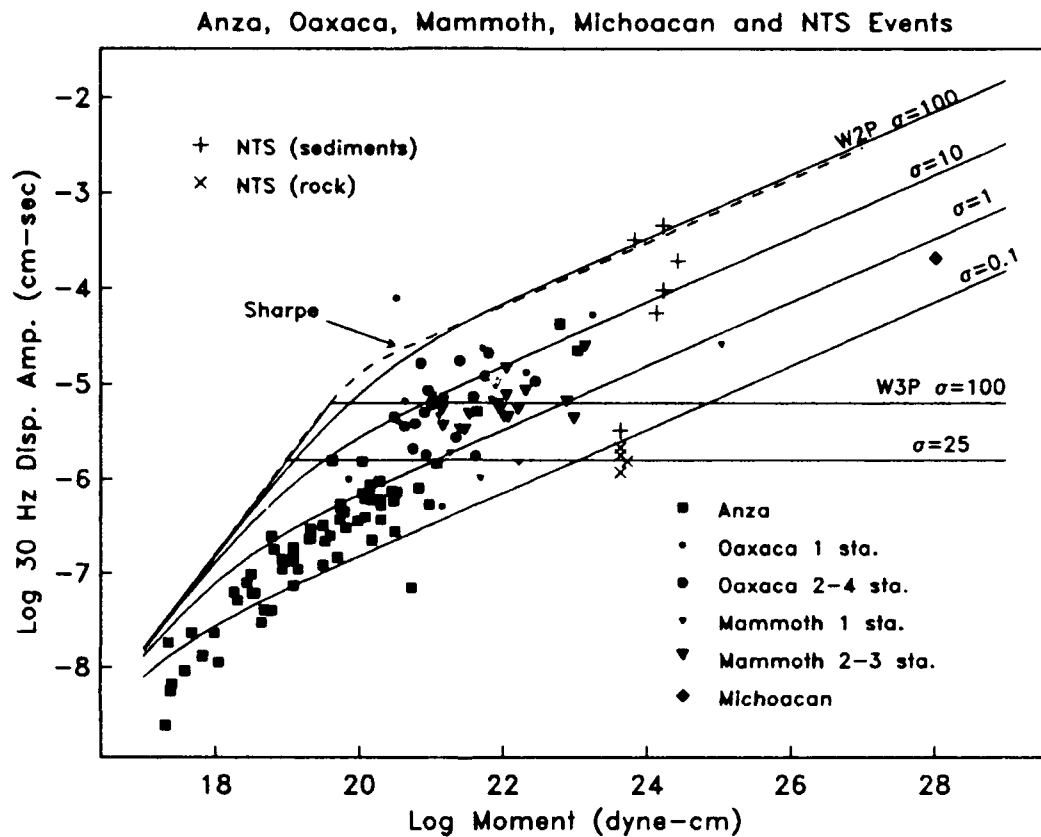
Fig. 2b. The 30 Hz P wave displacement spectral amplitude as a function of moment (from Walter et al., 1988)

14

energy than the earthquakes. The material properties and depth to the water table at KTS are very different from NTS. This raises the questions of what are the corner frequency scaling and high frequency decay slope for Soviet KTS explosions, and, whether Soviet explosions can be discriminated from earthquakes in either the manner of Evernden et al. (1986), or the manner of Chael (1988). We seek a preliminary answer to these questions by examining the regional seismic data recorded in the vicinity of the Soviet East Kazakh Test Site.

Central Asian Data

Soviet JVE. Figure 3 shows the location of the September 14, 1988 Soviet JVE explosion (NEIC m_b=6.1, about 650 m depth) and the four near regional seismograph stations which recorded the event and whose digital seismograms are available to us. The three closest stations, Karkaralinsk (KKL, $\Delta \approx 255$ km), Bayanaul (BAY, $\Delta \approx 255$ km) and Karasu (KSU, $\Delta \approx 160$ km) were installed as part of a cooperative data collection effort between the Natural Resources Defense Council (NRDC) in the U. S. and the Soviet Academy of Sciences (SAS) in the U. S. S. R. (Priestley et al., 1990). Both short period (1 s) and broadband (15 s free period) high sample rate (200 sample/s) seismographs recorded the Soviet JVE at the NRDC-SAS sites. The seismometers were located in the same vaults as the previous NRDC-SAS cooperative experiment from 1986 - 1987 (Berger et al., 1987). All three of these stations are located on similar granitic intrusions of Paleozoic to early Mesozoic age (Leith, 1987). The seismograph located at Talgar (TLG, $\Delta \approx 740$ km) is a digital seismograph operated by the SAS and has a free period of 1.6 seconds (Priestley et al., 1990) and a flat velocity response to about 15 Hz. TLG is situated on the Northern flanks of the Zaili-Alatau mountains and is sited within Precambrian and lower Paleozoic crystalline rocks.

Seismograms of the Soviet JVE from the vertical short period components at the three NRDC-SAS sites are shown in Figure 4. The KKL seismogram shows an emergent low frequency first arrival followed about three-quarters of a second later by a low amplitude higher frequency arrival. The BAY seismogram shows a single arrival containing high frequencies. The stations KKL and BAY are past the P_n - P_g crossover distance predicted from the Eastern Kazakhstan velocity structure (Antonova et al., 1978; Leith 1987; Priestley et al., 1988), and we assume the first low amplitude arrival is P_n. The relatively low frequency content of the first KKL P_n arrival is consistent with this arrival being a head wave; however, the relatively high frequency content of the second low amplitude KKL arrival and the BAY P_n arrival are more consistent with their being turning rays. The P_g wavetrain is dominated by the large amplitude dilatational arrival on the vertical and radial components following the P_n arrival by about 1.5 seconds. The dilatational motion of this arrival suggests a supercritical reflection from the Moho. Synthetic reflectivity seismograms computed for the DSS velocity structure (Leith, 1987) agree in both the P_n - P_mP time interval and with the large amplitude and relatively simple shape of P_mP observed at BAY and, particularly, at KKL (Walter and Patton, 1990, Figure 1). The closest recording of the Soviet JVE was made at KSU within the P_n-P_g crossover distance. Both the short and long period records show a 3 Hz resonance associated with the site (Berger et al., 1988;

75° E   80° E

▲ BAY

50° N

★★   ▲ KSU

▲ KKL

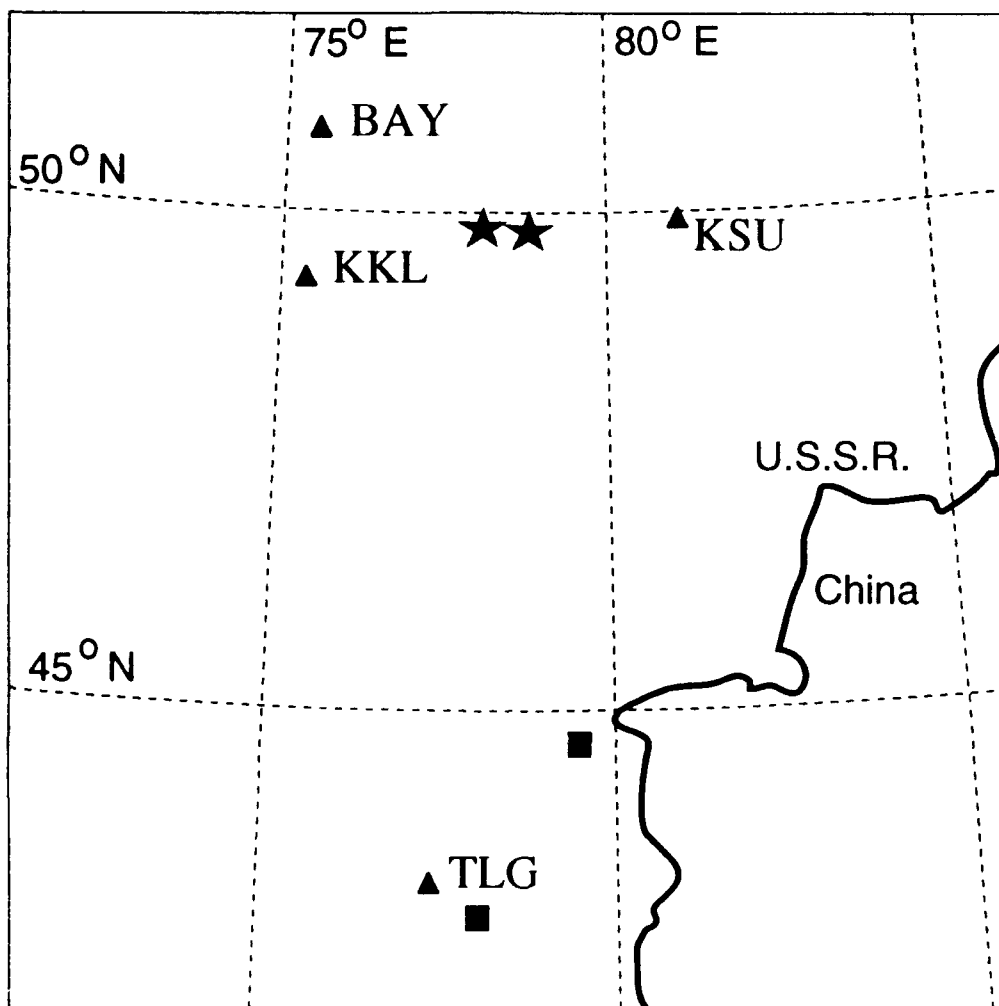U.S.S.R.

China

45° N

■

▲ TLG
■

Fig 3. Map showing locations of Soviet events and stations used in this study.
The explosions are denoted by stars and the earthquakes are denoted by squares.
The September 14, 1988 Soviet JVE explosion is the easternmost star. The
seismic recording stations are shown as triangles with their three letter
abreviations.

16

Priestley et al., 1990). The filtered KSU trace in Figure 4 shows a large amplitude arrival following the first arrival by about two seconds, which is consistent with the time for the P_mP arrival at this distance range.

P wave spectra of the Soviet JVE, both corrected and uncorrected for attenuation, from data recorded at BAY and KKL are shown in Figure 5. The spectra from KSU are contaminated by the site resonance and are not shown. In order to estimate the effect of any site resonance at KKL we computed the ratio of the surface to borehole (66 m deep) spectral amplitude from the first six seconds of the P wave from the m_b = 4.6 earthquake of May 26, 1987. The surface to borehole spectral ratio, shown in Figure 6 displays little evidence of any near surface site effect between 1 and 10 Hz, but there is an amplification of the surface spectra of about 2 to 4 in the 10 - 30 Hz range. Thus we expect site effects at KKL to have little or no effect on the shape of the spectra less then 10 Hz and a small effect on decay rates above 10 Hz. The first arrival of this earthquake was not recorded at BAY but a comparison of the surface and borehole (99 m deep) P coda in the 7.2 to 6.0 km/s group velocity window shows no evidence of surface resonance in the 1 to 6 Hz frequency band where the surface recording has a reasonable signal-to-noise ratio. Thus we do not expect the BAY spectral shape to be strongly effected by site effects between 1 and 6 Hz. The borehole instruments at the NRDC-SAS sites had been removed by the time of the Soviet JVE.

Spectra for an equal length data window prior to the P_n or P_g arrival were computed to indicate the noise level and are also shown in Figure 5. The spectra uncorrected for attenuation, should give a minimum estimate for the source corner frequency and a maximum estimate for the source spectral decay slope. The uncorrected P_n and P_g spectra at BAY give similar corner frequencies of 2.6 - 4.0 Hz and decay as ω^{-3} at higher frequencies. The uncorrected P_n spectra at KKL does not show a clear corner frequency, perhaps because of the complicated multiple arrival as discussed above. The uncorrected P_g spectrum at KKL has an apparent corner frequency of about 1.5 Hz and decays as $\omega^{-1.6}$ from 2 to about 7 Hz steepening to $\omega^{-3.8}$ from 7 to 25 Hz. The corner frequency determined by the intersection of the $\omega^{-3.8}$ asymptote with the low frequency level is about 3 Hz. To correct the P_n spectra for attenuation we used the results of Sereno [1990] who determined P_n attenuation to be given by $Q(f) = 300 f^{0.5}$ by assuming a source spectrum similar to the W2P model for both earthquakes and mine blasts, and fitting spectra from data recorded at the three NRDC-SAS sites. Sereno (1990) notes a frequency independent value of Q = 1175 fit the data equally well. To correct the P_g spectra for attenuation we have used the P_g Q of 2000, estimated by Given et al. (1990) to be a minimum value for frequencies above 10 Hz on the basis of chemical blasts recorded at the NRDC stations in Kazakhstan. Given et al. (1990) note that the differing ray paths strongly affect the P_g amplitude so that $Q \geq 2000$ should be regarded as a tenuous estimate. The attenuation corrected BAY P_n, P_g and KKL P_g spectra for the Soviet JVE have about the same corner frequencies as the uncorrected spectra. The high frequency decay slopes of the BAY P_n and P_g spectra decay approximately as $\omega^{-2.2}$ in the range of 5 - 25 Hz. The KKL P_g spectra decay as $\omega^{-1.4}$ in the range from 1.5 - 7 Hz and as $\omega^{-3.0}$ in the range from 7 - 25 Hz.
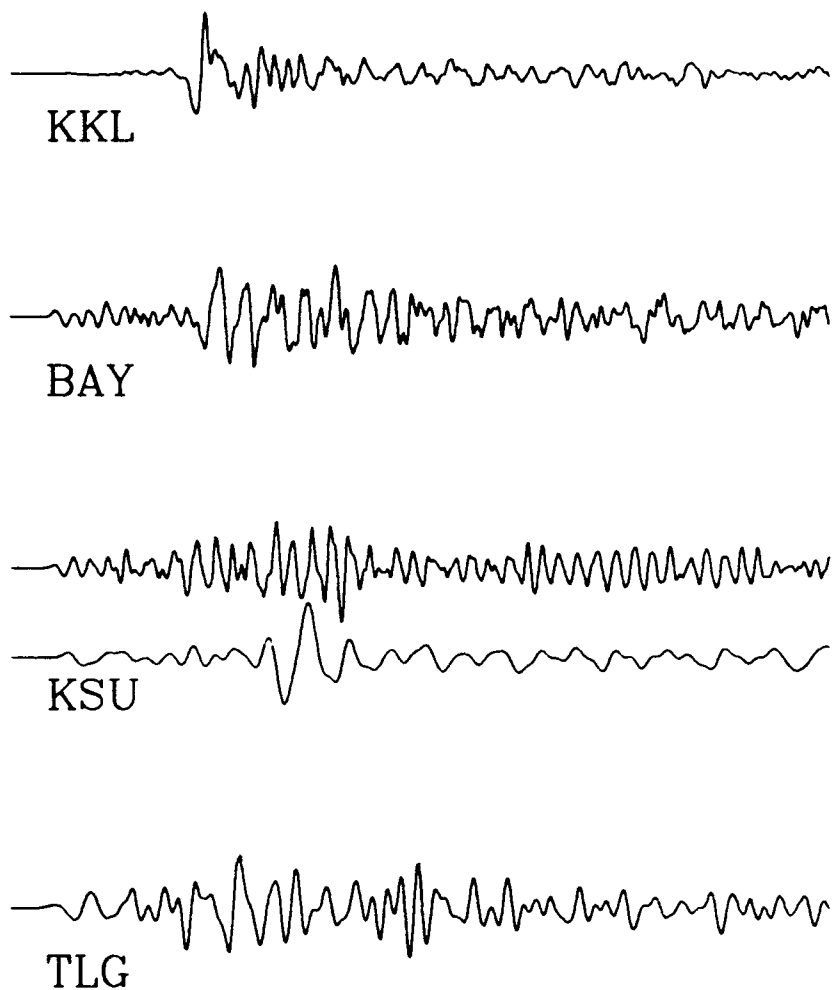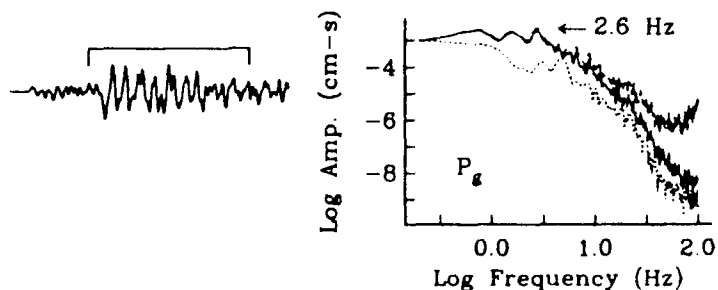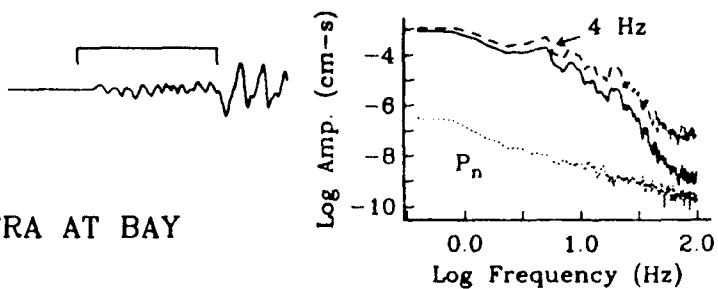
Fig. 4. Short period vertical seismograms of the Soviet JVE recorded at the four regional seismograph sites shown in figure 3. Two expanded plots of the KSU P wave are shown, the upper plot is the original data and the lower trace is the same data after low pass filtering with a four pole butterworth filter with a corner at 1.5 Hz in order to remove the 3 Hz site resonance.
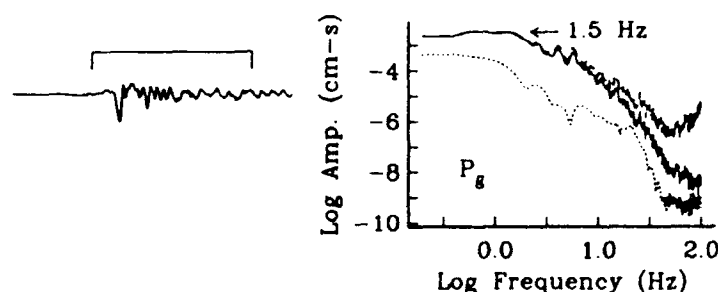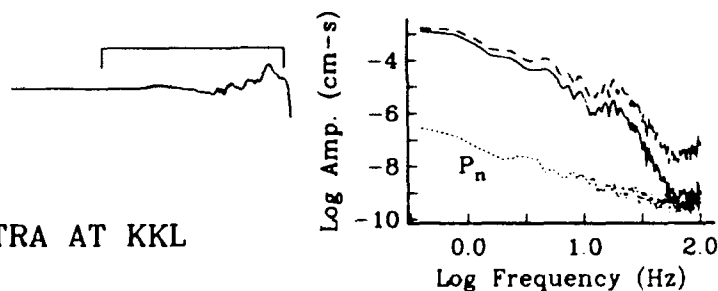
Fig. 5. Spectra of Soviet JVE recorded at stations BAY (top) and KKL (bottom). Windows used in computing spectra are also shown. Dotted lines indicate spectra of an equal length window preceding the signal to indicate the noise level. Solid lines are the uncorrected signal spectra and dashed lines have been corrected for attenuation as described in the text. Corner frequency is indicated for both the Pn and Pg phases at BAY and for the Pg phase at KKL.

19

Fig. 6. Ratio of surface-to-borehole P wave spectra of the first six seconds of the May 26, 1987 event (NEIC mb = 4.6, 740 km distant) recorded at KKL. The borehole seismometers were 66 m below the surface. The spectra were smoothed once with a five-point running mean prior to computing the ratio.

20

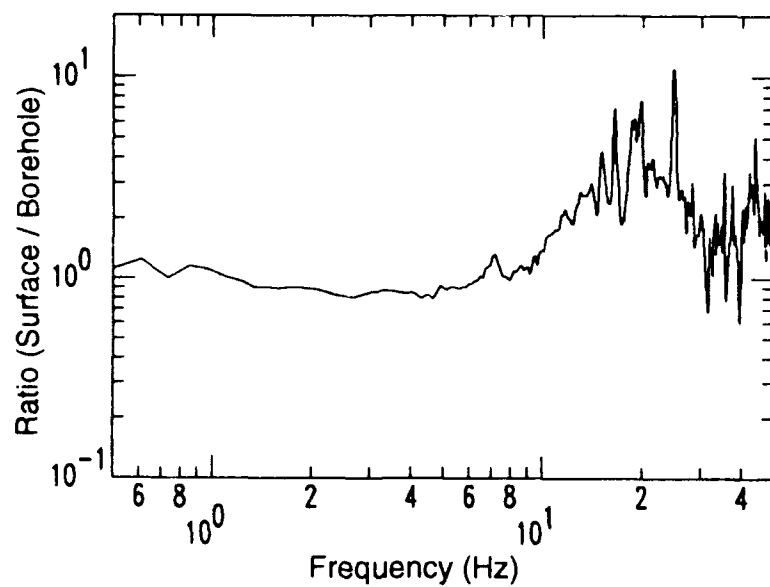One of the interesting features of the near regional recordings of the Soviet JVE is the large high frequency SH phases apparent on the transverse components. The SH pulse on the BAY transverse component has a frequency of about 1 Hz. These phases have been modeled as tectonic release by Walter and Patton (1990). It is often assumed that tectonic release has a negligible contribution at frequencies of 1 Hz or greater, but these seismograms raise questions about whether such assumptions are valid for KTS explosions.

Comparison of Soviet Earthquakes and Explosion. In order to isolate differences in source spectra from propagation effects, we attempt to minimize the effects of attenuation as much as possible by comparing the spectra of two Soviet explosions with the spectra of two earthquakes recorded over similar, but nearly reversed paths. The two earthquakes (whose location is shown in Figure 3) occurred on July 21, 1986 and May 26, 1987. Both events were $m_b = 4.6$ (NEIC), and were recorded at KKL. The 1986 event was about 610 km distant (NEIC depth 33 km) and the 1987 event was about 740 km distant (NEIC depth 20 km). The two explosions are denoted by solid stars in Figure 3. The easternmost explosion in Figure 3 is the Soviet JVE; the other explosion is an $m_b = 4.9$ (NEIC) event which occurred at Degelen on October 18, 1988. Both were recorded at the Soviet Academy of Sciences station Talgar (TLG) near Alma-Ata, about 740 km away.

Figure 7 compares instrument-corrected P_n spectra from each event. For these near reciprocal propagation paths the explosions have a relatively greater high frequency decay compared with the earthquakes. Fitting the log-log spectrum from 5 to 20 Hz with a least squares line we obtain fall off slopes of about $\omega^{-3.5}$ and $\omega^{-4.0}$ from the 1986 and 1987 earthquake, respectively. In contrast the JVE explosion has a larger decay, about $\omega^{-5.0}$ between 5 and 15 Hz. The smaller Degelen explosion shows a similar high frequency decay where the signal is above the noise. The explosions have high apparent corner frequencies, about 5 Hz. The earthquakes do not show a well defined apparent corner frequency but show gradually larger decay rates with increasing frequency.

Discussion

Since we have only a limited Soviet data set, any conclusions are of necessity, preliminary. The steeper high frequency P wave spectral decay observed for the Soviet explosions compared with those observed for Central Asian earthquakes (Figure 7) with nearly reciprocal paths, is similar to that observed for North American earthquakes and explosions (Chael, 1988; Walter et al., 1988). However, although comparing data along nearly reciprocal paths minimizes attenuation effects related to the propagation path, we have not eliminated effects due to the differences in source depth nor the differences in seismograph site effects. The attenuation corrected near regional JVE spectra show falloff slopes between ω^{-2} and ω^{-3}. If the attenuation correction is valid and Soviet earthquakes falloff as ω^{-2}, then the significant difference in slope observed in the near reciprocal path data between the earthquakes and explosions may be partly due to depth dependent attenuation effects, seismograph site effects at TLG,

21

JVE recorded at TLG
(mb=6.1, depth~600 m, Δ~740 km)

Degelen Explosion
recorded at TLG
(mb=4.9, depth~300m, Δ~740km)

Earthquake recorded at KKL
(mb=4.6, depth~33 km, Δ~740km)

Earthquake recorded at KKL
(mb=4.6, depth~20 km, Δ~610km)

Log Frequency (Hz)

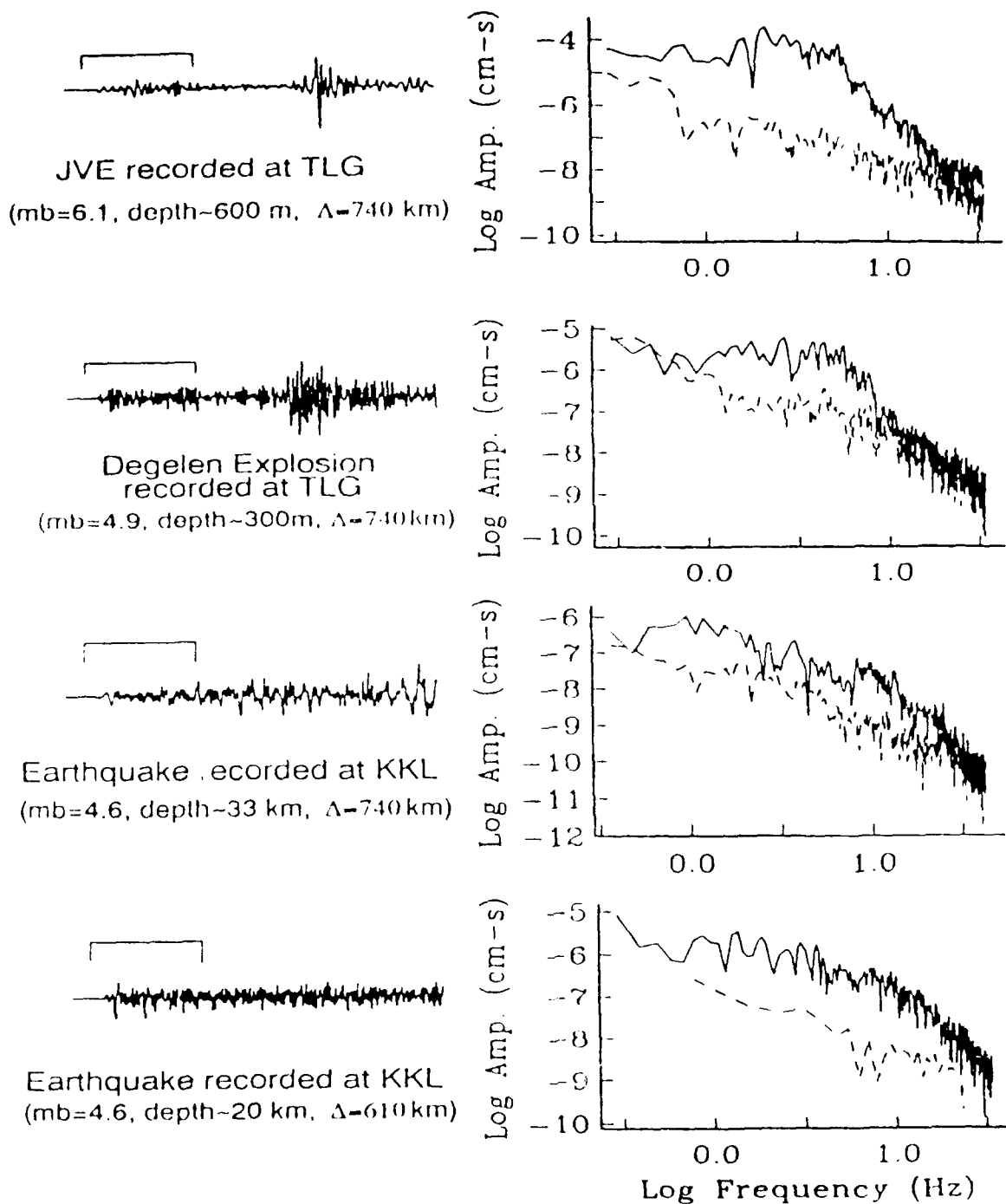Fig. 7. Pn spectra of Soviet explosions and earthquakes recorded on nearly reciprocal paths. The top two traces are the September14, 1988 Soviet JVE explosion and the October 18, 1988 Degelen explosion recorded at TLG. The bottom two traces are the May 26, 1987 and July 21, 1986 earthquakes recorded at KKL. Earthquakes depths are from NEIC, explosion depths are estimates assuming NTS depth scaling.

or some a combination of both.

Recordings of the Soviet JVE show more high frequency energy in the 2 to 5 Hz band than predicted by the Sharpe or Mueller-Murphy models. Priestley et al, (1990) used the L_g amplitude at the near regional NRDC-SAS stations to estimate a yield of about 120 kt for this event. Sykes and Ekstrom (1989) used a combined m_b - M_s magnitude yield relation to obtain a similar value 113 Kt. The corner frequency for the Soviet JVE (assuming a 120 kt yield) predicted by the Sharpe model from equation (1.3) and (1.15) is about 1.4 Hz. The apparent corner frequency predicted by the Mueller-Murphy model from equations (1.9) and (1.15) for a depth of 650 m is about 0.95 Hz. Because of the peaking near the corner frequency in the Mueller-Murphy model, the intersection of the high and low frequency asymptotes gives a slightly higher value for the corner frequency, about 1.7 Hz. The average corner frequency of the Soviet JVE (using the asymptotic corner frequency for the KKL P_g spectrum, and the BAY P_n and P_g spectra) is about 3 Hz. If we assume that this corner is not due to spall, site effects or tectonic release, then both the Sharpe model and the Mueller-Murphy model would appear to under predict the corner frequency from Soviet explosions. However, the large SH phases on the transverse components suggest that complications to the explosion source, such as spall and tectonic release, may be adding significant high frequency energy to this event. Walter and Patton (1990) used surface wave amplitudes from the NRDC-SAS stations to estimate the tectonic release moment at about one fifth to one tenth that of the explosion. If the tectonic release source spectra resemble the typical earthquake spectra (i.e. flat out to a corner and then decaying) it would be difficult to explain the high P wave corner frequencies on this basis. Recent theoretical calculations for spall in a velocity model appropriate for KTS (Barker et al, 1990, McLaughlin et al., 1990) give a peaked spectrum at about 1 - 4 Hz for the JVE. Synthetic calculations for P_n and P_g by McLaughlin et al., (1990), indicate the spectral amplitude at 1 - 4 Hz may be dominated by spall. Without near source acceleration data however, it is difficult to determine whether spall is a significant contributor of 1 - 4 Hz energy for the Soviet JVE. The smaller explosion shown in Figure 7 presumably contains tectonic release and spall signals that are different from the JVE event, yet they have similar apparent corner frequencies at the TLG station.

The relatively high frequency content of the near regional Soviet JVE spectra can also be seen by comparing 1 to 4 Hz spectral ratios with theoretical calculations. We calculated the ratio of the 0.75 - 1.25 Hz to 3.0 - 5.0 Hz energy for the attenuation corrected spectra in Figure 5. The BAY P_n, P_g and KKL P_g regional phases give spectral ratios of 2.2, 2.8, and 5.7 respectively The Mueller-Murphy and Sharpe models predict larger spectral ratios of 6.6 and 8.3 respectively. For comparison the W2P earthquake model gives a spectral ratio of 7.2 (100 bar stress drop) or 12.3 (10 bar stress drop), and the W3P earthquake model gives a spectral ratio of about 64 (for either 100 or 10 bar stress drop), when constrained to have about the same low frequency level as the Soviet JVE. Thus the Soviet JVE also shows both smaller explosion spectral ratios than predicted by theory, and than expected for earthquakes.

23

We also calculated the same spectral ratios of the spectra of the m_b = 6.1 Soviet JVE recorded at TLG and the m_b = 4.6 earthquake that occurred near the TLG station recorded at KKL using the previously assumed P_n attenuation correction (Sereno, 1990). Again the explosion has a small spectral ratio of about 0.25, which is much less than the ratio of about 4.2 calculated for the earthquake, even though the earthquake is about 1.5 m_b units smaller. The earthquake spectral ratio value of 4.2 is consistent with a 10 bar stress drop W2P model, but the explosion value is again much lower than either explosion model predicts. Because the paths are nearly reciprocal the ratio of the two different spectral ratios does not depend upon the specific distance attenuation correction chosen, but it may be influenced by depth dependent attenuation or site effects at TLG as noted above. This may be reflected in the less than one explosion spectral ratio value, indicating that there is some peaking of the TLG spectra near 4 Hz. Such peaked spectra are not observed at the closest stations. Overall these observations give similar results to Taylor and Marshall (1990) who found that KTS explosions gave lower 0.5 - 1.0 Hz to 2.0 - 3.0 Hz spectral ratios when compared with shallow Central Asian earthquakes at the United Kingdom teleseismic arrays.

Conclusions

The North American earthquake data presented in this paper are consistent with a constant stress drop W2P model, and have more high frequency energy than shallow NTS explosions at Pahute Mesa which show a spectral decay greater than ω^{-3} above 10 Hz. In contrast the attenuation corrected near regional recordings of the Soviet JVE *explosion* have a spectral decay between ω^{-2} and ω^{-3} from 10 to 25 Hz. These results are approximately consistent with the hypothesis of Taylor and Denny (1990), who found that spectral ratio data from U.S. explosions could be fit by an explosion model that decays as ω^{-3} at high frequencies, KTS (Shagan River) explosion spectral ratios could be fit with a model that decays as ω^{-2}, and both western U.S. and Central Asian earthquake spectral ratios were consistent with an W2P model. In addition, we found the near regional recordings of the Soviet JVE have a higher corner frequency than predicted by both the Mueller-Murphy model for granite and the Sharpe (using Evernden et al. parameters for KTS) model. This higher corner frequency does not appear to be due to attenuation, path or site effects. The higher corner frequency causes a lower observed explosion 1 to 4 Hz spectral ratio for the Soviet JVE than is predicted by the explosion models. Comparing the Soviet JVE explosion with an earthquake recorded on nearly reciprocal paths we find a similarly low 1 to 4 Hz spectral ratio for the explosion and a higher ratio for the smaller m_b earthquake, which may be partly due to depth dependent attenuation, and site effects at TLG. Whether the higher corner frequency for the Soviet JVE is due to a need for a different explosion scaling relationship at KTS than contained in the models reviewed here, or is due to complications in the simple source models, such as spall and tectonic release, needs to be resolved in order to confidently use a discriminant based on differences between earthquake and explosion spectra.

References

Aki, K., Scaling law of seismic spectrum, *J. Geophys. Res.*, *72*, 1217-1231, 1967.

Anderson, J. G., Implications of attenuation for studies of the seismic source, in *Earthquake Source Mechanics*, S. Das, J. Boatwright, and C. H. Scholtz, Editors, American Geophysical Union Monograph, *37*, 311-318, 1986.

Antonova, L. V., F. F. Aptikayev, R. I. Kurochkina, I. L. Nersesov, A. V. Nikolayev, A. I. Ruzaykin, Y. N. Sedova, A. V. Sitnikov, F. S. Trergub, L. D. Fedorskaya, and V. I. Khalturin, *Experimental Seismic Investigation of the Earth's Interior*, AS USSR, Institute of Physics of the Earth, Publishing House "Nauka", Moscow, 155p, 1978.

Archambeau, C. B., General theory of elastodynamic source fields, *Rev. Geophys.*, *6*, 241-288, 1968.

Archambeau, C.B., The theory of stress wave radiation from explosions in prestressed media, *Geophys. J.*, *29* 329-366, 1972.

Barker, T. G., S. M. Day, K. L. McLaughlin, B. Shkoller, and J. L. Stevens, An analysis of the effects of spall on regional and teleseismic waveforms using two-dimensional numerical modeling of underground explosions, Air Force Geophysics Laboratory Report, GL-TR-90-0126,1990, ADA226921.

Bennett, T. J., and J. R. Murphy, Analysis of seismic discrimination capabilities using regional data from western United States events. *Bull. Seism. Soc. Am.*, *76*, 1069-1086, 1982.

Berger, J, H. K. Eissler, F. L. Vernon, I. L. Nersesov, M. B. Gokhberg, O. A. Stolyrov, and N. T. Tarasov, Studies of high-frequency seismic noise in Eastern Kazakhstan, *Bull. Seism. Soc. Am.*, *78*, 1744-1758, 1988.

Berger, J., J. N. Brune, P. A. Bodin, J. S. Gomberg, D. M. Carrel, K. F. Priestley, D. E. Chavez, W. R. Walter, C. B. Archambeau, T. B. Cochran, I. L. Nersesov, M. B. Gokhberg, O. A. Stolyrov, S. K. Daragen, N. D. Tarasov, Y. A. Sutelov, A new US-USSR seismological program, *EOS, 68*, 110-111, 1987.

Brune, J. N. Tectonic stress and the spectra of seismic shear waves from earthquakes, *J. Geophys. Res.*, *75*, 4997-5009, 1970

Brune, J. N., Correction, *J. Geophys. Res.*, *76*, 5002, 1971

Chael, E. P., Spectral Discrimination of NTS Explosions and Earthquakes in the Southwestern United States using High-Frequency Regional Data, *Geophys. Res. Lett.*, *15*, 625-628, 1988.

Dahlman, O., and H. Israelson, *Monitoring Underground Nuclear Explosions*, Elsevier Scientific Publishing Co., Amsterdam, 440 pp., 1977.

Denny, M. D., Free-field data and the seismic source function, this volume, 1990.

Der. Z., T. McElfresh, R. Wagner, and J. Burnetti, Spectral characteristics of *P* waves from nuclear explosions and yield estimation, *Bull. Seism. Soc. Am.*, *75*, 379-390, 1985.

Evernden, J.F., C.B. Archambeau, and E. Cranswick, An evaluation of seismic decoupling and underground nuclear test monitoring using high-frequency seismic data, *Rev. of Geophys.*, *24*, 143-215, 1986

Given, H., N. T. Tarasov, V. Zhuravlev, F. L. Vernon, J. Berger, and I. L. Nersesov, High-frequency seismic observations in Eastern Kazakhstan, USSR, with emphasis on chemical explosion experiments, *J. Geophys. Res. 95*, 295-307, 1990.

Haskell, N. A., Analytic approximation for the elastic radiation from a contained underground explosion, *J. Geophys. Res 72*, 2583-2595, 1967.

Helmberger, D. V., and D. M. Hadley, Seismic source functions and attenuation from local and teleseismic observations of the NTS events Jorum and Handley, *Bull Seism. Soc. Am., 71*, 51-67, 1981.

Hough, S. E., J. G. Anderson, J. Brune, F. Vernon, J. Berger, J. Fletcher, L. Harr, T. Hanks, and L. Baker, Attenuation near Anza, California, *Bull. Seism. Soc. Am., 78*, 672-691, 1988.

Leith, W., Geology of NRDC seismic stations in eastern Kazakhstan, USSR, *USGS Open-file Report 87-597*, 1987.

Malin, P. E., J. A. Waller, R. D. Borcherdt, E. Cranswick, E. G. Jensen, and J. van Schaack, Vertical seismic profiling of Oroville microearthquakes: velocity spectra and particle motion as a function of depth, *Bull. Seism. Soc. Am., 78*, 401-420, 1988.

McLaughlin, K., T. G. Barker, and S. M. Day, Implications of explosion generated spall models: regional seismic signals, Air Force Geophysics Laboratory Report, GL-TR-90-0133, 1990. ADA227273

Molnar, P., B. E. Tucker and J. N. Brune, Corner frequencies of P and S waves and models of earthquake sources, *Bull. Seism. Soc. Am., 63*, 2091-2104, 1973.

Mueller, R. A., and J. R. Murphy, Seismic characteristics of underground nuclear detonations: Part I. seismic spectrum scaling, *Bull. Seism. Soc. Am., 61*, 1675-1692, 1971.

Murphy, J. R., Seismic source functions and magnitude determinations for underground nuclear detonations, *Bull. Seism. Soc. Am., 67*, 135-158, 1977.

Murphy, J. R., and T. J. Bennett, A discrimination analysis of short period regional seismic data recorded at Tonto Forest Observatory, *Bull. Seism. Soc. Am., 72*, 1351-1366, 1986.

Pomeroy, P. W., W. J. Best, and T. V. McEvilly, Test ban treaty verification with regional data - a review, *Bull. Seism. Soc. Am. 72*, S89-S129, 1982.

Priestley, K. P., G. Zandt, and G. Randall, Crustal structure in eastern Kazakh, U.S.S.R. from teleseismic receiver functions, *Geophys. Res. Lett., 15*, 613-616, 1988.

Priestley, K. P., W. R. Walter, V. Martynov, and M. V. Rozhkov, Regional seismic recordings of the Soviet nuclear explosion of the Joint Verification Experiment, *Geophys. Res. Lett., 17* 179-182, 1990.

Rodean, H. C., *Nuclear Explosion Seismology*, U.S. Atomic energy commission, Division of Technical Information, 1971.

Sereno, T., S. Bratt, and T. Bache, Simultaneous inversion of regional wave spectra for attenuation and seismic moment in Scandinavia, *J. Geophys. Res., 93*, 2019-2035, 1988.

Sereno, T. J., Frequency-dependent attenuation in Eastern Kazakhstan and implications for seismic detection thresholds in the Soviet Union, *Bull. Seism. Soc. Am., in*

press, 1990.

Sharpe, J. A., The production of elastic waves by explosions pressures, 1. Theory and empirical field observations, *Geophysics, 7*, 144-154, 1942.

Stevens, J. L., and S. M. Day, The physical basis of m_b:M_s and variable frequency magnitude methods for earthquake/explosion discrimination, *J. Geophys. Res., 90*, 3009-3020, 1985.

Sykes, L., and G. Ekstrom, Comparison of seismic and hydrodynamic yield determinations for the Soviet joint verification experiment of 1988, *Proc. Natl. Acad. Sci. USA, 86*, 3456-3460, 1989.

Taylor, S. R., N. W. Sherman, and M. D. Denny, Spectral discrimination between NTS explosions and western United States earthquakes at regional distances, *Bull. Seism. Soc. Am., 78*, 1563-1579, 1988.

Taylor, S. R., M. D. Denny, E. S. Vergino, and R. E. Glaser, Regional discrimination between NTS explosions and western U.S. earthquakes, *Bull. Seism. Soc. Am., 79*, 1142-1176, 1989.

Taylor, S. R. and M. D. Denny, An analysis of spectral differences between NTS and Shagan River nuclear explosions, *Rep. UCRL-102276*, Lawrence Livermore Natl. Lab., Livermore, Calif., 1990.

Taylor, S. R., and P. D. Marshall, Spectral discrimination between Soviet explosions and earthquakes using U. K. array data, *Geophys. J., in press*, 1990.

von Seggern, D. and R. Blandford, Source time functions and spectra for underground nuclear explosions, *Geophys. J. R. Astr. Soc., 31*, 83-97, 1972.

Walter, W. R., J. N. Brune, K. Priestley, and J. Fletcher, Observations of high-frequency P wave earthquake and explosion spectra compared with ω^{-2}, ω^{-3}, and Sharpe source models, *J. Geophys. Res., 93*, 6318-6324, 1988.

Walter, W. R. and H. J. Patton, Tectonic release from the Soviet Joint Verification Experiment, *Geophys. Res. Lett. 17*, 1517-1520, 1990.

SECTION B

Tectonic Release from the Soviet Joint Verification Experiment

William R. Walter

Seismological Laboratory, Mackay School of Mines, University of Nevada, Reno

Howard J. Patton

Department of Earth Sciences, Lawrence Livermore National Laboratory

Abstract

The regional broadband seismic recordings of the Soviet Joint Verification Experiment underground nuclear explosion show evidence of tectonic release in the form of Love waves at long periods and high-frequency S_mS phases on the transverse components. We present the results of some simple forward modeling of this data in order to quantify both the moment and mechanism of the tectonic release. Using 10-20 second Love wave amplitude and phase data, we estimate the tectonic release moments to be 3.5×10^{15} N-m for a north striking right-lateral strike-slip fault, and 7.0×10^{15} N-m for a northwest striking reverse fault. Using the results of these end member tectonic models, the Rayleigh waves can be satisfied with explosion moments of 1.7×10^{16} N-m (F = 0.31) and 2.4×10^{16} N-m (F = 0.44), respectively. To resolve the ambiguity in tectonic mechanism we used the reflectivity method to generate synthetics and compare the relative amplitudes of the SH and SV parts of the S_mS phase. While the results favor the strike-slip mechanism of tectonic release, application of source inversion techniques to this data and other regional data will be needed to evaluate more realistic tectonic release models involving, for example, oblique fault slip and dip.

Introduction

On September 14, 1988, the Soviet Union conducted an underground nuclear explosion as part of the Joint Verification Experiment (JVE). Under an agreement between the Soviet Academy of Sciences and the Natural Resources Defense Council, the University of Nevada, Reno recorded the explosion at three seismic stations surrounding the Soviet test site at near regional distances (160-260 km). A description of the data, instruments and recording sites is given in Priestley et al. (1990).

Theoretically, spherically symmetric explosions should generate only P and SV waves. Observations of significant SH waves from explosions have been explained by two mechanisms: earthquake faulting triggered by the explosion (Brune and Pomeroy, 1963), and release of tectonic prestress in a shattered zone surrounding the explosion (Press and Archambeau, 1962). In either case an equivalent double couple mechanism can be found for this "tectonic release". Evidence of the tectonic release from the JVE at the near regional stations is supported by both the long period Love waves, and the short period phases arriving with a group velocity of about 3.5 km/s on the transverse components, particularly at BAY. We have identified the most prominent of these phases as S_mS, the Moho-reflected shear wave, as shown in Figure 9. Murphy and Archambeau (1986) observed a short-period coherent SH phase from the Rulison underground nuclear explosion on the transverse component of a very close station, 23 km away, but such short period evidence of tectonic release is not commonly observed.

Many investigators have noted anomalous surface waves from Soviet underground explosions in Eastern Kazakhstan (e.g. Rygg, 1979; Helle and Rygg, 1984; Given and Mellman, 1985). Tectonic release from a reverse fault striking northwest is the favored explanation, since some large F-value (Toksoz et al., 1971) events have reversed Rayleigh wave polarities at all stations. The 45° dipping reverse fault is the only mechanism that can account for these polarity anomalies at all azimuths.

In this study we try some simple forward modeling to determine the size and orientation of the tectonic release. We assume the mechanism is either pure strike-slip or pure reverse on a 45° dipping plane. First we use long period Love and Rayleigh amplitude and phase information to estimate the tectonic and explosive moments. There is an ambiguity however, since a reverse fault on a 45° dipping plane and a strike-slip rotated 45° with respect to the reverse, produce the same four-lobed Love wave radiation pattern. At low F-values Rayleigh waves cannot resolve the ambiguity due to the shallow source depth of explosions (Patton, 1988). To resolve the ambiguity we use the reflectivity method to generate synthetics and compare the relative amplitudes of the SV and SH parts of the S_mS phase.

Surface Wave Modeling

We used only two of the three stations, BAY and KKL (see Figure 3, in Chapter 1) in our analysis because of long period instrument problems at KSU. The azimuths of the two stations from the JVE differ by about 38 degrees. Each of these stations was about 260 km away from the JVE. The data were corrected for the effects of the instrument at long periods using the stopwatch measurements of the free periods (about 22 s at BAY, 15 s at KKL) and assuming 0.7 of critical damping. The corrected data were then rotated to vertical, radial and transverse components using the apparent back azimuth. We used arrival times from co-located University of Wisconsin instruments that had an omega receiver clock (H. Meyer, personal communication) and the origin time given by NEIC.
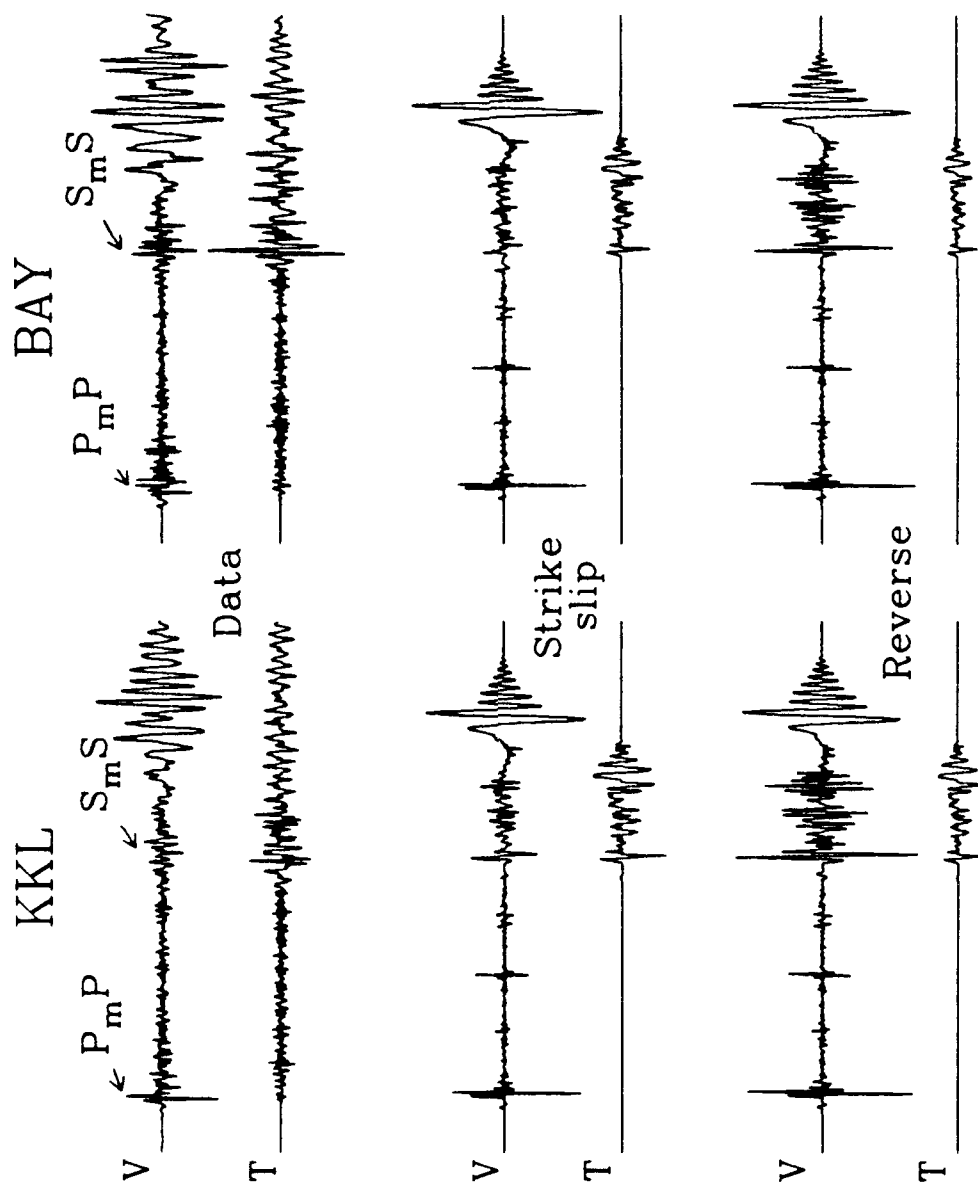
31

Fig. 8. Data and synthetics at 260 km. The first traces are the vertical
(V) and transverse (T) component recordings of the Soviet JVE at KKL
and BAY. The middle traces are the same components calculated
for an explosion plus a strike-slip model of tectonic release in the DSS
velocity model. The last traces were calculated for an explosion plus
a reverse fault model. Both data and synthetics have been low pass
filtered with a four pole Butterworth filter at 2.5 Hz.

32

Phase velocities and eigenfunctions were computed for the velocity model BAY-Japan (Priestley et al., 1988) using the method of Takeuchi and Saito (1972). The phase spectra of the Love and Rayleigh waves were found by taking the Fourier transform of a sixty second window starting at a group velocity of about 3.8 km/s. These phase spectra were then corrected for the travel path using the calculated phase velocities. The resulting source phase delay spectra are shown in Figure 10. The theoretical values for an explosive source of Rayleigh waves with step function time dependency is $3\pi/4$ radians (0.375 cycles). Note the reasonable match of the data to the theoretical for the Rayleigh waves, particularly at BAY. This gives us confidence in our velocity model and our subsequent interpretation of the Love wave source phase delay. The theoretical values for a double couple source with step time function dependency is $\pi/4$ or $5\pi/4$ radians (0.125 or 0.625 cycles) for Love waves, depending upon the polarity of the lobe of the radiation pattern. The Love wave data in Figure 10 show values of 0.675 cycles for both KKL and BAY implying they are on the same lobe of the radiation pattern. Using the additional information that the long period Love wave amplitudes are nearly equal constrains the orientation of a strike-slip mechanism to between about 355° and 15° in strike, or, for a reverse mechanism, to about 310° to 330°. In the following analysis we assume a strike-slip mechanism striking due north and a reverse mechanism striking due northwest.

The eigenfunctions were combined to compute synthetic spectra of the fundamental mode surface waves at the appropriate distances and azimuths of the two stations. Assuming the tectonic release is co-located and simultaneous with the explosion we adjusted the moment for an assumed mechanism until a reasonable fit was obtained in the period range of 5-20 seconds. Figure 11 shows the data and synthetics for Love waves at BAY assuming a north striking strike-slip mechanism and a seismic moment of 5.5×10^{15} N-m. A similar fit is obtained at KKL. Using an explosion moment of 1.7×10^{16} N-m with the strike-slip tectonic mechanism fits the Rayleigh wave data reasonably, as shown in Figure 11. As noted previously, we can generate the same synthetic Love wave spectra using a reverse mechanism and a moment twice as large as for the strike-slip case (7.0×10^{15} N-m). Assuming a reverse mechanism leads to an explosive moment of 2.4×10^{16} N-m. These results correspond to F = 0.31 for the strike-slip case and F = 0.44 for the reverse case.

Body Wave Modeling

To attempt to resolve the ambiguity between the two mechanisms of tectonic release, we looked at the SH and SV parts of the S_mS phase. Although the SH radiation patterns are the same for the two mechanisms, the SV patterns differ, causing different relative SV and SH S_mS amplitudes on the vertical and transverse components. We used the reflectivity method (Muller, 1985) and the same velocity structure as for the surface wave modeling along with the deep seismic sounding (DSS) model used as a starting model by Priestley et al. (1988). The DSS model has no low velocity zone and a stronger Moho contrast. The resulting differences in the synthetics between the two velocity models are shown in Figure 12. Both models give very similar long period (> 10 s) phase velocities, but differ at shorter periods. The
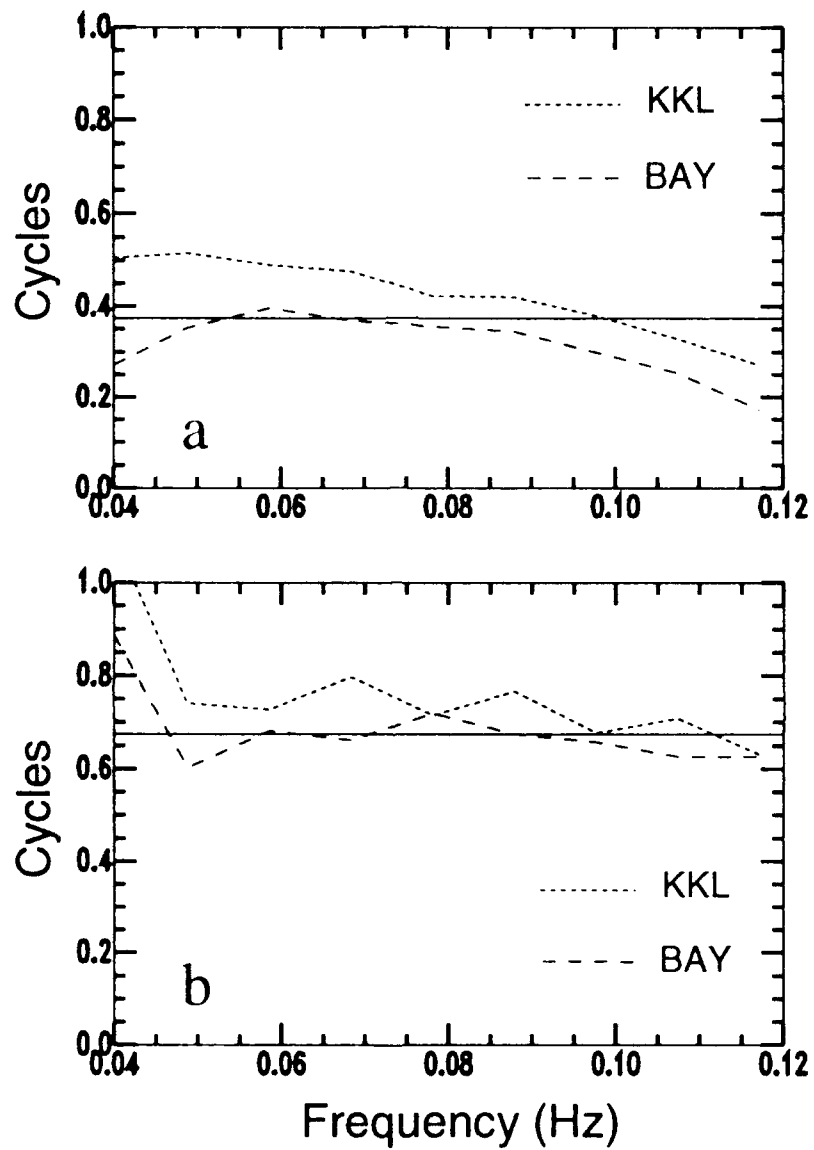
Fig. 9. Plot of (a) Rayleigh and (b) Love wave source phase delay at
stations BAY and KKL. The theoretical values are shown as solid lines.
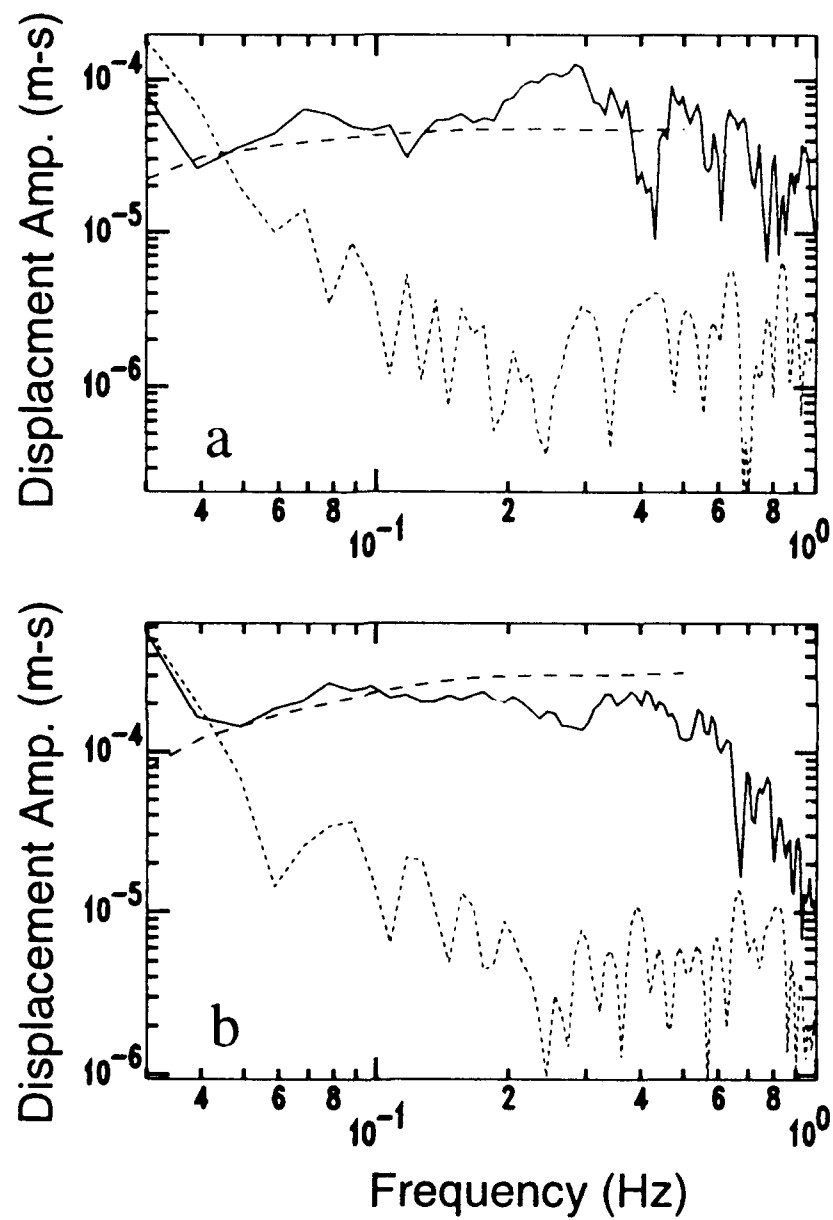The spectra have been normalized by a factor of 2 π

Fig. 10. Observed and synthetic (a) Love, and (b) Rayleigh wave spectra at BAY. The solid line is the amplitude spectra of 60 s of the surface waves, and the dotted line shows the preceding 60s for comparison. The dashed line is the synthetic spectra of the fundemental mode surface wave.

35

assumption of a constant high Q velocity structure resulted in large amplitudes of the higher mode surface waves which are not observed in the data. Observations of the dispersion of R_g phases in New England give crustal models with very low Q values in the uppermost kilometer (Saikia et al., 1990). The eastern region of the U.S. is often thought to be analogous to Eastern Kazakhstan. For these reasons we used an attenuation structure of $Q = 80$ in the top 1 km, $Q = 400$ from 1 to 2 km depth and $Q = 2000$ from 2 km down for P waves, and 3/4 of these values for S waves. In all cases we assumed a source depth of 640 m and a step source time function.

Figure 9 shows a comparison of the data and reflectivity synthetics at KKL and BAY. The KKL Pn and P_mP relative amplitude and character are matched quite well by the strike-slip synthetics. The reverse mechanism predicts a slightly larger P_mP than is observed. The S_mS phase for the reverse mechanism shows far too much amplitude on the vertical component relative to the transverse. The strike-slip mechanism comes closer to the correct amplitude ratio, but the data show an even higher frequency on the transverse than the synthetics. The strike-slip mechanism is also a better match of the relative vertical to transverse S_mS amplitude ratio at BAY. However the P_mP and S_mS character at BAY is not well matched, since the data show a less coherent P_mP arrival and a stronger SH S_mS arrival than the synthetics, possibly due to the limitations of the simple source assumptions.

Discussion

The orientation of the tectonic release is important in both the problems of determining the yield of an underground explosion using seismic data, and discriminating it from naturally occurring earthquakes. Both M_s and m_b measurements can be affected significantly due to tectonic release. For example the reverse mechanism usually assumed in Eastern Kazakhstan lowers the value of M_s compared with that of the explosion by itself. Sykes and Ekstrom (1989) correct their M_s estimate by adding a factor of 0.15 due to tectonic release on an assumed reverse fault for the Soviet JVE event. This correction of M_s changes their yield based purely on M_s from 101 kilotons (kt) to 145 kt. Our observations however, imply that the strike-slip model is more appropriate for this particular explosion, so that the correction used by Sykes and Ekstrom (1989) may overestimate the M_s yield of the Soviet JVE.

Although previous large tectonic release events show a reverse mechanism, there is some evidence for a strike-slip stress regime in the East Kazakhstan region. Pooley et al. (1983) analyzed a suspected earthquake that occurred in 1976 less than 100 km from the JVE site and found it fit an oblique-slip on a northwest striking, steeply dipping plane. They also noted the nearby presence of the Chingiz fault, a right-lateral strike-slip fault striking N40° W.

The results of this study are based on some simple forward modeling of the regional broadband seismic recordings at two stations. Two end member models of tectonic release were modeled: vertical strike-slip and reverse faulting on a 45° dipping plane. We used the synthetic seismograms to determine the relative excitation of the SV and SH parts of the S_mS phase for each of these models. Although the character of
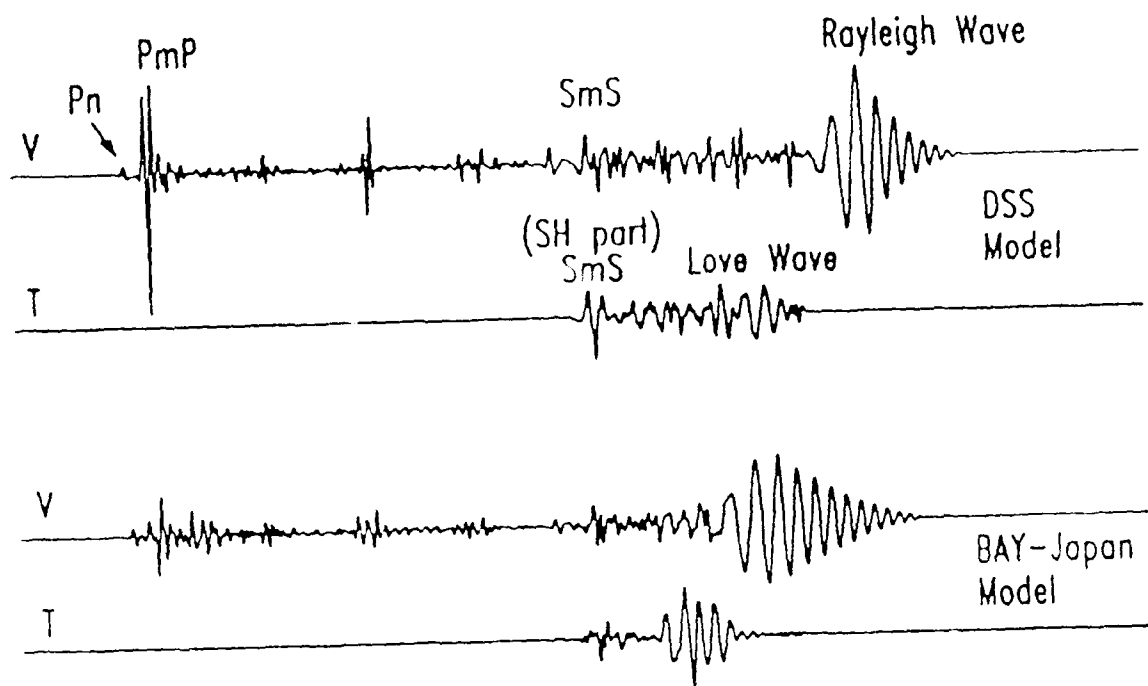
Fig. 11. Synthetic seismograms at BAY azimuth and distance for the two different velocity models discussed in the text.

the S_mS phases are not completely matched, the strike-slip model of tectonic release comes much closer to matching the relative amplitudes observed in the data than the reverse model. The modeling included the simplifying assumptions of step function source time dependence and the co-location and simultaneity of the explosion and tectonic events. Additional complexities such as spall were not considered. The use of other regional data and more tectonic release models, such as oblique fault slip and dip, will be needed to further evaluate the tectonic release from the Soviet JVE. A source inversion of this near regional data will be the subject of future work

References

Brune, J. N., and P. Pomeroy, Surface wave radiation for underground nuclear explosions and small magnitude earthquakes, *J. Geophys. Res.* 68, 5005-5028, 1963.

Given, J., and G. Mellman, Source parameters of Shagan river East Kazakh, USSR events using surface wave observations, in *The VELA program*, edited by A. Kerr, pp. 705-710, Defense Advanced Research Projects Agency, 1985.

Helle, H., and E. Rygg, Determination of tectonic release from surface waves generated by nuclear explosions in Eastern Kazakhstan, *Bull. Seism. Soc. Am.*, 74, 1883-1898, 1984.

Muller, G., The reflectivity method: a tutorial, *J. Geophys.*, 58, 153-174, 1985.

Murphy, J., and C. Archambeau, Variability in explosion body wave magnitudes: an analysis of the Rulison/Gasbuggy anomaly, *Bull. Seism. Soc. Am.*, 76, 1087-1113, 1986.

Press, F. and C. Archambeau, Release of tectonic strain by underground nuclear explosions, *J. Geophys. Res.*, 67, 337-343, 1962.

Patton, H., Source models of the Harzer explosion from regional observations of fundamental-mode and higher mode surface waves, *Bull. Seism. Soc. Am.*, 78, 1133-1157, 1988.

Pooley, C., A. Douglas, and R. Pearce, The seismic disturbance of 1976 March 20, East Kazakhstan: earthquake or explosion?, *Geophys. J. R. Astr. Soc.*, 74, 621-631, 1983.

Priestley, K., G. Zandt, and G. Randall, Crustal structure in Eastern Kazakh, U.S.S.R. from teleseismic receiver functions, *Geophys. Res. Lett.*, 15, 613-616, 1988.

Priestley, K., W. Walter, V. Martynov, and M. Rozhkov, Regional seismic recordings of the Soviet nuclear explosion of the joint verification experiment, *Geophys. Res. Lett.*, 17, 179-182, 1990.

Rygg, E., Anomalous surface waves from underground explosions, *Bull. Seism. Soc. Am., 69*, 1995-2002, 1979.

Saikia, C., A. Kafka, S. Gnewuch, and J. McTigue, Shear wave velocity and attenuation structure of the shallow crust in southeastern New England from dispersion of R_g waves, *submitted to J. Geophys Res.*, 1989.

Sykes, L., and G. Ekstrom, Comparison of seismic and hydrodynamic yield determinations for the Soviet joint verification experiment of 1988, *Proc. Natl. Acad. Sci. USA, 86*, 3456-3460, 1989.

Takeuchi, H, and M. Saito, Seismic surface waves, in *Methods in Computational Physics*, B. Bolt, Editor, Academic Press, New York, 217-295, 1972.

Toksoz, M., C. Thomson, and T. Ahrens, Generation of seismic waves by explosions in prestressed media, *Bull. Seism. Soc. Am., 61*, 1589-1623, 1971.

SECTION C

The Spectra of Seismic Radiation from a Tensile Crack

William R. Walter and James N. Brune

Seismological Laboratory, Mackay School of Mines, University of Nevada, Reno

Abstract

A model for the average far-field P and S wave amplitude spectra from a circular crack failing in tension is presented. The model explicitly avoids specifying the details of the rupture process, instead the spectral amplitude is determined by applying physically realistic constraints to an idealized spectral shape for each wave type. The idealized spectral form is given by: $\Omega_o / (1 + (\omega/\omega_c)^2)$ where ω_c is a parameter representing the corner frequency and the parameter Ω_o determines the overall scaling of the spectra. The P and S spectral models are constrained by fixing the low frequency level of each to be equivalent to a point source. They are further constrained by equating the total radiated energy with the available elastic energy. A final constraint between the corner frequencies of the P and S spectra is needed to completely determine the four free parameters. For the type of model considered here: an equidimensional fault with greatest displacement in the center we expect the P to S corner frequency ratio to range between 1 and 1.73 depending on the details of the rupture. This model gives an average S/P amplitude spectrum ratio that is about 2.1 at very low frequencies and between 2.1 and 0.7 at very high frequencies, depending on the P to S corner frequency ratio. Applying the same criteria to a circular shear crack we show that the average S/P amplitude is about 7.1 at very low frequencies and between 7.1 and 2.4 at very high frequencies, again depending on the S to P corner frequency ratio. The tensional crack thus has a lower average S/P ratio than the shear crack, and such low S/P ratios may be an identifying characteristic of tensile or tensile-equivalent rupture. Using the shear and tensional models we construct composite spectra that have significantly smaller S/P ratios than the shear cracks alone although the tensional events radiate less than 10 per cent of the total radiated energy. The tension crack average spectral model presented here may be useful as a first approximation for modeling seismic sources with a volumetric component in them, such as magma injection, or slip on a non-planar fault.

Introduction

41

Conceptually most of the sources of naturally occurring seismic radiation in the earth have been modeled as shear slip on a perfectly planar surface. However observations of exposed faults show they are often not continuous, not straight and not smooth (e.g. Aviles and Scholtz, 1986; Segall and Pollard, 1980). Shear slip occurring on such non-planar surfaces might be expected to contain a significant amount of motion normal to the shear slip direction. For example a fault plane containing a bend should tend to form a new fault at the bend in order to avoid a stress singularity (Andrews, 1989). During shear slip this triple junction must undergo a volume change, which might either be an opening or some complex local deformation in the vicinity of the junction. Other sources of seismic radiation might be more explicitly related to volumetric changes such as magma injection or the loss of compressional strength in a region. As a first approximation to these volumetric sources of seismic radiation we develop a model of the average spectra radiated by a circular crack failing in tension.

While shear crack models of seismic radiation by earthquakes have proven very successful, some observations, particularly small S to P ratios at high frequencies remain inadequately explained by such models. Recent observations of anomalous S to P ratios near Anza, California (Vernon et al., 1991) and Guerrero, Mexico (Castro et al., 1991) seem to be due, at least in part, to a source effect. These investigators have speculated that motions normal to the fault plane may be causing the anomalously low ratios. The idea of earthquakes containing some tensional motions goes back to Haskell (1964), who suggested that in order to explain the observed ratio of short period S to P ratios earthquakes should be modeled as the sum of subevents, some shear and some tensional. This idea was later extended by Blandford (1975) to explain other observations such as the robustness of the m_b:M_s earthquake/explosion discriminant and high P/S corner frequency ratios.

For some physical processes expected to generate seismic waves, source types other than shear on a plane are expected. For example magmatic processes have been modeled as a compensated linear vector dipole which can be decomposed into a tensile crack plus a pure volume expansion. Some observers have found volumetric components in moment tensor inversions of with long period data in volcanic volcanic regions (e.g. Julian, 1983; Aki 1984) but the interpretation of these results as non-shear sources is controversial (Wallace 1985). As pointed out by Wallace (1985) it is impossible to resolve volumetric change in a source using wavelengths longer than the source depth. Recently Patton and Zandt, (1991) have found a small (17 per cent) but significant volumetric component from surface wave moment tensor inversions of earthquakes within the Basin and Range.

A number of investigators have shown both theoretically (Odens and Martin, 1985, Lomnitz-Adler 1991) and observationally (Tolstoi, 1967) that slip on a rough surface generates motion normal to the plane of slip leading to reduced effective normal stress and thus reduced friction. This reduction of effective normal stress has been proposed as playing a major role in stick-slip sliding expected during earthquakes (Brune, Johnson and Slater, 1990; Melosh, 1979). These normal motions might reasonably be approximated by a number of tensile sub-events added to the overall shear event. These tensile sub-events might change the observed spectra from that expected for a pure shear source.

In this paper we will first determine a model for the average amplitude spectra of seismic radiation from a circular tensional failure. In contrast with other tensional failure models (e.g. Haskell, 1964, Blandford, 1975) we do not attempt to explicitly define the rupture location and velocity, but rather assume a physically realistic spectral shape and use basic energy, point source and corner frequency relations to constrain the models free parameters. Because the rupture and slip time histories remain unspecified we cannot make any conclusions regarding the change in spectral shape with azimuth due to a directivity effect (e.g. Boatwright, 1980). The spectral model used here represents an average over azimuth. In fact at relatively high frequencies it has been proposed that the rupture velocity undergoes abrupt changes due to stress (e.g. Madariaga, 1983) or frictional (e.g. Segall and Pollard, 1980) heterogeneities. Therefore simple constant rupture models of directivity may not be applicable at high frequencies, and the average amplitude used here may be more appropriate.

The approach used here is similar to, but more general than that used by Brune (1970) and Randall (1973) for a circular shear crack. Brune used an energy balance criteria but determined only the S wave spectrum. Randall (1973) assumed 100 per cent conversion of elastic energy to radiated energy and fixed the P to S corner frequency at the ratio of the wave velocities. For our tensional crack model we allow both to vary. We then apply the same analysis to a circular shear crack and compare the spectra from the two types of events. Finally we construct some composite models containing both shear and tensile faulting.

Model

We shall assume an idealized far-field displacement spectral amplitude model for the average seismic radiation from a tensile crack of the form:

$$|\Omega^P(\omega)| = \frac{\Omega_o^P}{1 + (\omega/\omega_c^P)^2} \, , \quad |\Omega^S(\omega)| = \frac{\Omega_o^S}{1 + (\omega/\omega_c^S)^2} \tag{3.1}$$

where Ω_o^P, Ω_o^S, ω_c^P, and ω_c^S are parameters to be determined by physical constraint equations. The phase spectrum remains unspecified so that in the time domain a variety of pulse shapes will have this amplitude spectrum. While the choice of model is somewhat arbitrary, this model is about the simplest form of a displacement spectrum that has the correct asymptotic behavior. It approaches a constant value (neglecting near-field terms) as $\omega \to 0$ that is proportional to the moment, and as $\omega \to \infty$ it falls off as ω^{-2} which is steeper than the $\omega^{-1.5}$ needed to keep the radiated energy finite. This model has been applied successfully to many earthquakes being modeled as shear cracks. We have no apriori reason to use a different spectral model in the case of a tensile crack failure and therefore will assume this model in the following analysis. In an appendix we show that the same analysis can be applied to spectral models similar to those described by equation (3.1) but with a different high frequency falloff rate. The adoption of a different high frequency falloff rate slightly changes the corner frequency scaling constants but does not otherwise affect our analysis.

The geometry for the tensional failure considered here is that of a circular crack in the interior of an infinite elastic medium. The crack occupies a circle of radius a in the $x_1 - x_2$ plane as shown in Figure 13. The crack is formed by axially symmetric tension along the x_3-axis (σ_3), which is perpendicular to the plane of the crack. The displacements and elastic energy change from a circular or "penny shaped" crack failing in tension was first solved by Sack (1946) in oblate spheroidal coordinates. Sneddon (1951) gives a solution in the more tractable cylindrical coordinates. The net opening in the x_3-direction across the crack is given by (Sneddon, 1951):

$$\Delta u_3(r) = \frac{3\,\sigma_3}{\pi\,\mu} \sqrt{a^2 - r^2} \qquad (3.2)$$

where we have assumed the Lame constants λ and μ are equal (Poisson's ratio is 1/4). From equation (3.2) it is apparent that the maximum displacement, which we denote as ε, occurs at the origin. The average displacement can also be obtained from equation (3.2) and is 2/3 ε. We note that the displacements given by equation (3.2) are independent of the stress σ_1 and σ_2. We also note that the displacements of the circular crack in a uniaxial tensional field are equivalent to those generated by a circular crack formed by a uniform internal pressure.

The first constraint equation is provided by the elastic energy available to be radiated. The energy difference between the intact medium and one containing a circular tension crack is (Sneddon, 1951):

$$W_{elastic} = \frac{\sigma_3^2 a^3}{\mu} = \frac{\pi^2 \mu \varepsilon^2 a}{9}. \qquad (3.3)$$

Equation (3.3) represents the total energy available for seismic radiation, the rupture of atomic bonds and any other energy consumptive processes that occur during the tensile failure. The seismically radiated energy is given by:

$$W_{rad} = 2\rho R^2 \left[\alpha \int_{-\infty}^{\infty} |\,\Omega^P(\omega)\,\omega\,|^2 d\omega + \beta \int_{-\infty}^{\infty} |\,\Omega^S(\omega)\,\omega\,|^2 d\omega \right] \qquad (3.4)$$

where α and β are the P and S wave velocity, ρ represents the medium density, and R is the distance from the crack to where the seismic waves are recorded. Using the spectral shapes from equation (3.1) the first constraint equation is obtained by setting (3.3) equal to (3.4) via a constant f which represents the fraction of the elastic energy that goes into seismic radiation:

$$\pi \rho R^2 \left[\alpha (\Omega_0^P)^2 (\omega_0^P)^3 + \beta (\Omega_0^S)^2 (\omega_0^S)^3 \right] = \frac{f \sigma_3^2 a^3}{\mu}. \qquad (3.5)$$
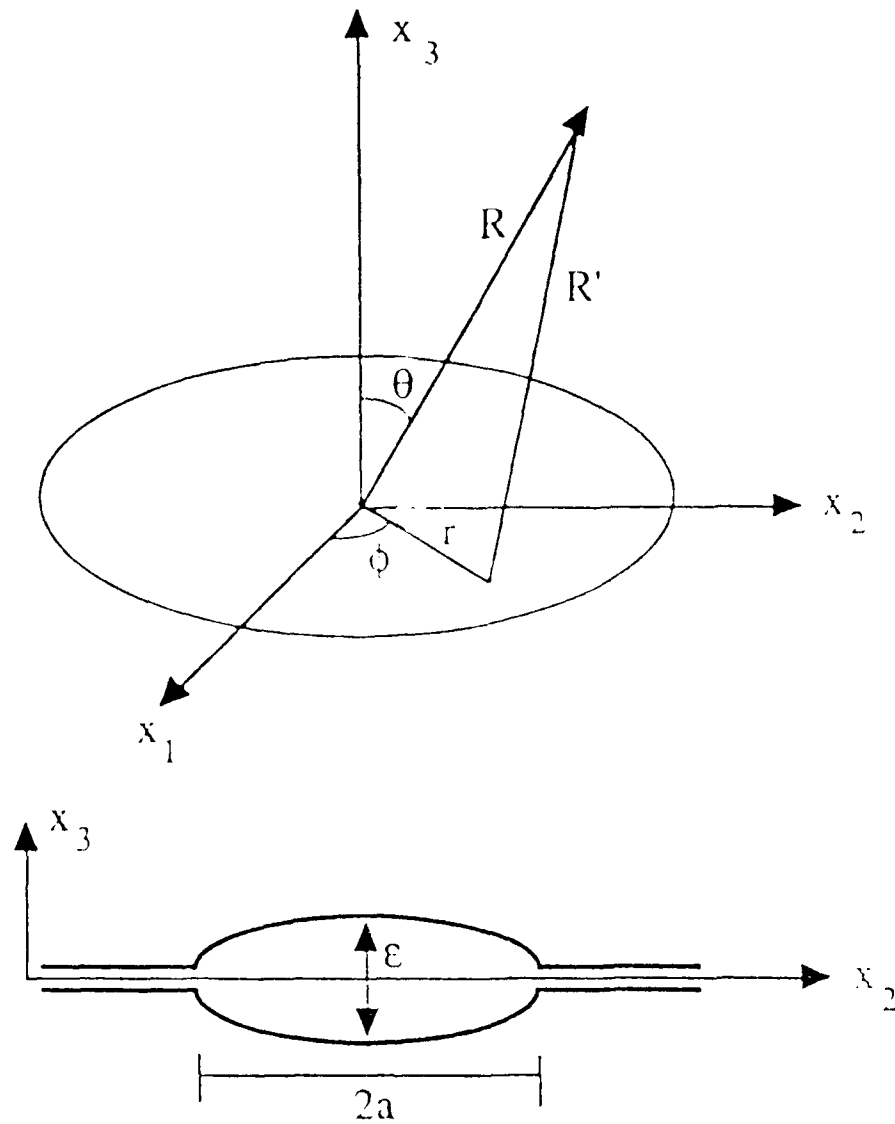
Fig. 12. The coordinate system for the tensile crack model. The circular crack of radius a lies in the x1-x2 plane, centered at the origin. In side view the deformation in the x3 direction is elliptical with the maximum opening of ε, occurring at the center of the crack. We shall assume a $>> \varepsilon$ so that the crack is approximately planar. The radiation is observed at a point at distance R and angle Θ from the origin and a distance R' from a specfic point specified by r and Φ on the plane of the crack.

If the circular crack were opened by a sudden internal pressure of magnitude σ_3 instead of external tension the displacement in the x_3 direction is still described by equation (3.2). The work done by this internally driven crack is given by the pressure times the area times the average deformation:

$$W = (\sigma_3)(\pi a^2)(\frac{2}{3}\epsilon) = \frac{2\pi a^2 \sigma_3 \epsilon}{3} = 2\frac{\sigma_3^2 a^3}{\mu}. \tag{3.6}$$

This is twice the energy in the equation (3.3). Thus only half of this energy goes into deforming the medium and the rest, the same amount as in equation (3.3) is available for seismic radiation.

The second and third constraint equations come from assuming that the source approaches a point source as the frequency of seismic radiation goes to zero. We shall limit ourselves to considering only those cases where a $>>$ ϵ so that the failure can be approximated as occurring on a plane at $x_3 = 0$. We will also assume that the source to receiver distance is large compared with the radius of the crack (R $>>$ a) and that we are in the far-field for frequencies of interest. The moment density tensor is then given by (Aki and Richards, 1980; equation 3.20):

$$\mathbf{m} = \begin{bmatrix} \lambda & 0 & 0 \\ 0 & \lambda & 0 \\ 0 & 0 & \lambda+2\mu \end{bmatrix} \Delta u_3(r, \phi, t). \tag{3.7}$$

The far-field, whole-space displacement is then given by Aki and Richards (1980) equations 3.19 and 14.4:

$$u_n = \iint_S m_{pq} * G_{n,p,q} \, dS$$

$$= \iint_S \left[\frac{\gamma_n \gamma_p \gamma_q}{4\pi\rho\alpha^3 R} \mu \Delta \dot{u}_3(t - \frac{R'}{\alpha}) - \frac{\gamma_q(\gamma_n \gamma_p - \delta_{np})}{4\pi\rho\beta^3 R'} \mu \Delta\dot{u}_3(t - \frac{R'}{\beta}) \right] dS \tag{3.8}$$

where m_{pq} is an element of the moment density tensor, G represents the Green's function, S the area of the crack and the asterisk represents a convolution. Each γ represents a directional cosine of the radiation from the source, $\gamma_i = \partial R'/\partial x_i$. Since we assumed that R $>>$ a the directional cosines are approximately constant and independent of r and ϕ, and can be taken outside of the integral. Solving for the magnitude of the separate P and S displacements and taking the Fourier transform of the results we obtain:

$$\Omega^P(\omega) = \frac{(1 + 2\cos^2\theta)\mu}{4\pi\rho\alpha^3 R} \iint_S \Delta\dot{u}_3(r, \phi, \omega) e^{i\omega R'/\alpha} \, dS \tag{3.9}$$

46

for the far-field P wave spectra, and

$$\Omega^S(\omega) = \frac{(2\sin\theta\cos\theta)\mu}{4\pi\rho\beta^3 R} \iint_S \Delta\dot{u}_3(r,\phi,\omega)\, e^{i\omega R'/\beta}\, dS \tag{3.10}$$

for the far-field S wave spectra, where

$$\Delta\dot{u}_3(r,\phi,\omega) = \int_{-\infty}^{\infty} \Delta\dot{u}_3(r,\phi,t)\, e^{i\omega t}\, dt. \tag{3.11}$$

In the above equations θ is defined in Figure 13. As the $\omega\to 0$ the far-field spectra given in equations (3.9) and (3.10) approach a constant value, proportional to the integral of the final offset of Δu_3 over the area of the tensile crack and independent of the time history. Using the final offset for a circular fault given by equation (3.2) we can equate the model in equation (3.1) with the far-field spectra given by equations (3.9) and (3.10) at $\omega=0$ to obtain:

$$|\Omega^P(\omega=0)| = (1+2\cos^2\theta)\frac{\sigma_3 a^3}{2\pi\rho\alpha^3 R} = \Omega_o^P \tag{3.12}$$

and

$$|\Omega^S(\omega=0)| = (2\sin\theta\cos\theta)\frac{\sigma_3 a^3}{2\pi\rho\beta^3 R} = \Omega_o^S. \tag{3.13}$$

The factors of $1+2\cos^2\theta$ and $2\sin\theta\cos\theta$ appearing in the above equations are the point source radiation patterns of a tensile crack. The radiation pattern amplitudes are shown in Figure 14, note the S-wave nodes in the plane and perpendicular to the plane of the crack. The P wave radiation pattern does not have any radiation pattern nodes. In order to use equations (3.12) and (3.13) to determine the energy content of the seismic radiation a mean square value of the radiation pattern must be determined. Averaging over the whole focal sphere:

$$<(1+2\cos^2\theta)^2> = \frac{3}{4\pi R^2}\int_0^\pi (1+2\cos^2\theta)^2\, \frac{2\pi R^2}{3}\sin\theta\, d\theta = \frac{47}{15} \tag{3.14}$$

and

$$<(2\cos\theta\sin\theta)^2> = \frac{3}{4\pi R^2}\int_0^\pi (2\cos\theta\sin\theta)^2\, \frac{2\pi R^2}{3}\sin\theta\, d\theta = \frac{8}{15} \tag{3.15}$$
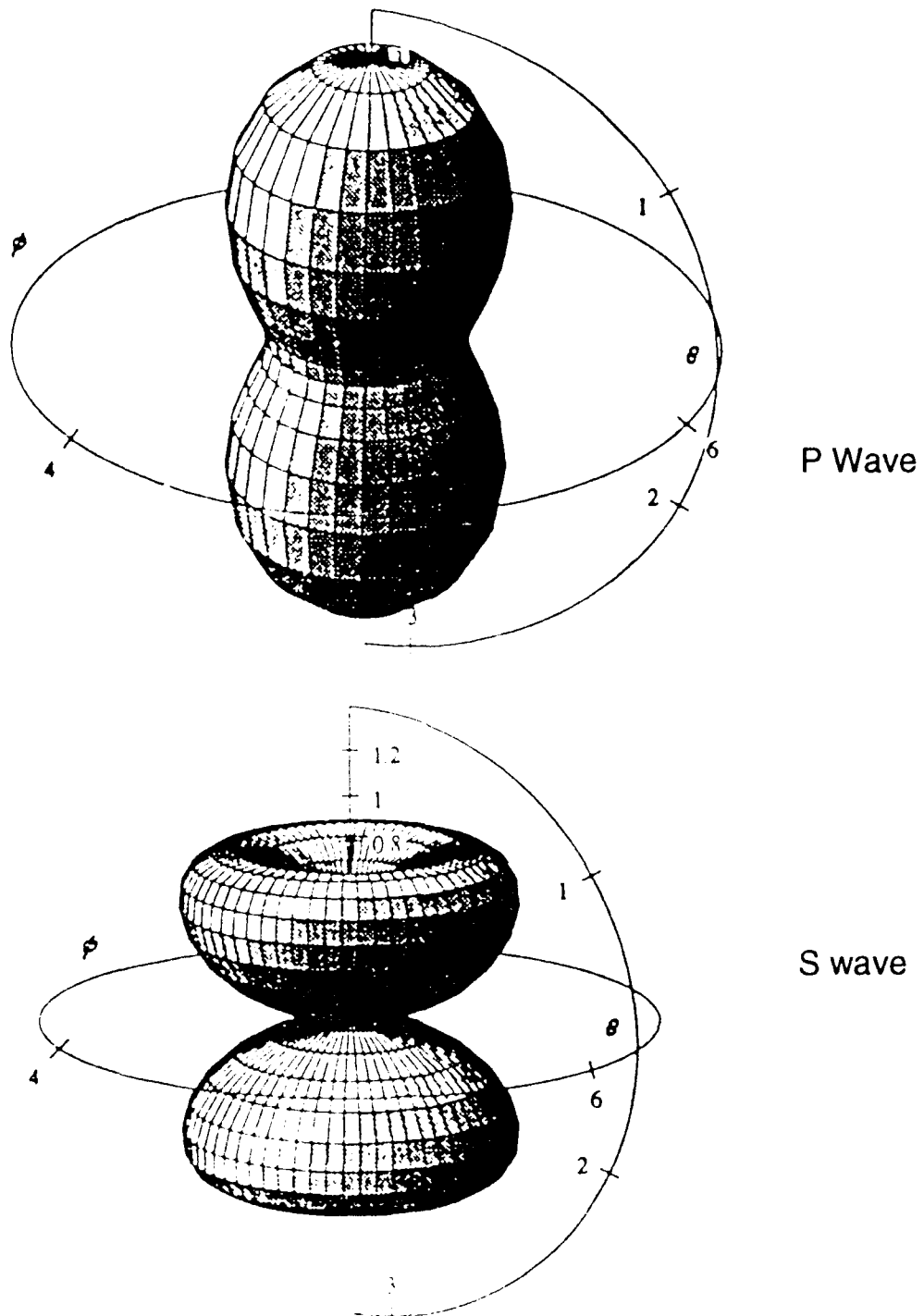
47

P Wave

S wave

Fig. 13. P and S point source radiation patterns for the tensile crack. The crack plane is indicated by the circle.

Equations (3.5), (3.12) and (3.13) represent 3 constraints on the four unknowns in our model, given by equation (3.1). One further constraining equation is needed before we can solve for the unknowns in the model. The final constraining equation must relate the P and S corner frequencies to each other. The physical reason for corner frequencies can be seen by examining the form of equations (3.9) and (3.10). These equations are in the form of one Fourier transform in time and two in space. Thus corner frequencies arise because of the finite duration of faulting as well as the finite area of faulting. For an equidimensional fault with rupture velocity on the order of the shear wave velocity, the corner frequencies associated with the two spatial transforms and the one time transform should be similar and consistent with our spectral model assumption given by (3.1).

As discussed by Sato and Hirasawa (1973), a seismic source which undergoes greater displacement over a longer time in the center of the crack than at the edges leads to a larger P wave corner frequency than the S wave corner frequency. Molnar et al. (1973) showed that in the case of instantaneous rupture the P to S corner frequency ratio is equal to the P to S wave velocity ratio. We can represent the P wave corner frequency as some constant, g times the S wave corner:

$$\omega_c^P = g\ \omega_c^S \tag{3.16}$$

where we expect g to fall in the range from $1 < g < \alpha/\beta$ or between 1 and $\sqrt{3} \approx 1.73$. Using (3.16) as our last constraint equation we solve (3.5) for the S wave corner frequency:

$$\omega_c^S = \left[\frac{1620\,\pi\,f}{47\,\sqrt{3}\ g^3 + 216} \right]^{\frac{1}{3}} \frac{\beta}{a.} \tag{3.17}$$

The parameter f represents the fraction of elastic energy which goes into seismic radiation and might be expected to vary greatly. In constant rupture velocity models such as Sato and Hirasawa (1973) this fraction increases with faster rupture velocities. In general the energy radiated will be related to the form of $\Delta u_3(r, \phi, t)$ which might be quite complex and not adequately modeled by constant rupture velocity models. Errors in our choice for the parameter f will not change the low frequency spectral level but change the corner frequency by $f^{1/3}$ and the high frequency level by $f^{2/3}$. This effect is illustrated in Figure 15. In this paper we will assume that the energy partition between radiation and energy consumptive processes such as rupture of atomic bonds is approximately equal and $f \approx 0.5$. Let us examine some specific cases for the corner frequency ratio given by (3.16).

Case $g = \alpha/\beta$. If a rupture occurs rapidly enough so that the fault can be treated as radiating essentially instantaneously, then the P and S corner frequencies are proportional to the velocity divided by the fault dimension. This can be seen directly by substituting a delta function time dependence of Δu_3 into equations (3.9) and (3.10)
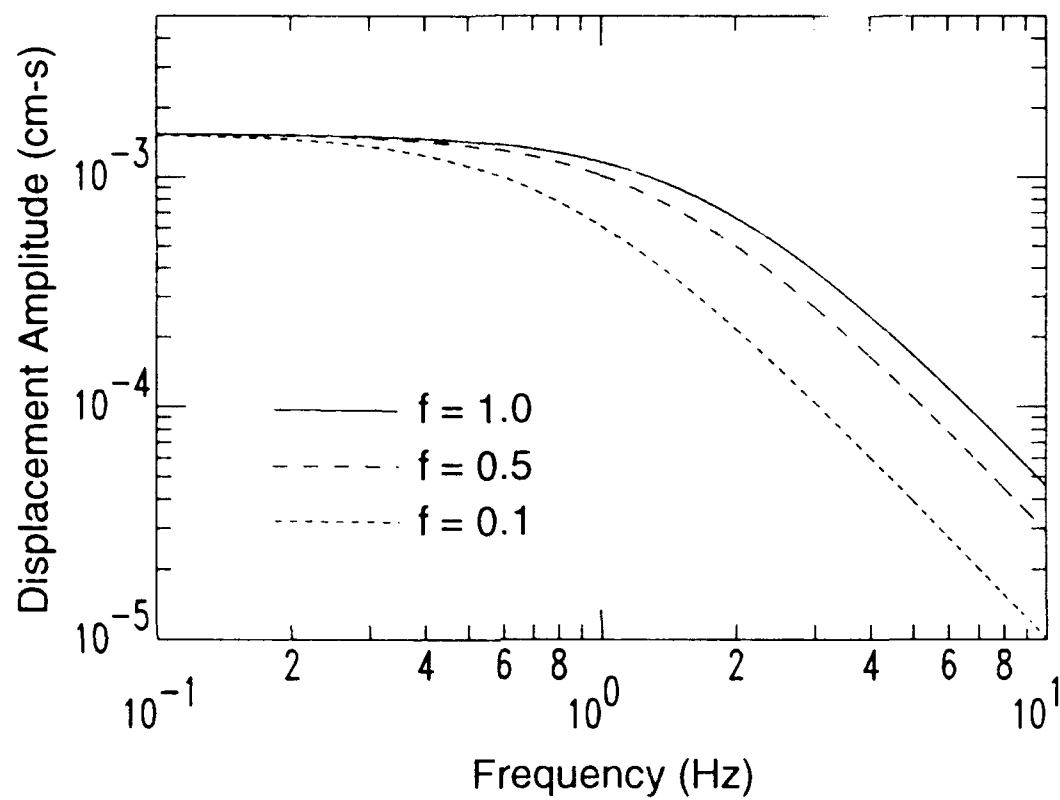
49

Fig. 14. Tensile P wave spectra for several values of the parameter f, the fraction
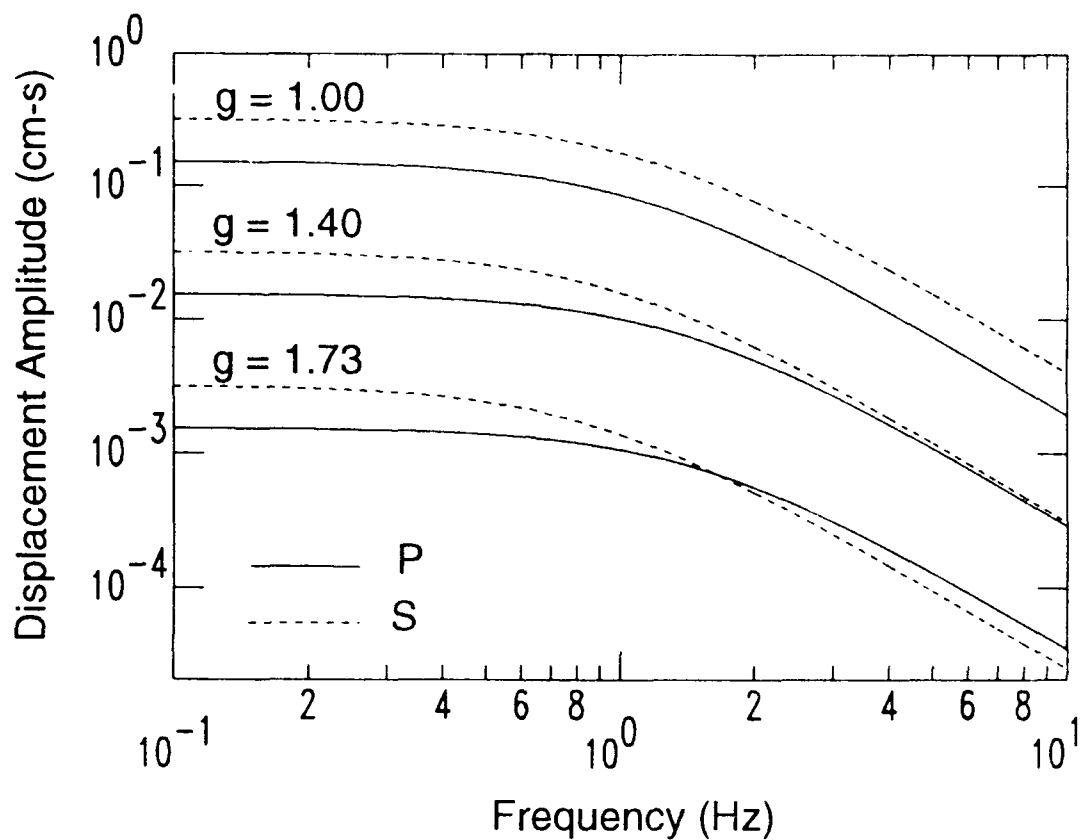of elastic energy radiated. All spectra were calculated for a 1km radius crack,
opening 1 cm.

Fig. 15. P and S spectral pairs for tensile crack model with three different values of g, the P to S corner frequency ratio. All spectra were calculated for a 1 km radius crack with 1 cm of maximum opening. Upper two pairs of spectra were multiplied by factors of 10 and 100 for display purposes.

51

(cf. Molnar et al., 1973). In this case the P to S corner frequency ratio will be equal to the P to S velocity ratio, or $g = \sqrt{3} \approx 1.73$. Using equation (3.17) we find an S wave corner frequency of $\omega_c^S = 1.59 \beta / a$ and a P wave corner frequency of $\omega_c^P = 1.59 \alpha / a$ The P and S wave spectra for this case are shown in Figure 16.

Case g = 1 . If the effective duration of rupture is long compared to the radius over the seismic wave velocity, then the observed corner frequency might be determined completely by the rupture time. This is equivalent to treating the crack as a point source (R′ = R) for the frequencies of interest, so that the corner frequencies are determined only by the rupture time. In this case the corner frequencies are equal and g = 1.0. Using (3.17) and (3.16) the S and P corner frequencies are $\omega_c^S = \omega_c^P = 2.05 \beta / a$. Spectra for this case are shown in Figure 16

Case g = 1.4. We would now like to consider an intermediate case when g = 1.4. While this choice is somewhat subjective we are motivated by similar values for the P to S wave ratio obtained by a variety of investigators for a circular shear crack which involves solving integrals completely analogous to those appearing in equations (3.9) and (3.10) (e.g. Sato and Hirasawa, 1973, Molnar et al., 1973, Madariaga, 1976). The S and P wave corner frequencies are $\omega_c^S = 1.80 \beta / a$ and $\omega_c^P = 2.51 \beta / a$. Using equations (3.9) and (3.10) the far-field P and S wave amplitude spectra is given by:

$$|\Omega^P(\omega)| = (1 + 2\cos^2\theta)\frac{6.32}{2\pi}\frac{c}{R}\frac{\sigma_3\alpha}{9\mu}\frac{1}{\omega^2 + 6.32\beta^2/a^2} \tag{3.18}$$

$$|\Omega^S(\omega)| = (2\cos\theta\sin\theta)\frac{3.23}{2\pi}\frac{c}{R}\frac{\sigma_3\beta}{\mu}\frac{1}{\omega^2 + 3.23\beta^2/a^2} \tag{3.19}$$

The P and S wave spectra are shown in Figure 16.

The lithostatic pressure increases with depth approximately as 300 bars/km in the crust. At the 5-35 km depths where most crustal earthquakes occur the lithostatic pressure will be of the order of thousands of bars. During an earthquake one might expect some regions to be under local tensile stress during the event, perhaps due to shear slip on a non-planar fault or some other mechanism, which then returns to compressive stress after the event is over. In such a case we can model a circular region subject to short duration of tensile stress as an opening and closing crack. Making a simplifying assumption that the opening and closing crack displacement pulses are equal but opposite in sign, the far field displacement is given by:

$$u(t) = u_0(t) - u_0(t + \tau) \tag{3.20}$$

where u_0 is the far-field displacement of the opening crack and τ is the time the crack remains open. This simplifying assumption can lead to radiated energy that is about 20 per cent higher than twice the energy of the opening crack for particular values of τ. However, the values of τ we will use later in the paper give an energy for the opening

and closing case that is very nearly twice that of the opening case alone, justifying this simple assumption for our modeling purposes. Making use of the shift theorem we find our model magnitude spectra are multiplied by a factor of $(2 - 2\cos \omega \tau)^{(1/2)}$. This has the effect of reducing the low frequencies, leading to a displacement spectrum peaked near the corner frequency as shown in Figure 17.

Comparison with Shear Crack

The above analysis can just as easily be done for a circular shear crack. Let us consider a circular shear crack of radius a' in the x_1–x_2 plane subject to a uniform applied shear stress of magnitude σ which slips in the x_2 direction. The relative displacement across the faces of the crack is given by (Eshelby, 1957):

$$\Delta u_2 = \frac{24 \, \sigma_2}{7 \, \pi \, \mu} \sqrt{a'^2 - r^2} \tag{3.21}$$

again assuming Poisson's ratio is 1/4. Again the maximum displacement which we denote as ε', occurs at the origin. The energy difference between an intact infinite elastic medium and one containing a circular shear crack with the displacement specified by equation (20) is (Eshelby, 1957):

$$W'_{\text{elastic}} = \frac{8 \, \sigma_2^2 \, a'^3}{7 \, \mu} = \frac{7 \, \pi^2 \mu \, \varepsilon'^2 \, a'}{72} \tag{3.22}$$

We use the same spectral amplitude model as given in equation (2), with the parameters $\Omega_0^{P'}$, $\Omega_0^{S'}$, $\omega_c^{P'}$, and $\omega_c^{S'}$ denoted with primes to distinguish them from the tensile case. Applying the similar low frequency constraints and assuming a fraction, f' of the elastic energy is radiated and the P to S corner frequency ratio is given by g' we can solve for the four parameters:

$$\Omega_0^{P'} = R_{\Theta\Phi}^{P'} \frac{4 \, \sigma_2 \, a'^3}{7 \, \pi \rho \, \alpha^3 R} \tag{3.23}$$

$$\Omega_0^{S'} = R_{\Theta\Phi}^{S'} \frac{4 \, \sigma_2 \, a'^3}{7 \, \pi \rho \, \beta^3 R} \tag{3.24}$$

$$\omega_c^{P'} = g' \, \omega^{S'}_c \tag{3.24}$$

$$\omega_c^{S'} = \left(\frac{2835 \, \pi \, f'}{8 \sqrt{3} \, g'^3 + 324} \right)^{\frac{1}{3}} \frac{\beta}{a'} \tag{3.25}$$
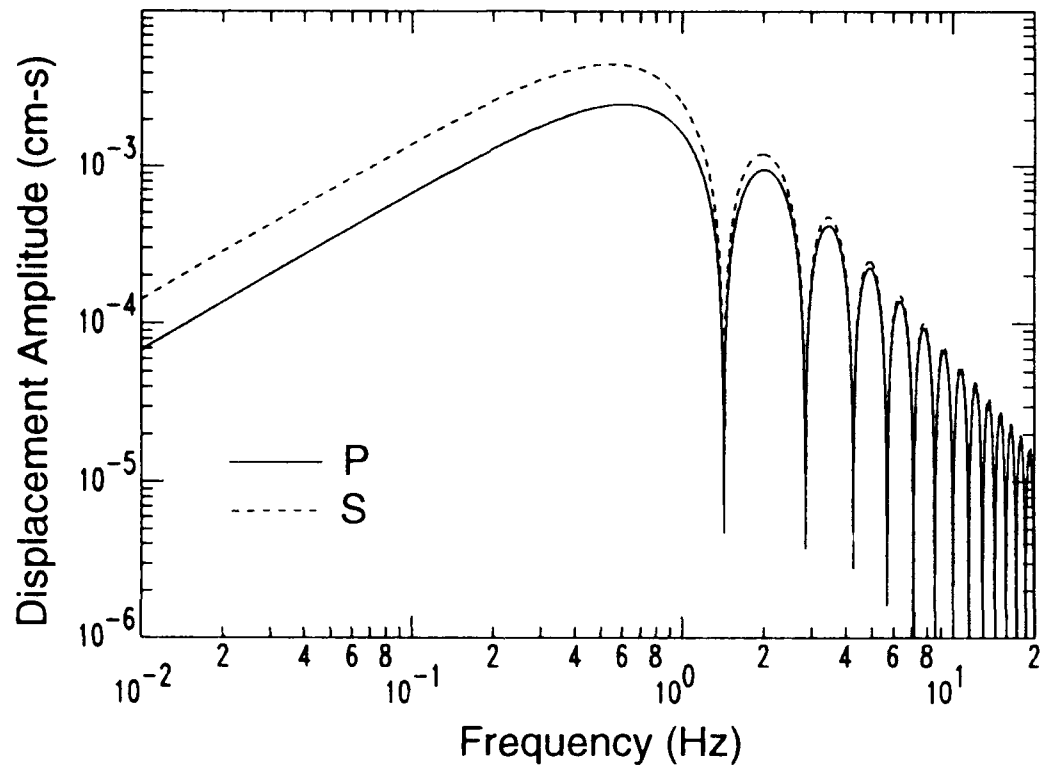
53

Fig. 16. Spectra of an opening and closing tensile crack. Calculated for a
1 km radius crack opening 1 cm in 0.7 seconds then closing.

where $R^{P'}_{\Theta\Phi}$ where $R^{S'}_{\Theta\Phi}$ are the P and S point source radiation patterns for a shear crack (cf. Aki and Richards, 1981). We note that if $f' \approx 0.5$ we obtain values for $\omega_c^{S'}$ close to the Brune (1970, 1971) value of $2.34\,\beta/a'$. For example $f' = 0.5$ and $g' = 1.4$ yields $\omega_c^{S'} = 2.31\,\beta/a'$.

We have assumed that the general spectral shape for pure shear and pure tensile cracks are similar. If these models are correct then predicted observational differences between the two types of events will be mostly due to radiation pattern differences. In addition to differences in the spatial character, the radiation patterns should also lead to large differences in the observed S to P spectral amplitude ratios. At very low frequencies ($\omega << \omega_c^S$) and very high frequencies ($\omega >> \omega_c^P$) the P to S spectral amplitude ratio has the same form for both the shear and tensile crack cases. The tensile crack S/P ratios are:

$$\frac{|\Omega^S(\omega \to 0)|}{|\Omega^P(\omega \to 0)|} = \frac{R^S_{\Theta\Phi}}{R^P_{\Theta\Phi}}\frac{\alpha^3}{\beta^3}, \quad \frac{|\Omega^S(\omega \to \infty)|}{|\Omega^P(\omega \to \infty)|} = \frac{R^S_{\Theta\Phi}}{R^P_{\Theta\Phi}}\frac{\alpha^3}{g^2\beta^3}, \tag{3.26}$$

where $R^S_{\Theta\Phi}$ and $R^P_{\Theta\Phi}$ are the S and P wave radiation patterns. The shear crack ratios are of similar form to (3.26) with $R^{S'}_{\Theta\Phi}$, $R^{P'}_{\Theta\Phi}$ and g' replacing $R^S_{\Theta\Phi}$ $R^P_{\Theta\Phi}$ and g. For the tensile case $<|R^S_{\Theta\Phi}|> = 2/3$ and $<|R^P_{\Theta\Phi}|> = 5/3$ so that at low frequencies the S to P spectral amplitude ratio is about 2.1. At high frequencies the ratio varies from about 2.1 to about 0.69 as g varies from 1.00 to 1.73. The tensile crack S/P ratio is shown in Figure 18a for three specific values of g. The average magnitude of the shear crack radiation patterns is $<|R^{S'}_{\Theta\Phi}|> = 0.60$ and $<|R^{P'}_{\Theta\Phi}|> = 0.44$ (Boore and Boatwright, 1984) so that at low frequencies the S to P spectral amplitude ratio is about 7.1 and the high frequency S/P ratio varies from 7.1 to 2.4 as g' goes from 1.00 to 1.73. The shear crack S/P spectral ratio is shown in Figure 18b for three values of g'. These large differences in S/P ratios may be an identifying characteristic of tensile events.

Composite Events

Some earthquakes near Anza, California (Vernon et al., 1991) and Guerrero, Mexico (Castro et al., 1991) have been observed to have high frequency S/P ratios less than two. As shown in Figure 18b the lowest S/P ratio expected from a pure shear source when averaged over the focal sphere has a value of about 2.4. These investigators show that attenuation estimates for these areas are insufficient to explain the anomalously low values by themselves and favor at least a partial source explanation. We use the above developed tensile and shear models to estimate how much tensile motion relative to shear slip is necessary to cause anomalous S/P ratios.

The presence of S wave nodes in the shear crack radiation pattern and the absence of P wave nodes in the tensile crack radiation pattern means that even small amounts of tensile motion in a composite event may be apparent if the observing station is at a particular angle from the fault plane. However scattering and a non-uniform rupture velocity, even for a pure shear seismic source might be expected to obscure a
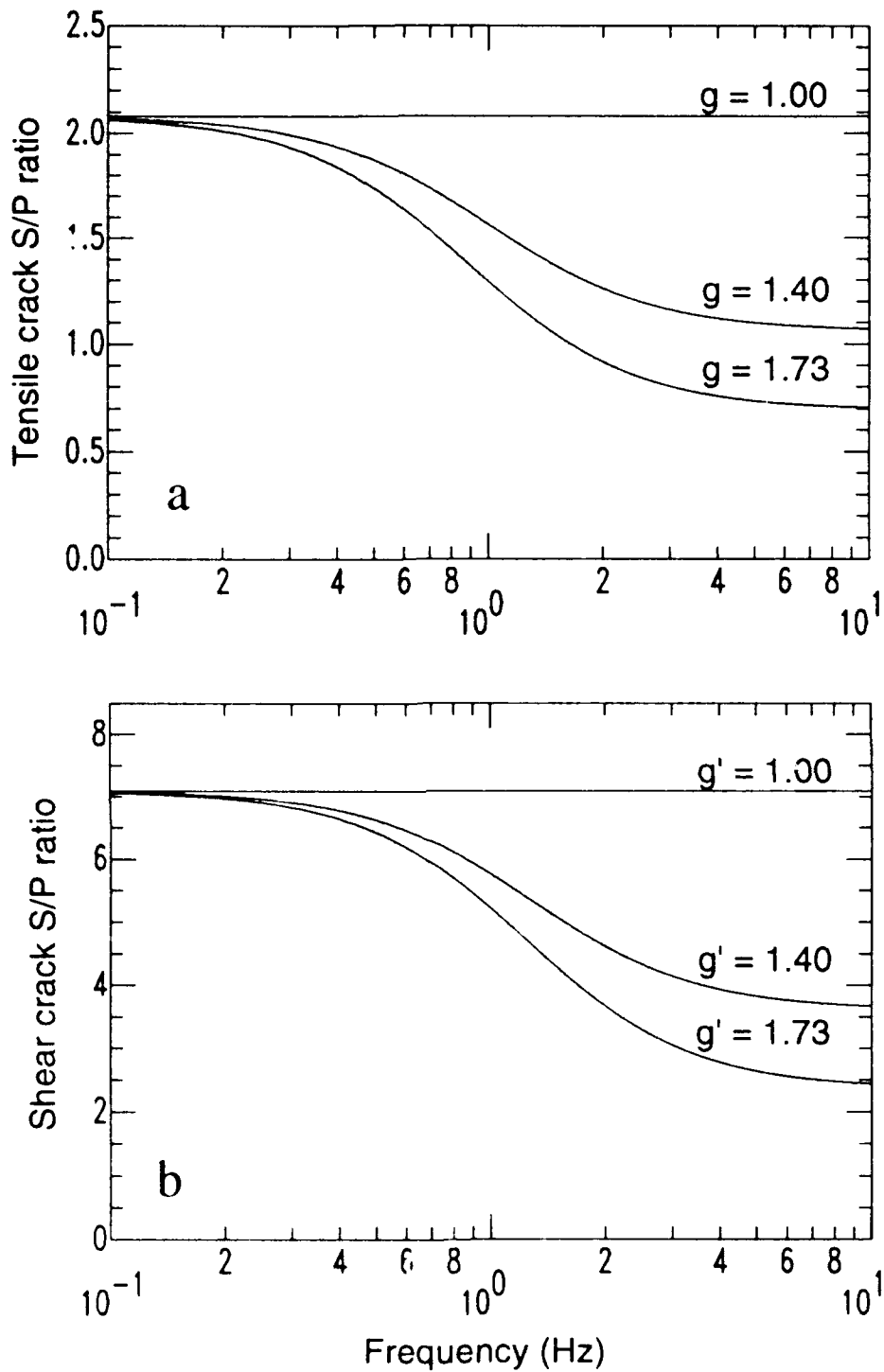
Fig. 17. S/P spectral ratios. (a) Tensile crack model S/P ratio for three values of P/S corner frequency ratio, g . (b) Shear crack S/P ratio for same three values of P/S corner frequency ratio, g'.

simple point source radiation pattern, particularly at high frequencies. Liu and Helmberger (1985) have noted that the high frequency P wave radiation pattern of earthquakes is more homogeneous than that observed at lower frequencies. Therefore, we will compare the magnitude of the tensile and shear models when averaged over the focal sphere. Taking the ratio of shear crack to tensile crack P wave displacement spectra at high frequencies $(\omega>>\omega_c^P$ and $\omega>>\omega_c^{P'})$ we find:

$$\frac{|\Omega^{P'}(\omega\to\infty)|}{|\Omega^P(\omega\to\infty)|} = \frac{\Omega_o^{P'}}{\Omega_o^P}\frac{(\omega_c^{P'})^2}{(\omega_c^P)^2} = \frac{R_{\Theta\Phi}^{P'}}{R_{\Theta\Phi}^P}\frac{k'^2}{k^2}\frac{\varepsilon'}{\varepsilon} \qquad (3.27)$$

where we have used $\omega_c^{P'}=k'\beta/a'$ and $\omega_c^P=k\beta/a$. We define a significant contribution of tensile P energy as occurring when the shear to tensile P wave spectral ratio given in equation (27) is less then one. Using the average magnitudes of the shear and tensile point source P wave radiation patterns, a relative slip criterion is obtained from (27):

$$\varepsilon \geq 0.265\left[\frac{k'}{k}\right]^2\varepsilon'. \qquad (3.28)$$

For example assuming both the shear and tensile cracks have the same P to S corner frequency ratio of 1.4 $(g=g'=1.4)$ the relative slip criteria becomes $\varepsilon \geq 0.44\varepsilon'$. In other words if the shear crack has a maximum slip of 10 cm the tensile crack must have a maximum opening of 4.4 cm in order to have the same P wave displacement spectra at high frequencies. Of course the tensile crack does not have to consist of one large event but may be made up of many smaller subevents with total opening and closing displacements equal to 4.4 cm. If the smaller events add incoherently however, more total displacement may be necessary. In the case of opening and closing events the factor of $(2-2\cos(\omega\tau))^{1/2}$ multiplies the tensile crack opening in equation (3.28). This factor varies from 0 to 2 but at very high frequencies has an average value of $\sqrt{2}$. The relative slip criteria in equation (3.28) does not put any constraints on the radius of the tensile subevents. Equations (3.3) and (3.22) show the total energy of the cracks is proportional to the maximum displacement squared times the radius. Thus, although the total opening and closing displacements may be large, the radius and total energy of the subevents may be small compared with the shear radius and radiated energy.

As specific examples we construct composite events consisting of a 2 km radius shear crack which has a maximum of 10 cm of slip (corresponding to about a 30 bar stress drop) and several opening and closing tensile subevents which are assumed to be randomly distributed over the fault plane and thus over the duration of the shear event. As shown in Figure 17, the subevents are peaked near their corner frequency and are expected to have a significant contribution only at high frequencies. Therefore we use the approximation that the composite spectra are the square root of the sum of the squares of all the events (e.g. Joyner and Boore, 1986). This should be a conservative approximation of the contribution of the tensile subevents.
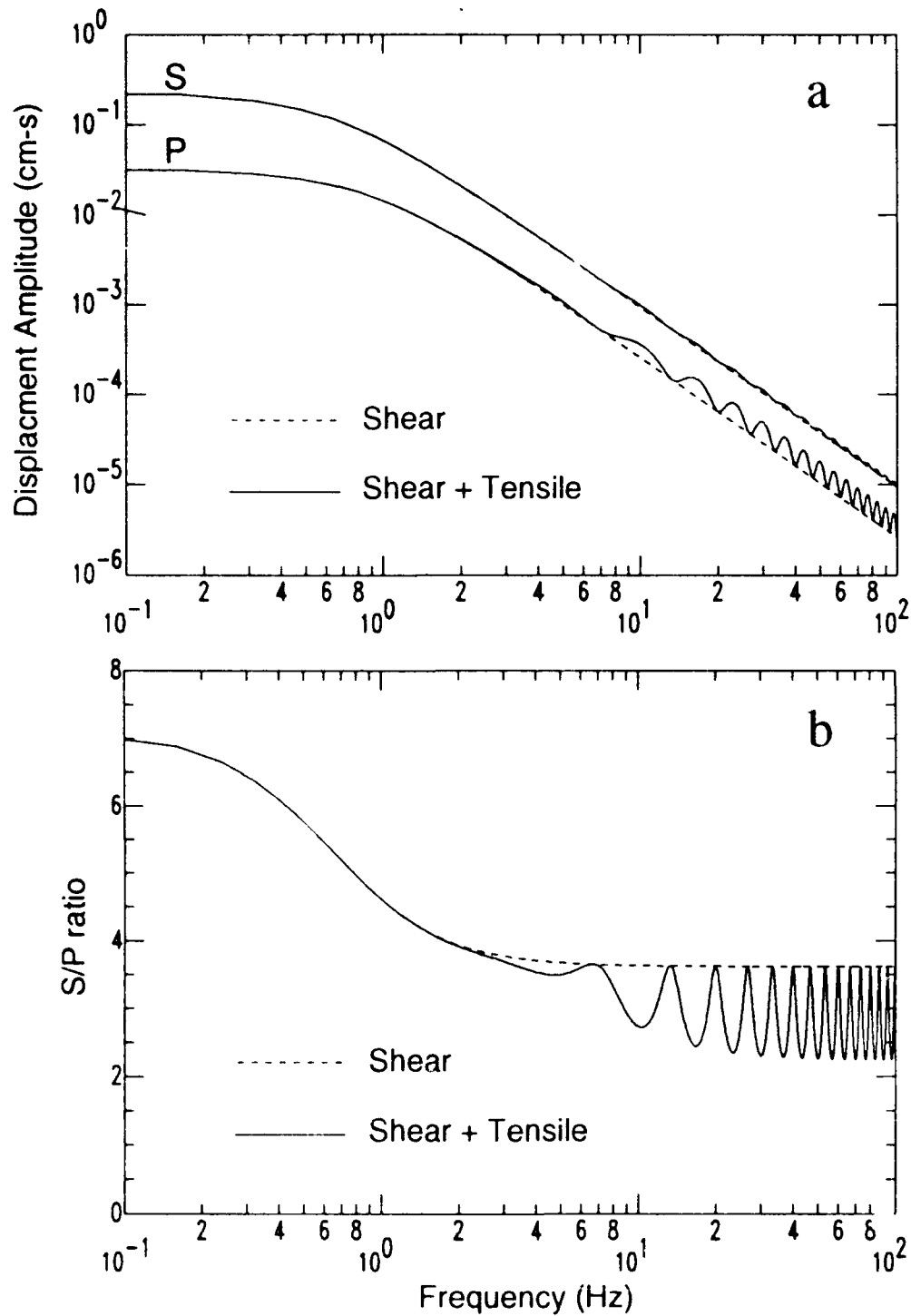
Fig. 18. (a) Composite spectra compared with pure shear crack. Composite spectra is composed of a 2 km radius shear crack with a maximum of 10 cm of slip plus 10 inchoherently adding opening and closing tensile cracks (200 m radius, maximum opening 2 cm). (b) S/P ratio of spectra in (a).

The first composite event consists of 1 shear crack and 10 opening and closing subevents. The tensile subevents have a radius of 200 m and a maximum opening of 2 cm with an opening closing time, τ, of 0.15 s ($\tau = 2a/0.8\beta$). Assuming the tensile sub events do not overlap, they cover 10 per cent of the area of the shear crack. The total energy radiated by the tensile subevents is also about 10 percent of that radiated by the shear crack. The composite model spectra are shown in Figure 19a compared with the shear crack alone. The effect of the tensile subevents is visible at frequencies above 2 Hz. Figure 19b shows the S to P ratio for the composite event and the shear crack alone. The tensile subevents decrease the S/P ratio at frequencies above 2 Hz although the average effect on the S/P ratio is similar to that of a shear crack alone with a P to S corner frequency ratio of 1.73 (see Figure 18b).

A second composite event was constructed using smaller radius subevents. The second composite model consists of the same 2 km radius shear crack with 10 cm maximum slip plus 100 opening and closing tensile subevents which add incoherently. The tensile subevents have a radius of 20m with a maximum opening of 2 cm and a τ of 0.015 s. The tensile sub events cover just one per cent of the area of the shear crack. Again the total radiated tensile energy is about ten per cent that of the shear crack. The composite spectra are shown in Figure 20a as well as that of the shear crack alone for comparison. The effect of these smaller radius tensile subevents becomes apparent for frequencies above 20 Hz. Figure 20b shows the S to P ratio for the composite event and the shear crack alone. The tensile subevents substantially decrease the S/P ratio above 20 Hz and in the 80 - 100 Hz range the ratio is less than two. The large peak in the S/P ratio at about 70 Hz is due to the first null in the $(2 - 2\cos\omega\tau)^{1/2}$ term in the opening and closing tensile subevents.

A final composite model using 1000 tensile subevents with radii of 20 m and maximum openings of 2 cm was constructed. These tensile subevents cover just 10 percent of the area of the shear crack but radiate approximately equal energy. The final composite model spectra is shown in Figure 21a. The effect of the tensile subevents becomes apparent above 10 Hz. Figure 21b shows the S/P ratio for the composite event and the shear crack alone. For this model the S/P ratio drops below two above about 30 Hz and approaches the expected ratio of the tensile cracks alone, a value of about 1.2, at 100 Hz.

Conclusions

A model for the displacement amplitude spectra of a circular crack failing in tension was presented. Although the spectra of the tensile crack model is similar to that expected for circular shear cracks, the radiation pattern differences lead to predictions of much lower average S/P ratios for tensile as opposed to shear cracks. These low S/P ratios may be an identifying characteristic of tensile or tensile equivalent seismic sources.

We construct some composite events of shear and tensile cracks that may be representative of slip on a non-planar fault. We show that a tensile crack must have about 44 per cent of the maximum slip on a shear crack to have equal average
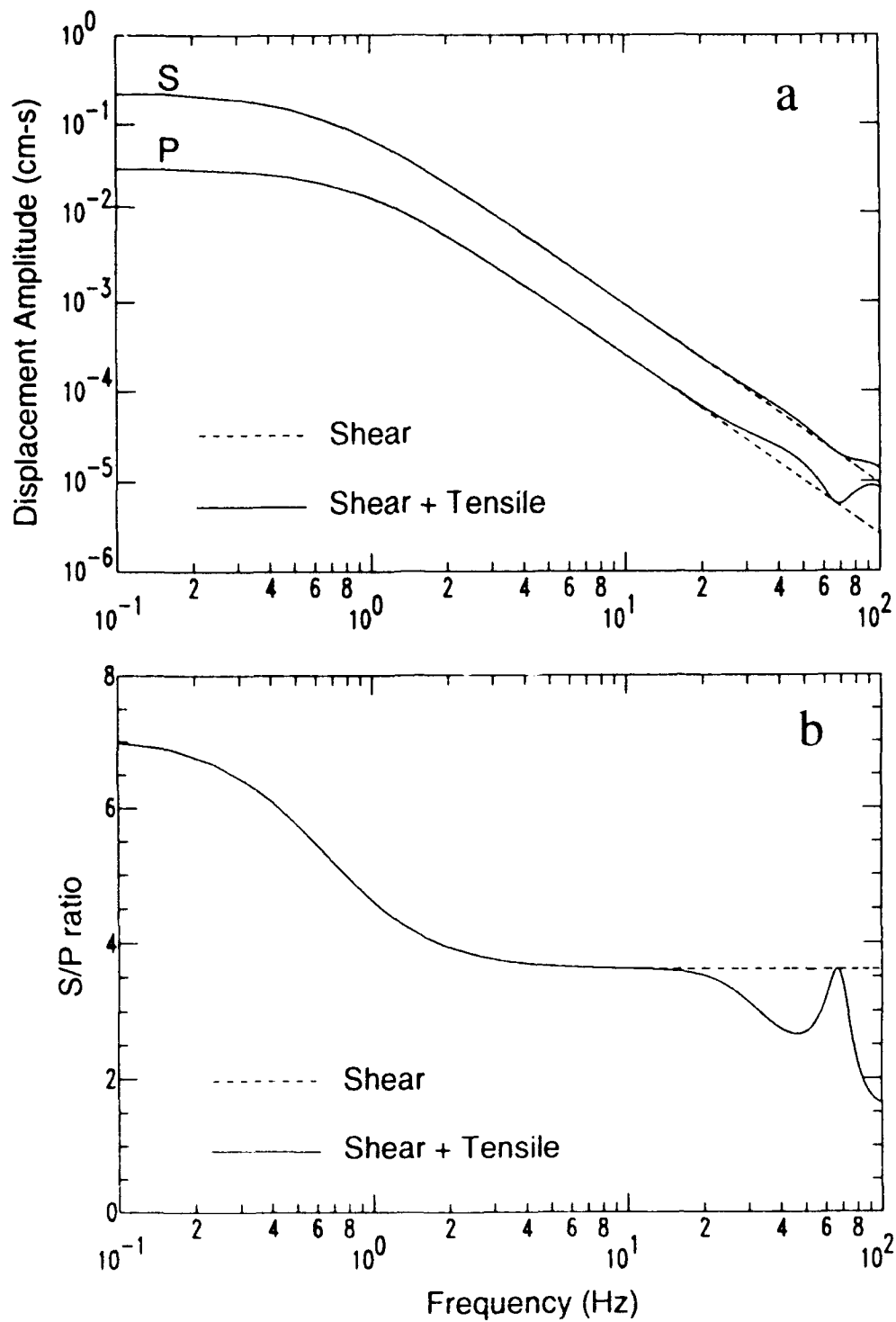
Fig. 19. (a) Composite spectra compared with pure shear crack spectra.
Composite is composed of 1 shear crack (radius 2 km, maximum slip
10 cm) and 100 incoherently adding opening and closing tensile cracks
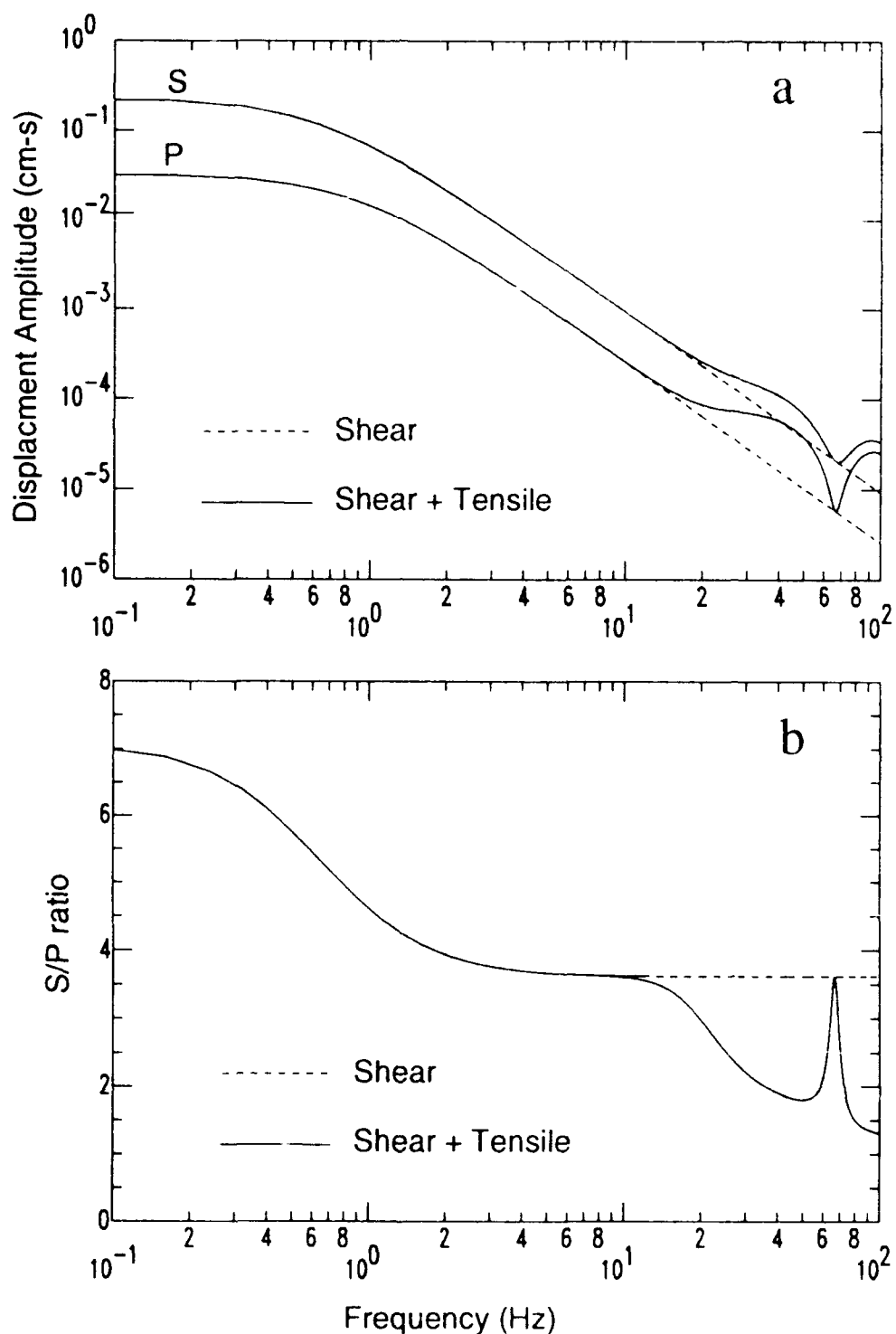(20 m radius, 2 cm maximum opening). (b) S/P ratios of above spectra.

Fig. 20. (a) Composite spectra compared with pure shear crack. Composite spectra is composed of one shear crack (2 km radius, maximum slip 10 cm) and 1000 incoherently adding opening and closing tensile cracks (20 m radius, 2 cm maximum opening). (b) S/P ratios of above spectra.

61

amplitude P spectra. If the tensile subevents have radii within an order of magnitude of the shear event the composite spectra may have the appearance of a pure shear crack with a high P/S corner frequency ratio. If the subevents have smaller radii, the composite spectra show much lower S/P ratios at high frequencies than expected for shear cracks alone. These anomalously low S/P ratios may occur when the tensile subevents radiate less than 10 per cent of the energy of the shear crack and cover just a fraction of the fault area.

Appendix

The spectral shape assumed in equation (3.1) is one of a class of spectral shapes of the form:

$$|\Omega(\omega)| = \frac{\Omega_o}{(1 + (\omega/\omega_c)^2)^{\psi/2}} \tag{3.A1}$$

which can be described by a low frequency level, Ω_o, a corner frequency, ω_c and a high frequency falloff slope, ψ. P or S waves which have displacement amplitude spectra given by equation (3.A1) contain an amount of energy given by:

$$W = 2\rho R^2 c \int_{-\infty}^{\infty} |\Omega(\omega)|^2 d\omega = \chi \sqrt{\pi} \rho R^2 c \Omega_o^2 \omega_c^3 \tag{3.A2}$$

where ρ is the medium density, R the distance from the source, c the P or S wave velocity and χ is a constant given by:

$$\chi = \frac{\Gamma(\psi - 1.5)}{\Gamma(\psi)} \tag{3.A3}$$

where Γ denotes the "gamma function". Note that equation (3.A3) is defined only for $\psi > 1.5$. If $\psi = 2.0$ then $\chi = \sqrt{\pi}$ and we get the same results as the main body of the paper. If, for example, $\psi = 2.5$ ($\chi = 4/3\sqrt{\pi}$) or $\psi = 3.0$ ($\chi = \sqrt{\pi}/4$) then our corner frequency equations in the main body of the paper would change but the low frequency values are unaffected. Making use of equations (3.A2) and (3.A3) we can rewrite equations (3.17) and (3.25) for the case of model spectra of the form (3.A1). Equation (3.17) becomes:

$$\omega_c^S = \left[\frac{\pi^{1/2}}{\chi} \frac{1620 f}{47\sqrt{3} g^3 + 216} \right]^{\frac{1}{3}} \frac{\beta}{a} \tag{3.A4}$$

and equation (3.25) becomes:

$$\omega_c^{S'} = \left[\frac{\pi^{3/2}}{\chi} \frac{2835\, f'}{8\sqrt{3}\, g'^3 + 324} \right]^{\frac{1}{3}} \frac{\beta}{a'}. \tag{3.A5}$$

It is apparent from the above equations that a high frequency falloff slope of three ($\psi = 3$) results in corner frequencies that are $4^{1/3} \approx 1.59$ times larger than when the falloff slope is assumed to be two.

References

Aki, K. and P. G. Richards, *Quantitative Seismology*, W. H. Freeman and Co., San Francisco, 1980.

Andrews, D. J. Mechanics of fault junctions, *J. Geophys. Res.* 94, 9389-9397, 1989.

Blandford, R. R., A source theory for complex earthquakes, *Bull. Seism. Soc. Am.* 65, 1385-1405, 1975.

Brune, J. N., Tectonic stress and the spectra of seismic shear waves from earthquakes, *J. Geophys. Res.*, 75, 4997-5009, 1970.

Brune, J. N., Correction, *J. Geophys. Res.*, 76, 5002, 1971.

Castro, R. R., J. G. Anderson and J. N. Brune, P/S spectral ratios from the Guerrero accelerograph array, *submitted to Bull. Seism. Soc. Am.*, 1991.

Eshelby, J. D., The determination of the elastic field of an ellipsoidal inclusion and related problems, *Proc. Roy. Soc. London, A 241*, 376-396, 1957.

Haskell, N. A., Total energy and energy spectral density of elastic wave radiation from propagating faults, *Bull. Seism. Soc. Am.* 54, 1811-1841, 1964.

Lomnitz-Adler, J., A microscopic model for steady-state friction, *J. Geophys. Res., in press*, 1991.

Madariaga, R., Dynamics of an expanding circular fault, *Bull. Seism. Soc. Am.* 66, 639-667, 1976.

Melosh, H. J., Acoustic fluidization: a new geologic process?, *J. Geophys. Res.* 84, 7513-7520, 1979.

Molnar, P., B. E. Tucker, and J. N. Brune, Corner frequencies of P and S waves and models of earthquake sources, *Bull. Seism. Soc. Am.* 63, 2091-2104, 1973.

Ode.., J.T., and J.A.C. Martins, Models and computational methods for dynamic friction phenomena, *Comp. Meth. Appl. Mech. Eng.*, 52, 527-634, 1985.

Patton, H.J. and G.. Zandt, Seismic moment tensors for western U.S. earthquakes and implications for the tectonic stress field, Report UCRL-JC-105880, 36 pp., 1990.

Randall, M. J., The spectral theory of seismic sources, *Bull. Seism. Soc. Am.* 63, 1133-1144, 1973.

Sack, R. A., Extension of Griffith's theory of rupture to three dimensions, *Proc. Phys. Soc.*, 58, 729-736, 1946.

Sato, T. and T. Hirasawa, Body wave spectra from propagating shear cracks, *J. Phys. Earth. 21*, 415-431, 1973.

Scholtz, C.H., and C.A. Aviles, The fractal geometry of faults and faulting, in *Earthquake Source Mechanics*, American Geophysical Union Monograph, 37, 147-155,

1986.

Segall, P. and D.D. Pollard, Mechanics of discontinuous faults, *J. Geophys. Res.*, *85*, 4337-4350, 1980.

Sneddon, I. N., Fourier Transforms, McGraw Hill, New York, 542 pp., 1951.

Tolstoi, D. M., Significance of the normal degree of freedom and natural normal vibrations in contact friction, *Wear*, *10*, 199-213, 1967.

Vernon, F., J.N. Brune and J. Fletcher, Source parameters of small earthquakes in the Anza array estimated from 300 m borehole recordingsm *Seism. Res. Lett.*, *62*, 16, 1991.

SECTION D

IMPLICATIONS OF EARTHQUAKE FOCAL MECHANISM DATA FOR THE ACTIVE TECTONICS OF THE SOUTH CASPIAN BASIN AND SURROUNDING REGIONS

Keith Priestley[1]
Department of Geological Sciences
and Seismological Laboratory
University of Nevada, Reno
Reno, Nevada 89557

Calum Baker, James Jackson
Department of Earth Sciences
University of Cambridge
Cambridge, CB3 0EZ, United Kingdom

SUMMARY

The south Caspian Basin is a relatively aseismic block within the Alpine-Himalayan Belt, but is surrounded by zones of high seismicity. We used the focal mechanisms of 16 earthquakes whose source parameters we determined from inversion of body waves, and the mechanisms of 15 other earthquakes to determine the style of faulting in the seismic belts that surround the south Caspian Basin. Earthquakes beneath the Talesh Mountains of NW Iran and immediately off-shore in the SW Caspian Sea have shallow thrust mechanisms, showing that the continental crust of NW Iran is overthrusting the "oceanic-like" crust of the south Caspian Basin. Earthquakes south of the Caspian Sea in northern Iran show a mixture of focal mechanisms. Both high angle reverse faulting and left-lateral strike slip faulting are observed in the high Alborz Mountains. Farthers south, on the edge of the central Iran plateau, oblique left-lateral reverse mechanisms are observed. It seems that the NE direction of shortening between central Iran and the south Caspian Basin is partitioned into pure left-lateral strike-slip and thrusting in the WNW trending high Alborz, but is accommodated by oblique faulting in lower elevations. Earthquakes in the Kopet Dag Mountains east of the Caspian Sea also show a mixture of high angle reverse and strike-slip faulting mechanisms and thus may be another example of the partitioning of oblique slip into strike-slip and thrust motion. Normal faulting mechanisms at centroid depths of 35 to 50 km dominate in the belt of seismicity which extends across the central Caspian Sea. The significance of the normal faulting earthquakes is enigmatic. It is improbable that these events represent the motion between the southern Caspian Basin and Eurasia for they imply a sense of motion which is incompatible with the observed topography and folding in the sediments. Two shallow earthquakes at about 12 km depth in this belt, one a small event and the other a large second sub-event of a multiple earthquake, have

[1] now at: Department of Earth Sciences, University of Cambridge, Cambridge, CB30EZ, United Kingdom

thrusting mechanisms suggesting that shortening occurs as the continental crust of the northern Caspian is thrust over the "oceanic-like" crust of the southern Caspian Basin. Shortening is also suggested by the orientations of folds in the sedimentary cover south of the central Caspian Sea seismic belt. We suggest that this shortening does indeed represent a NNE motion of the Caspian Sea relative to Eurasia, but that the motion is slow and has not produced many earthquakes. The deep, normal faulting may be related to bending or down-dip extension of the incipient subducted slab. If the motion of the Caspian Sea relative to Eurasia is indeed slow, then the motion in the Alborz between central Iran and the south Caspian Basin will be almost the same as that between Iran and Eurasia, as has previously been assumed.

The combined effect of the overthrusting of the south Caspian Basin by the Talesh-Alborz mountains in the south, and by the continental crust of the northern Caspian Sea in the north will lead to the eventual destruction of the south Caspian Basin and the possible formation of an intermediate depth, dipping seismic zone within the continental interior, similar to that presently observed in the Hindu Kush.

INTRODUCTION

This paper is concerned with the active faulting in and around the south Caspian Basin, which is a relatively aseismic block within the Alpine-Himalayan Belt but is surrounded by highly active seismic zones.

There were two motivations for this study. The first was to discover the nature of the deformation in the belt of seismicity extending across the central Caspian Sea from the Caucasus in the west to the Kopet Dag in the east. Before 1986, no earthquakes of $m_b \leq 5.5$ had occurred in this belt since the installation of the World Wide Standard Seismic Network (WWSSN) in the early 1960's and thus no reliable fault plane solutions were available. As a result, discussions of the motion of the south Caspian Basin with respect to Eurasia have largely been speculative. Nowroozi (1972) believed that the south Caspian is moving northwestward relative to Eurasia. Jackson & McKenzie (1984) pointed out that the thrust faulting earthquakes that occur throughout the Caucasus, Alborz, and Kopet Dag Mountains all have similar slip vectors directed NE, suggesting that the south Caspian is moving northeastward relative to Eurasia, although less rapidly than Iran. We have studied the mechanisms of several earthquakes in the Trans-Caspian seismic belt to better define the motion of the south Caspian Basin.

A second motivation for the study was to better understand the tectonic setting of the 6 June 1990 earthquake in the Talesh Mountains of the southwest Caspian. This was by far the largest earthquake (M_w 7.2) to occur in the region this century, and it had a focal mechanism quite unlike that of neighboring events. A detailed field and seismological report on this earthquake is published elsewhere (Berberian et al, 1991).

The principale new data we present new observations of earthquake focal mechanisms and depths determined from P-wave first motion and P- and SH-waveform data. These are much better constrained than the anisms and in earlier studies (eg. Jackson and McKenzie, 1984), which were based on P wave first motions alone, and extend the period of observation to 1990.

GEOLOGICAL AND GEOPHYSICAL SETTING

The seismicity of the Middle East is dispersed over bands 100 - 300 km wide, which surround regions such as the south Caspian Basin and central Ira within which the seismicity is relatively low (Fig. 21 and Jackson & Mckenzien 1984). The western and southern margins of the south Caspian Basin are bounded by an active arcuate fold and thrust belt in the Talesh and Alborz Mountains (Fig. 22a). To the east of the south Caspian Sea lies the west Turkmenian lowlands, which are structurally part of the south Caspian Basin. Farther to the east lie the seismically active Kopet Dag Mountains. The deeper water ($\approx$1000m) of the south Caspian Basin is separated from the shallower water ($\approx$200m) of the central and north Caspian Sea by the Apshceron - Balkhan sill, a shallow, seismically active zone extending from the Caucasus Mountains in the west to the Kopet Dag Mountains in the east (Fig. 21, 22b).

Deep seismic sounding (DSS) data from the south Caspian Basin reveal a crust consisting of a thick (15-20 km) low velocity (V_p 3.5 to 4.0 kms^{-1}) sedimentary section resting on a high velocity ($V_p \geq 6.7\ kms^{-1}$) layer (Galperin et al, 1962; Malovitsky, 1968; Neprochnov, 1968; Rezanov & Chamo, 1969; Malovitsky et al, 1970; Fedynsky et al, 1972) (Fig. 22a). DSS data to the east of the south Caspian Basin indicate the existence of a V_p 6.0 kms^{-1} layer, thought to represent continental basement, which pinches out towards the southwest and disappears beneath the Turkmenian lowlands. The existence of a 6.0 kms^{-1} layer is also apparent in DSS data from north of the Apshceron-Balkhan sill and in the Talesh and Alborz Mountains in northern Iran (Berberian, 1983), to the south of the Caspian Sea. The high velocity crustal layer of the south Caspian Basin has been assumed by many to be "oceanic-like crust" and this view is supported by observations of L_g blockage and efficient S_n propagation for paths crossing the south Caspian Basin (Kadinsky - Cade, et al, 1981). Seismic profiling shows that the sedimentary cover of the south Caspian Basin has undergone considerable deformation (Zonenshain & Le Pichon, 1986).

In the western part of the basin the fold axes trend NNW-SSE to N-S (Fig. 22a). Fold axes in the north and south parts of the basin trend NW-SE roughly parallel with the Apshceron-Balkhan Sill and the north Iranian coast, respectively (Fig. 22a).

The tectonic history of the south Caspian Basin has been reviewed by Berberian & King (1981), Berberian (1983), and Zonenshain & Le Pichon (1986). The age of the "oceanic" basement is uncertain. Paleoreconstruction of the Iranian region (Berberian and King, 1981) indicates that if the high velocity layer is oceanic it could be a relic of an ocean that closed in either the Triassic or the Cretaceous, or else a marginal sea that developed behind an island arc. The region has been dominated by compression during the Pliocene-Pleistocene. Some Soviet earth scientists (e.g. Muratov, 1972; Yanshin et al, 1980; Shlezinger, 1981) propose that the south Caspian Basin is young and was formed by the eclogitization and subsidence of granitic continental crust during the mid- to late Cenozoic. Others, (e.g. Amursski et al, 1968; Sorokhtin, 1979; Vardapetyan, 1981) consider the south Caspian Basin to be pre-Hercynian in age and a remnant of the Early Mesozoic Tethys sea floor. Evidence cited in support of the latter hypothesis includes the great thickness of sediment and low observed heat flow. Shikalibeily & Grigoriants (1980) suggest that the south Caspian Basin is Jurassic and is overlain by Cretaceous volcanic rocks. Adamia

et al (1977) and Letouzey et al (1977) consider the south Caspian Basin as a remnant back-arc basinresulting from spreading behind a Late Cretaceous - Paleogene volcanic arc. Despite the uncertainty in the age, most authors agree that the high velocity "oceanic-like" basement extends eastward beneath the western Turkmenian lowlands and to the western coastal region of the Azerbaijan-Caspian coast (Amursski et al, 1968). A more detailed discussion of the tectonic history of the region surrounding the south Caspian Basin can be found in Berberian (1983) and Zonenshain and Le Pichon (1986).

DETERMINATION OF EARTHQUAKE FOCAL PARAMETERS

We have used P-wave first motion polarities and P- and SH-waveforms to constrain the source parameters of moderate size earthquakes occurring in the region surrounding the south Caspian Basin. The earthquakes whose mechanisms we have studied plus those whose mechanisms we have taken from Jackson & McKenzie (1984), the Harvard centroid moment tensor (CMT) catalogue, or Gao & Wallace (1991), are listed in Table 1.

The P-wave first motions shown in Figure 23 are from WWSSN seismograms read by the authors. In almost all cases these were read from the long-period vertical component. In a few cases where the long-period vertical onset was too small or obscured by noise, we read the first motion from the short-period vertical component providing the onset was clear, impulsive, and recognizable as the instrument impulse response. In all cases, we used a P-wave velocity at the source of 6.8 kms^{-1} to plot the station positions on the focal sphere.

The P- and SH-waveform data are from the WWSSN and Global Digital Seismic Network (GDSN) stations in the distance range 30° - 95°. Our analysis followed the approach described by McCaffrey & Nabelek (1987) and subsequently used in a number of other studies (e.g., Molnar & Lyon-Caen 1989; Taymaz et al., 1990). Source parameters were determined using McCaffrey & Abers' (1988) version of Nabelek's (1984) waveform inversion procedure. This routine minimizes in a least squares sense, the misfit between the observed shape and amplitude of the long-period P- and SH-waveforms and synthetic waveforms. The synthetic seismograms are computed for a point source embedded in a simplified Earth structure by combining the direct arrival (either P or S) with the near source reflections (pP and sP, or sS) and near source multiples. The earthquakes were assumed to be either embedded in a velocity structure which was a simplified version of a published crustal velocity model for the same region, or embedded in a crustal velocity structure of a tectonically analogous region if no published velocity model exist in the region of the earthquake. Seismographs are assumed to be located on a homogeneous half space. When available, we have taken the Harvard CMT solution reported in the Preliminary Determination of Epicenters (PDE) as the starting point in the inversion; whereunavailable, we have used the first motion fault plane solution of Jackson & McKenzie (1984). The time durations of the seismogram inversion windows were chosen to be long enough to include the near source reflected phases pP, sP, or sS. We examined the waveforms where we thought the PcP or ScS arrival might be within the inversion window. If we thought these phases might be of significant amplitude, we truncated our inversion window.

Synthetic waveform amplitudes are corrected for geometrical spreading, and anelastic attenuation is accounted for by applying a Futterman (1962) Q operator with $t^*_p = 1$ sec and $t^*_s = 4$ sec. Uncertainties in t^* mainly affect estimates of source duration and seismic moment, but have smaller effects on source orientation or centroid depth (Fredrich et al, 1988). To avoid complications introduced by the upper mantle triplication or core phase interference we restricted the body waveform inversion (with one exception discussed in the Appendix) to P-waves in the $30°$ to $90°$ distance range and S-waves in the $35°$ to $84°$ distance range. In the inversion process, SH seismograms were given only 50% of the weight of the P-wave seismograms, and all seismograms were azimuthally weighted; that is, seismograms from stations clustered together in azimuth were given lower weight than seismograms from isolated stations. We assumed that all slip occurs at the same point in space, the centroid location, but is distributed in time, the source time function. This is usually a good approximation for events less than about M_s 6.5. However, in one case complexities observed in the seismograms suggest the existence of a second source. The source time function is described by a series of overlapping isosceles triangles (Nabelek, 1984). We initially selected the number and duration of the isosceles triangles using the event magnitude as a guide. We then eliminated late occurring, small amplitude elements of the source time function if we felt these were the result of noise. The inversion routine minimizes the misfit between the observed and synthetic waveforms by varying the strike, dip, slip, centroid depth, seismic moment, and source time function.

The "best-fitting" set of source parameters is found by the inversion routine. However, the statistical description of the inversion misfit underestimates the true uncertainties. Similar to McCaffrey & Nabelek (1987), once we had obtained the minimum misfit solution, we performed a series of tests to assess realistic uncertainties and examine tradeoffs between the various factors. Our test procedure was to fix the source parameter being examined at a series of values that bracket the "best-fitting" value, then reinvert the waveform data to examine what effect variations in the fixed parameters had on the free parameters. In summary, we found that reasonable variations in crustal velocity structure do not result in significant changes in strike, dip and rake, but can affect centroid depth, moment, and the source time function. Our tests showed that the strike, dip, rake, and centroid depth are relatively independent of each other: that is, when one parameter was held fixed at a value within a few degrees or kilometers of its minimum misfit value and the waveforms reinverted, the resulting values of the free parameters were close to their minimum misfit values.

AN EXAMPLE OF WAVEFORM ANALYSIS: THE EARTHQUAKE OF 4 NOVEMBER 1978

The 4 November 1978 (1978.11.04) Siahbil earthquake belongs to a group of events occurring in northwest Iran which we have studied, and whose mechanisms are consistent with overthrusting of the south Caspian Basin by the Azerbaijan-Talesh block of northwest Iran. This event has been examined in several previous studies and provides a good example of the waveform analysis conducted in this study. P-wave first motion polarities (Fig. 23) constrain a $347°$ striking, high angle ($79°$ ENE) plane. This does not conform to any

mapped faults in the area (Berberian, 1983) and is taken as the auxiliary plane. The shallow dipping fault plane is poorly constrained by the first motion data. Berberian (1983) studied P- waveforms of this event by forward modelling and concluded that the earthquake occurred on a 168° striking fault dipping 9° WSW at a depth of 20 ± 4 km. One plane of the best fitting double couple to the Harvard CMT solution strikes 177°, dips 9° WSW, has a rake of 87°, and has a centroid depth of 15 km. Figure 24 shows the match between the observed seismograms and synthetic P and SH seismograms computed for the minimum misfit solution. We used the Harvard CMT solution as the starting point in the inversion procedure. The velocity structure used in obtaining these results consisted of a 12 km thick layer (V_p 5.60 kms^{-1}, V_s 3.24 kms^{-1}, ρ 2600 kgm^{-3}) overlying a half-space (V_p 6.80 kms^{-1}, V_s 3.93 kms^{-1}, ρ 2900 kgm^{-3}). The inversion routine requires that the source be located in the half-space. The source parameters from our inversion (given in the title of Figure 24 and in Table 2) are not significantly different from previously determined solutions for this event. The inversion procedure is nonlinear and the result may be dependent on the starting parameters. To verify that we had not found a local minimum, we significantly displaced the starting solution from the Harvard solution and reinverted the waveform data to verify that we still obtained a similar solution.

Having determined a minimum misfit solution, we performed a series of tests to estimate the effect on the source parameters produced by variations in the source velocity structure and to place bounds on the source parameters.

Source Region Velocity Structure: Since the crustal velocity structure in the south Caspian region is poorly known, our approach was to use a simplified version of a published crustal velocity models in the area of the earthquake if they exist, or the crustal velocity models of an analogous tectonic region if no crustal velocity model in the vicinity of the earthquake has previously been determined. We performed a number of tests for the 1978.11.04 earthquake to see how reasonable variations in source velocity structure affect estimates of the source parameters and just how different the source velocity structure could be before it significantly affected the inversion results. Figure 25 shows the results of our tests. The velocity models tested are given in the figure caption.

The McCaffrey-Abers inversion routine allows for only a simplified source structure. The first row in Figure 25 shows the minimum misfit solution from Figure 24. In our first test (Row B), we altered the velocity structure in such a way so as to give the same delay time between the direct phase and the surface reflection (the controlling factor in determining the depth), as the delay determined for the crustal velocity structure we thought most realistic (used in computing Row A). We then reinverted the whole data set. The synthetic waveforms for the minimum misfit solution for this velocity structure are indistinguishable from those in Row A. The focal parameters strike, dip, rake, and centroid depth are not significantly different from the results in Row A and only the seismic moment is different. We next made changes in the velocity structure which still would represent reasonable crustal velocity structures (Row C - D) without attempting to preserve the delay time above the source. This again produced negligible changes in the synthetic waveforms from those shown in Row A. Row E and F show minimum misfit synthetics for more radical (and probably unrealistic) changes in the crustal velocity structures. These do

show more significant changes but even in these cases, the source orientations have hardly changed from those in Row A. We conclude from these tests that reasonable variations in crustal velocity structure affect strike, dip, and rake less than other factors. Varying the source velocity structure did have a significant effect on centroid depth and seismic moment. These arise from variations in delay times between the direct and surface - reflected phases, and from variations in the reflection coefficients.

Assessment of Source Parameter Uncertainties: Thorough discussions of the assignment of uncertainties are given in McCaffrey & Nabelek (1987) and Molnar & Lyon-Caen (1989). For each event we studied, we have made extensive tests to determine uncertainty bounds on thecentroid depth, and the strike, dip, and rake of the fault plane. These uncertainties are listed in Table 2.

Figure 26 summarizes only the tests we have made to place bounds on the strike, dip, rake and centroid depth of the 1978.11.04 event. The first row compares the observed seismograms and those computed for the minimum misfit solution. The following four rows compare the observed seismograms with those computed when one source parameter is held fixed at the smallest displacement from the minimum misfit value which resulted in a significant degradation of the synthetic fit. In making the full range of tests, we held one parameter (e.g. centroid depth) fixed at a value different from the minimum misfit value, and inverted for the remaining source parameters. We then successively increased the difference between the fixed parameter we were testing and its minimum misfit value until a significant difference was apparent between the observed seismograms and the synthetics computed for the particular combination of source parameters. Based on a range of tests of these parameters which are summarized in Figure 26, we estimate that for the 1978.11.04 earthquake the bounds on the centroid depth are ± 5 km, strike ±15°, dip ±4°, and rake ±20°. For low-angle faulting events such as the 1978.11.04 earthquake the rake is not tightly constrained. The bounds on focal parameters shown in Table 2 are of similar magnitude to those noted in comparable studies in other regions (e.g. Molnar & Lyon-Caen, 1989; Taymaz et al., 1990).

THE EARTHQUAKE OF 6 MARCH 1986

We now discuss the earthquake of 1986.03.06 in some detail for two reasons: it was the first moderately large earthquake to have occurred in the central Caspian seismic zone since the installation of the WWSSN, and it was the only event we studied whose seismograms suggested to us the possibility of a complex multiple rupture involving sub-events of different mechanisms. The S-wave spectrum from seismograms recorded at Askhabad (Golensky et al., 1989) and the coda spectrum (Rautian - personal communication) are complex, showing a constant low frequency level, a low frequency corner at 0.08 Hz above which there is a high frequency decay of ω^{-1} to a second high frequency corner at 1.0 Hz above which the spectrum decays as ω^{-2}. Smith et al (1991) attribute such a spectral shape to source complexity with the low frequency corner corresponding to the overall source dimension and the high frequency corner related in some fashion to the size of the subevents. The P-wave first motion polarities (Fig. 23) tightly constrain a near vertical nodal plane. striking 300 . Our single source minimum misfit inversion solution is shown

in Figure 27a. This solution is very similar to the best fitting double couple solution from theHarvard CMT catalogue. The agreement between the observed and synthetic seismograms is good at most stations. However, waveforms of stations lying on the focal sphere near the P-wave nodal plane (e.g. SHL, KOD, PTO, STU) show a weak initial P-wave arrival in keeping with the nodal position, but also show a large second pulse, shaped like an inverted "W", that follows the first motion by about 20 seconds. The single source shown in Figure 27a cannot reproduce the late pulse observed at these stations since the direct P and pP are both nodal, and hence of small amplitude, and sP leaves the focal sphere close to the node in the S radiation pattern.

With our poor knowledge of the undoubtedly complex crustal velocity structure in the vicinity of the Apshceron-Balkhan sill, it is impossible to adequately assess the contribution to seismogram complexity resulting from three-dimensional velocity structure. However, what appears to be missing from the P-waveforms of the near nodal seismograms is an inverted "W" P-wave arrival reminiscent of shallow depth, reverse faulting earthquakes (e.g., Jackson & Fitch, 1981). This suggests to us that the 6 March 1986 earthquake may have been a multiple event. Source complexity is also suggested by the shape of the source spectrum at regional stations in the U.S.S.R. (Golensky et al., 1989; Ratuian - personal communication). We therefore reinverted the P- and SH-waveforms, allowing for the existence of a second, delayed, reverse-faulting event. The starting source model for the second waveform inversion consisted of an initial event with the source mechanism shown in Figure 27a, followed 10 seconds later by a second reverse faulting event. The starting source orientation for the second reverse faulting event was guided by our interpretation of the observed waveforms. The reversed mechanism must be constrained to produce the observed P-waveforms at nodal stations such as SHL, KOD, PTO and STU, but not disturb the observed P-waveforms at African stations such as SLR and WIN, nor disturb the nodal character of the SH-waveforms at these stations. A 45° reverse faulting event with a strike near 300°, similar to the strike of the initial event, conforms to these requirements. We reinverted the waveform data, first constraining the mechanisms of the first event and solving for the fault plane parameters, centroid depth, source time function, and origin time offset of the second event. To produce the final solution shown in Figure 27b, we inverted the waveform data with all parameters of both events free. Synthetic waveforms for this double event solution fit observed waveforms at all azimuths equally well. The nodal character of SH-waves observed at African stations is preserved and provides the main constraints on the strike of the second event.

To assure ourselves that the initial conditions we assumed in constructing the second source were not overly restrictive and biasing our result, we reinverted the waveform data with both events having a starting solution similar to the normal faulting mechanism shown in Figure 27a, but the second source delayed by 10 seconds. The mechanism for the first event changed little, and the solution of the second event changed from having a normal to reverse mechanism. We reinverted the data with other startingdepths for the second event and again the final result was very near the solution shown in Figure 27b.

Figure 28 compares results for the single and double source solution and individual waveforms for the elements of the double source. The upper row compares the observed

seismograms with those computed for the single source, minimum misfit solution. Stations SHL, KOD, PTO, and STU lie on the focal sphere near the P-wave node for the single source; station WIN lies near an SH node. The single source synthetics poorly match the observed seismograms at the four P-wave nodal stations, as discussed above. The P-wave seismogram recorded at SLR is reasonably well fit by the synthetic, with the exception of the large back swing. The SH nodal character observed in the WIN seismogram is preserved and the SH waveform observed at KOD is reasonably well fit with the exception of the large back swing which is larger in the synthetic than in the observed seismogram.

The second row of seismograms compares observed waveforms at the same stations with synthetic seismograms computed for the double source solution. The fit at WIN is similar to that for the single source, and fits for all other stations are significantly improved. Rows 3 and 4 show the contributions to the seismograms of the individual components of the double source. Both events have similar seismic moments. We performed a series of tests as described above, to estimate bounds on the centroid depth, strike, dip, and rake of the second event on the synthetic and compare these with the observed seismogram. From this comparison we estimate that the centroid depth, strike, dip, and rake of the second event are resolved to ± 4 km, $\pm 15°$, $\pm 5°$, and $\pm 8°$, respectively. Note that the seismic moment of this second source is almost as great as that of the first source. The combined seismic moment of the two subevents is 5.1×10^{17} Nm compared to 6.4×10^{17} Nm for the Harvard CMT solution.

It is difficult to assess whether the three dimensional velocity structure in the source region of the 1986.03.06 earthquake could produce the seismogram complexity that we attribute to a later sub-event. Two other moderate-sized earthquakes occurred in the central Caspian Sea on 16 and 17 September 1989 (1989.09.16, 1989.09.17) and our waveform inversion results for these two events are shown in Figures A13 and A14. P-waveforms of 1986.03.06, 1989.09.16, and 1989.09.17 at common stations are compared in Figure 29. As a result of the decline in performance of the WWSSN, data for the 1989 events are less complete than for 1986.03.06. The minimum misfit solution for both of the 1989 events have a normal faulting mechanism similar to the single source minimum misfit solution for 1986.03.06. However, WWSSN seismograms recorded to the northwest (e.g., PTO, VAL, NUR, WES), while not showing the same initial nodal character as seismograms recorded at similar azimuths for the 6 March 1986 event, do show some evidence for a similar later pulse in the P-wave train (Figs. A13, A14). Although the GDSN instrument response tends to blur details of the source time function and WWSSN data are scarce for the 1989 events, we inverted seismograms for the 1989.09.16 earthquake allowing the possibility of a second source. This resulted in a mechanism where the first source was similar to that in Figure A13, and a second source whose seismic moment was less than 10% that of the initial source. Three double earthquakes with similar time delays and mechanisms for the second events are somewhat suspect, and this may imply that the secondary arrivals result from crustal velocity structure complexities in the source region. However in a plane layered structure there is no direct P or SH arrival for the European and Indian stations showing the second pulse. It would therefore be necessary for the late pulse to be the result of bent raypaths, that is rays refracted after leaving the focal sphere

at different take off angles. On the other hand, there is another, smaller earthquake in this central Caspian belt (1987.12.19) with a Harvard CMT solution having almost the same reverse faulting mechanism as we postulate for the second sub-event of 1986.03.06. The earthquake of 1987.12.19 was too small for us to be able to confirm the Harvard CMT solution using long period P and SH waveforms. Although we prefer the double source explanation for the P-wave complexities discussed above for 1986.03.06, we are not able to rule out the possibility that complexities in the observed waveforms are the result of source region velocity structure.

TECTONICS OF THE SOUTH CASPIAN BASIN

The minimum misfit solutions for the other fourteen events we studied are presented in Appendix A. Their orientations are consistent to within a few degrees with the first motion polarity data. The few inconsistent first motion polarities are discussed in Appendix A. Figure 30a shows the fault plane solutions for these events (Table 2). Figure 30b shows fault plane solutions for other events which we have not analyzed: either first motion solutions of Jackson & McKenzie (1984) which occurred prior to establishment of the WWSSN (1957.07.02) or which produced insufficient long-period waveforms for us to analyze using the procedure outlined above, Harvard CMT solutions that were too small for us to study their P and SH waveforms, or the 20 June 1990 event (Gao & Wallace, 1991). With some exceptions, the patterns of focal mechanisms shown in Figures 30a and 30b are generally similar, giving us some confidence in the solutions we were unable to confirm by waveform inversion. In our discussion of the tectonics, we will rely primarily on the sixteen events we have studied (Fig. 30a) and the mechanism of the 20 June 1990 event (Gao & Wallace, 1991) (large symbol, Fig. 30b), but we will make cautious use of the firstmotion and CMT solutions of the smaller events.

Slip Vectors: Figure 31 shows the horizontal projection of the slip vectors for the events in Figure 30. Choosing the slip vector required us to identify one of the two nodal planes in each fault plane solution as the fault plane. Both the Buyin Zara earthquake (1962.09.01) (Appendix A) and the Rudbar-Tarom earthquake (1990.06.20) (Berberian et al, 1991) were accompanied by surface faulting, and the choice of the fault plane is straightforward (Ambraseys, 1963; Berberian et al, 1991). No surface faulting was recognized for the Karnaveh earthquake (1970.07.30). However, relative relocations of the aftershocks of this event defined an elongated pattern trending north-northeast (Jackson & Fitch, 1979), approximately parallel to the strike of one of the nodal planes (Figure A2) and also parallel to a nodal plane of a large aftershock with a similar mechanism to that of the main shock. The aftershock pattern suggests that the Karnaveh earthquake occurred on a northeast-trending fault with predominantly left-lateral strike-slip motion.

Other earthquakes such as the 1957.07.02, 1969.01.03, and 1983.07.22 events are almost pure thrust and hence the choice of the slip vector orientation is not very sensitive to the choice of the fault plane. For the 1969.01.03 and 1983.07.22 events we chose the planes dipping northeast to be consistent with the local topography; however, in both cases choosing the other plane would change the orientation of the slip vector by less than

10°. The other events studied all have one nodal plane that, if chosen as the fault plane, implies a slip vector similar to that of an adjacent earthquake whose slip vector ambiguity is resolved. This determined our choice of slip vectors for those events.

In the case of strike-slip events, this reasoning is dangerous. The 1990.06.20 event, which produced surface faulting, had a slip vector almost perpendicular to that of a nearby reverse faulting earthquake (1983.07.22) (See Berberian et al, 1991; Gao & Wallace, 1991). Three other strike-slip events occurred near thrust faulting earthquakes (1983.03.26, 1984.02.22, and 1990.01.20). For all of these we mark both possible slip vectors on Figure 31. The convention we have used in Figure 31 is to show the motion of the S or E side relative to the N or W side.

The inset in Figure 31 shows the orientation of the tension axes of the five normal faulting events in the central Caspian. All of these events have a shallow dipping, NNE striking tension axis.

Talesh Mountains: It is clear from the earthquake mechanisms we have studied that the Talesh and NW Alborz mountains overthrust thesouth Caspian Basin as suggested by Berberian (1983) and Jackson & McKenzie (1984). The slip vectors on the shore of the Talesh Mountains show the motion of the Caspian Sea westward beneath the Azerbaijan-Talesh block, which moves east relative to both Iran and the Arabian-Eurasia collision zone in eastern Turkey. This motion of the Azerbaijan-Talesh block may be accommodated inland by conjugate strike-slip faulting. The focal mechanism of the 1976.02.03 earthquake (Fig. 30b) is consistent with left lateral faulting on a NNE plane, parallel to a prominent NNE lineament followed by the Araxes River. Berberian & Arshadi (1976), Tchalenko (1977), and Ambraseys & Melville (1982) have studied faulting associated with two large northwest Iranian earthquakes which occurred in 1721 and 1786 (Fig. 22b). All agree that the southwest side of the fault was down-dropped, but disagree as to whether there was a significant right-lateral strike-slip component. Stream diversions are visible on aerial photographs (Tchalenko, 1977) suggesting right lateral offset but these have not been verified on the ground. The combination of left lateral faulting following the Araxes lineament along the Iran-USSR border, probable right lateral faulting extending southeast from the North Anatolian fault system, and low angle thrusting along the Talesh Mountains support Jackson & McKenzie's (1984) suggestion of the easterly expulsion of northwest Iran away from the collision zone in the Caucasus and the overthrusting of the south Caspian Basin. This motion is probably responsible for the N-S trending folds seen in the sedimentary cover offshore, east of the Talesh Mountains (Fig. 22a), and is presumably favored by the "oceanic-like" crust of the south Caspian Basin.

Alborz Mountains: The Rudbar-Tarom earthquake (1990.06.20) was by far the largest earthquake to occur in northern Iran this century. Berberian et al (1991) report at least 80 km of surface faulting along three discontinuous fault segments. These are arranged in a right-stepping en-echelon pattern, and are separated by gaps in the observed surface rupture. The three segments range in strike from 95° to 120° and have oblique, left-lateral and reverse motion on faults that are sub-vertical or have steep dips to the S or SSW. The

maximum surface displacements were 60 cm horizontal (left-lateral) and 95 cm vertical with the south side up. The moment tensor solution (Gao & Wallace, 1991) for the main shock suggests a complex rupture consisting of at least three sub-events, and had a significant non-double couple component. However, no change in fault geometry or slip direction during the main rupture could be resolved. The best fitting double couple (Table 3) has a strike 292°, dip 88°, and rake −9° which are consistent with the mapped faults. Berberian et al (1991) also reported mechanisms for two aftershocks. The largest (1990.06.21) had a focal mechanisminvolving thrusting (strike 26°, dip 69°, rake 87°) with a centroid depth of 17 km and a moment of $5.7X10^{17}$ Nm ($M_W 5.8$) similar to those in the adjacent Talesh Mountains. A second large aftershock (1990.06.24) had a mechanism similar to that of the main shock (strike 235°, dip 70°, rake −164°), a significantly shallower centroid depth (8 km), and a moment of $2.2X10^{17}$ Nm ($M_W 5.5$).

The 1990.06.20 earthquake occurred close to an earthquake that involved high-angle reverse faulting (1983.07.22). The slip vector of the 1990.06.20 main shock is in the wrong sense (left-lateral) to represent the relative motion between the Talesh-Azerbaijan block and Iran. We think it probable that the deformation in this part of the NW Alborz Mountains involves oblique, left-lateral shortening that is partitioned into pure left-lateral strike-slip (i.e. 1990.06.20) and pure thrusting (i.e. 1983.07.22) in almost the same region. Such an interpretation is consistent with the almost perpendicular slip vectors for the 1990.06.20 and 1983.07.22 earthquakes, and with those slip vectors being approximately parallel and perpendicular, respectively, to the regional topography and fold axes (see also Berberian et al, 1991). Jackson & McKenzie (1984) suggested that the more easterly oriented slip vectors observed further south (e.g. the slip vector of 42° in 1962.09.01) represent the direction of regional convergence between Iran and South Caspian. As a consequence, there should be a component of left-lateral slip in the Alborz Mountains. In the high Alborz Mountains, it appears that this oblique regional convergence is partitioned into strike-slip (1990.06.20) and reverse faulting (1983.07.22) whereas it remains as oblique slip in the lower elevations to the south in north-central Iran. The component of left-lateral slip in the Alborz Mountains is small, which may account for the apparent infrequency of strike-slip faulting earthquakes in the range.

The confirmed existence of adjacent strike-slip and thrust mechanisms with nearly perpendicular slip vectors in the NW Alborz Mountains makes us unsure of the actual slip vector for the strike slip events near thrust events elsewhere in the Alborz Mountains, which is why we include both possible slip vectors for 1983.03.26 and 1990.01.20. If the EW nodal planes were the fault planes in these earthquakes, their slip vectors are similar and in the same sense as for the 1990 Rudbar-Tarom earthquake. In this case, these events too are evidence for partitioning of strike-slip and thrust motion in the Alborz. South of the high Alborz Mountains, in the Central Iranian Plateau, the motion is apparently not partitioned and occurs as faults with oblique slip (e.g. 1962.09.01, 1980.12.19, 1980.12.22).

Most slip vectors in the Alborz are directed NE (Fig. 31) consistent with convergence between central Iran and the south Caspian Basin. Apart from the strike slip events, which we havediscussed above, the only exception is a small ($M_W 5.1$) normal faulting event (1988.08.23) for which only a Harvard CMT solution is available (Fig. 30b). We

are uncertain how to assess this event and cannot evaluate the reliability of the solution. There are no other normal fault solutions like it in the Alborz (The 1970.07.30 Karnaveh earthquake, although it had a normal component, had a slip vector consistent with the NE motion between Iran and the south Caspian Basin). Below a certain threshold in magnitude it is quite common for small events to have a greater variety of mechanisms than the larger events (e.g. Lyon - Caen et al, 1988). Taymaz et al (1991) report a well-constrained reverse-faulting event of $M_W 5.5$ in a region of NW Turkey that is dominated by normal faulting. With only one anomalous event (that is probably not well constrained) in the Alborz, we cannot assess its significance further. The component of normal faulting seen in 1970.7.30 suggests that the low elevations and thick sediments in the Turkmenian Lowlands, (Fig. 22a) may be partly related to extension-induced subsidence.

The Kopet Dag Mountains: The Kopet Dag has an abrupt northeast topographic front (Fig. 22a) that was associated with a large earthquake in 1948 near the city of Askhabad. Field and teleseismic data for this earthquake are ambiguous (Rustanovich & Shirakova, 1964; Tchalenko, 1975; and Jackson & McKenzie, 1984), but several authors associate the linearity of the abrupt topographic scarp with right-lateral strike-slip motion, whereas elsewhere in the Kopet Dag there is certainly thrust faulting with northeast directed slip vectors. One other event (1984.02.22, Figure 3Ga) further NW is consistent with right lateral strike-slip on this trend. The Kopet Dag may thus be another example of partitioning of strike-slip and thrust motion that are postulated to occur in the Alborz Mountains.

Central Caspian Seismic Belt: In the belt of seismicity which extends across the central Caspian Sea following the Apsheron - Balkan sill, normal faulting mechanisms with an ESE strike and focal depths of 30-50 km dominate. It is improbable that the normal faulting events represent the motion between the southern Caspian and Eurasia. If the steep nodal planes were the fault planes, then the sense of motion, north side down, is the reverse of that seen in the bathymetry, i.e., deep water and thick sediments to the south; if the nodal planes dipping gently south were the fault planes, some expression of extension might be expected at the surface. Yet seismic reflection surveys report folding of the surface sediments (Zonenshain & Le Pichon, 1986), suggesting shortening. This is compatible with the high angle reverse faulting mechanism that we postulate for a possible second sub-event of the 1986.03.06 earthquake at a shallower depth than the normal faulting earthquakes. The CMT solution for the 1987.12.19 earthquake (Fig.30b) shows reverse faulting with a NW-SE strike, and supports this interpretation. However, it was a small $(M_W 4.9)$ event, and in the light of the anomalous small event (1988.08.23) in the Alborz Mountains (Fig. 30b), we do not place much confidence in it.

We suspect that shortening occurs as the continental crust of the northern Caspian is thrust over the "oceanic" crust of the southern Caspian Basin, and that the normal faulting events occur in the deep (possible mantle) basement of the material being overthrust. It is possible that a subducting mantle slab with very low seismicity dips north beneath the Apsheron-Balkhan sill, accounting for the north-dipping T axes of the normal faulting solutions. Another possibility is that the normal faulting is the result of plate bending

exceeding the elastic strain limit as the north side of the Caspian Sea is thrust over the south Caspian Basin. This would be analogous to the normal faulting seaward of the oceanic trench and is a possible cause of the normal faulting beneath the Ganges Basin south of the Himalayas thrust front (Lyon-Caen & Molnar, 1985). The low level of seismic shortening across the central Caspian suggests that most of the Iran-Eurasia shortening is accommodated in the much more active Alborz thrust belt. The seismicity of the trans-Caspian belt continues northwest into the Caucasus and southeast into the Kopet Dag. Reverse faulting and thrusting on ESE striking planes are dominant in both of these areas.

DISCUSSION

The two most important new results that our study demonstrates are the partitioning of thrust and strike slip motion in the Alborz, and the existence of a belt of normal faulting earthquakes across the central Caspian Sea. Both have important implications for the tectonics of the region.

The partitioning of oblique shortening into pure thrust and pure strike-slip motion is not particularly rare, though there is some debate as to why it occurs (e.g. McKenzie & Jackson 1983, Zoback et al., 1987, Mount & Suppe 1987, Molnar 1991). McKenzie & Jackson (1983) point out that, if fault-bounded blocks move in response to forces imposed on their bases by continuous flow in the mantle lithosphere beneath the seismogenic upper crust, then oblique slip on faults oriented obliquely to the strike of the deforming zone cannot accommodate large finite deformation because they rotate about a vertical axis as they move. One way in which the faults can take up large finite strains is if the motion on them is partitioned into pure shortening and pure strike slip. A clue to this process may lie in the observation that the motion is partitioned in the high Alborz, where strains are obviously large, but not in the lower elevations of north-central Iran, where strains are presumably smaller. The faults may have become organized into a stable geometry as the strain increased. This may explain why partitioning is common in other places where strainsare large, such as in California (e.g. Mount & Suppe, 1987), the NW Zagros and NE Kopet Dag Mountains of Iran (Tchalenko & Braud, 1974; Tchalenko, 1975; Jackson & McKenzie , 1984) and in island arcs (e.g. Fitch, 1972), but oblique slip is by no means rare in places where total strain is probably relatively small, such as in the lower elevations of central Iran (Jackson & McKenzie, 1984). If partitioning really does occur because it is the favored way for crustal rocks to accommodate large-scale and large magnitude oblique motion, then knowledge of the orientations of stress in the upper crust adjacent to such faults will provide little insight into the dynamics of the deformation, as pointed out by Molnar (1991).

The significance of the normal faulting earthquakes in the belt across the central Caspian Sea is enigmatic. For reasons expressed above we do not believe that they represent a southward motion of the Caspian Sea relative to Eurasia. Shortening at depths shallower than the normal faulting is implied by the orientation of folds in the sediment, a possible (but ambiguous) second sub-event of the 1983.03.06 earthquake that involved reverse faulting, and a CMT solution for a small (and probably not well-constrained) earthquake that involved thrusting on 1987.12.19 (Fig 30b). We suspect that this shortening

does indeed represent a NNE motion of the south Caspian basin relative to Eurasia, but that the motion is slow and has not produced many earthquakes. In this respect the convergence may be similar to that in the Makran of SE Iran (Jackson & McKenzie, 1984) and along the Washington - Oregon coast of the NW United States (Heaton & Kanamori, 1984), both of which have rather low levels of seismicity, but may be capable of generating infrequent large earthquakes. Our preferred interpretation of the normal faulting events is that they are related to either bending or shallow down-dip extension of a slab of mantle lithosphere attached to and beneath the Caspian Sea, as it is overthrust by Eurasia, but this interpretation cannot be regarded as conclusive. If the motion of the Caspian Sea relative to Eurasia is indeed slow, then the motion in the Alborz between central Iran and the south Caspian Basin will be almost the same as that between Iran and Eurasia, as was assumed by Jackson & McKenzie (1984) in their analysis of the tectonics of Iran.

We conclude that the active tectonics implied by the observed faulting in the Talesh, Alborz and central Caspian Sea will lead to the eventual destruction of the south Caspian Basin and perhaps the formation of an intermediate depth, dipping seismic zone in the continental interior, similar to that presently observed in the Hindu Kush.

ACKNOWLEDGEMENT

REFERENCES

Adamia, S.A., Lordkipanidze, M.B, & Zakariadze, G.S, 1977. Evolution of an active continental margin as exemplified by the Alpine history of the Caucasus, *Tectonophysics*, *40*, 183-199.

Ambraseys, N.N., 1963. The Buyin-Zara (Iran) earthquake of September, 1962: a field report, *Bull. Seism. Soc. Am.*, *53*, 705-740.

Ambraseys, N.N., & Melville, C.P., 1982. *A History of Persian Earthquakes*, Cambridge University Press, 219p.

Amurrsski, G.I., Tiunov, K.V., Khrikov, B.A., & Shlezinger, A.E., 1968. Structure and tectonic position of the Great Balkhan, *Akademii Nauk SSSR*, 53p.

Berberian M., & Arshadi, S., 1976. On the evidence of the youngest activity of the North Tabriz fault and the seismicity of Tabriz city, Rep. Geol. Surv. Iran, No. 39, 397-418.

Berberian, M., & King, G.C.P., 1981. Towards a paleogeography and tectonic evolution of Iran, Can. J. of Earth Sci., 18, 210-265.

Berberian, M., 1983. The Southern Caspian: A compressional depression floored by a trapped, modified oceanic crust, Can. J. Earth Sci., 20, 163-183.

Berberian, M., Qorashi, M., Jackson, J.A., Priestley, K.F., Wallace, T., The Rudbar-Tarom earthquake of 20 June 1990 in NW Persia: preliminary field and seismological observations, and its tectonic significance, Bull. Seism. Soc. of Am., in press

Fedynsky, V.V., Fomenko, K.E., Garkalenkov, J.A., Goncharov, V.P., Khrychev, B.A., Malovitsky, Y.P., Milashin, A.P., Neprochnov, Y.P., & Ushakov, S.A., 1972. The Earth's crust of the inland seas and continental depressions of the west Tethys region, 24th International Geological Congress, Montreal, P.Q. Section 3, 51-57.

Fitch, T.J., 1972. Plate convergence, transcurrent faults, and internal deformation adjacent to southeast Asia and the western Pacific, J. Geophys. Res., 77, 4432-4460.

Fredrich, J., McCaffrey, R., & Denham, D., 1988. Source parameters of seven large Australian earthquakes determined by body waveform inversion, Geophys. J., 95, 1-13.

Futterman, W.I., 1962. Dispersive body waves, J. Geophys. Res., 67, 5279-5291.

Galperin, E.I., Kosminskaya I.P., & Krakshina, P.M., 1962. Main characteristics of deep waves registered by deep seismic sounding in the central part of the Caspian Sea, Deep Sounding of the Earth's Crust in the USSR. Moscow. Gosloptekhizdat, 227-250, (in Russian).

Gao, L., & Wallace, T.C., 1991. Aftershocks of the 1990 western Iran (M_W 7.3) earthquake, Bull. Seism. Soc. Am., to be submitted.

Golensky, G.L, Kondorskya, N.V., Zakarova, A.E., Vandeshiva, N.V., Agalapova, E.B., Agamepzor, S.R., Bruk, M.G., Garagozov, D., Kuleiv, F.T., Logova, N.A., Muragov, C.M., Rautian, T.G., Panake, B.M., Rakemov, A.R., Rogozhen, E.A., Shafadeyaiv, R.H., & Chepkunac, L.C., 1989. The Caspian earthquake of March 6, Earthquakes in the U.S.S.R. in 1986, Akademii Nauk SSSR, 58.

Heaton, T.H., & Kanamori, H., 1984. Seismic potential associated with subduction in the northwestern United States, Bull. Seism. Soc. Am., 74, 933-947.

Jackson, J.A., & Fitch, T.J., 1979. Seismotectonic implications of relocated aftershock sequences in Iran and Turkey, Geophys. J. R. astr. Soc., 57, 209-229.

Jackson, J.A., & Fitch, T.J., 1981. Basement faulting and the focal depths of the larger earthquakes in the Zagros mountains (Iran), Geophys. J. R. astr. Soc., 64, 561-586.

Jackson, J., & M. Kenzie, D., 1984. Active tectonics of the Alpine-Himalayan Belt between western Turkey and Pakistan, Geophys. J. R. astr. Soc., 77, 185-264.

Kadinsky-Cade, K., Barazangi, M., Oliver, J., & Isacks, B., 1981. Lateral variations of high frequency seismic wave propagation at regional distances across the Turkish and Iranian plateaus, J. Geophys. Res., 86, 9377-9396.

Letouzey, J., Biju-Duval, B., Dorkel, A., Gonnard, R., Kristchev, K., Montadert, L., & Sungurlu, O., 1977. The Black Sea: A marginal basin, geophysical and geological data, In: Biju-Duval, B., & Montadert, L., (editors), International Symposium on the Structural History of the Mediterranean Basin, Edition Technip, Paris, 363-379.

81

Lyon-Caen, H., & Molnar, P., 1985. Gravity anomalies, flexure of the Indian Plate, and the structure, support and evolution of the Himalaya and Ganga Basin, *Tectonics*, *4*, 513-538.

Lyon-Caen, H., Armijo, R., Drakopoulos, J., Baskoutas, J., Delibassis, N., Gaulon, R., Kouskouna, V., Latoussakis, J., Makropoulos,K., Papadimitrious, P., Papanastassiou, D., & Pedotti, G.,1988. The 1986 Kalamata (S. Peloponessos) earthquake: Detailed study of a normal fault and tectonic implications, *J. Geophys. Res.*, *93*, 14,967-15,000.

Malovitsky, Y.P., 1968. History of the geotectonic development of the depression of the Caspian Sea, *Izvestiya Akademii Nauk SSSR, Seriya Geologicheskaya, 10*, 103-120.

Malovitsky, Y.P., Levin, L.E., Milashin A.P., & Zorina, Y.G., 1970. Gruppa Youshnykh Morey. Tektonika I Neftegazonosnost Okrunnykh I Vnutrennykh Morey SSSR, Nedra, Moscow.

McCaffrey, R., & Nabelek, J., 1987. Earthquakes, gravity, and the origin of the Bali Basin: an example of a nascent continental fold-and-thrust belt, *J. Geophys. Res.*, *92*, 441-460.

McCaffrey, R., & Abers, G., 1988. SYN3: A program for inversion of teleseismic body wave forms on microcomputers, Air Force Geophysics Laboratory Technical Report, AFGL-TR-88-0099, Hanscom Air Force Base, MA, 50p.

McKenzie, D.P., & Jackson, J.A., 1983. The relationship between strain rates, crustal thickening, paleomagnetism, finite strain and fault movements within a deforming zone, *Earth Planet. Sci. Lett.*, *65*, 182-202, and correction, idib., 1984. *70*, 444.

Molnar, P., 1991. Brace-Goetze strength profiles, the partitioning of strike-slip and thrust faulting at zones of oblique convergence, and the stress-heat flow paradox of the Andreas Fault, *In:* The Brace Volume, Evans B., & Wong, T.F., (editors), in press.

Molnar, P., & Lyon-Caen, H., 1989. Fault plane solutions of earthquakes and active tectonics of the Tibetan Plateau and its margin, *Geophys J. Int. 99*, 123-153.

Mount, V.S., & Suppe, J., 1987. State of stress near the San Andreas Fault: implications for wrench tectonics, *Geology, 15*, 1143-1146.

Muratov, M.V., 1972. Formation history of the deep Black Sea basin as compared with deep basins of the Mediterranean, *Geotektonika, 5*, 22-41 (in Russian).

Nabelek, J., 1984. Determinations of earthquake source parameters from inversion of body waves, *Ph.D. thesis*, M.I.T., Cambridge, MA.

Neprochnov, Y.P., 1968. Structure of the Earth's crust of epicontinental seas: Caspian, Black and Mediterranean, *Can. J. of Earth Sci.*, *5*, 1037-1043.

Nowroozi, N.N., 1972. Focal mechanism of earthquakes in Persia, Turkey, West Pakistan and Afghanistan and plate tectonics of the Middle East, *Bull. Seis. Soc. Am.*, *62*, 823-850.

Rezanov, I.A., & Chamo, S.S., 1969. Reasons for absence of a granitic layer in basins of the South Caspian and Black Sea type, *Can. J. of Earth Sci.*, *6*, 671-678.

Rustanovich, D.N., & Shinakova, E.I., 1964. Some results of a study of the Askhabad earthquake of 1948, *Izvestiya Akademii Nauk SSSR, Seriya Geofizika*, 1077-1080.

Shikalibeily, E.S., & Grigoriants, B.V., 1980. Principal feature of the crustal structure of the south Caspian basin and the conditions of its formation, *Tectonophysics, 69*, 113-121.

Shlezinger, A.Y., 1981. Structure of the Sedimentary Cover of the Black Sea Basin, *In:* Peive A.V. & Pushcharovskii, Y.N., (editors), *Problemy Tektoniki Zemnoi Kory*, Nauk, Moscow, 237-262 (in Russian).

Smith, K.D., Brune, J.N., & Priestley, K.F., 1991. The seismic spectrum, radiated energy, and the Savage and Wood inequality for complex earthquakes, *Tectonophysics*, *188*, 303-320.

Sorokhtin, O.G. (editor), 1979. Geodynamics, *In*: Okeanologiya. *Geofizika Okeanshogo Dna*. Nauk. Moscow, *2*, 375 (in Russian).

Taymaz, T., Jackson, J.A., & Westaway, R., 1990. Earthquake mechanisms in the Hellenic Trench near Crete, *Geophys. J. Int.*, *102*, 695-731.

Taymaz, T., Jackson, J., & McKenzie, D., 1991. Active tectonics of the north and central Aegean Sea, *Geophys. J. Int.*, 106, 433-490.

Tchalenko, J.S., 1975. Seismicity and structure of the Kopet Dagh (Iran, USSR), *Phil. Trans. R. Soc.*, *278*, 1-25.

Tchalenko, J.S., 1977. A reconnaissance of the seismicity and tectonics at the northern border of the Arabian plate; Lake Van region, *Rev. Geogr. Phys. Geol. Dyn*, *19*, 189-208.

Tchalenko, J.S., & Braud, J., 1974. Seismicity and structure of the Zagros (Iran): the Main Recent Fault between 33 and 35°N, *Phil. Trans, R. Soc. A*, *277*, 1-25.

Vardapetyan, A.N., 1981. Late Cenozoic plate tectonics of the Black Sea-Caspian region, Ph.D. thesis, Inst. of the Oceanology, Moscow, 24 (in Russian).

Yanshin, A.L., Bassenyants, S.A., Pilipenko A.I., & Shlezinger, A.E., 1980. New Data on the time of formation of the Black Sea deep basin, *Dokl. Akad. Nauk SSSR*, *252*, 223-227 (in Russian).

Zoback, M.D., Zoback, M.L., Mount, V.S., Suppe, J., Eaton, J.P., Healy, J.H., Oppenheimer, D., Reasenberg, P., Jones, L.M., Raleigh, C.B., Wong, I.G., Scotti, O., & Wentworth, C., 1987. New evidence on the state of stress of the San Andreas fault system, *Science*, *238*, 1105-1111.

Zonenshain, L.P., & Le Pichon, X., 1986. Deep basins of the Black Sea and Caspian Sea as remnants of Mesozoic back-arc basins, *In*: Aubouin, J., Le Pichon, X., & Monin, A.S., (editors), *Evolution of the Tethys, Tectonophysics*, *123*, 181-211.

Table 1 : Earthquake Hypocentral Data

d	Date m	y	Origin Time	Latitude (°N)	Longitude (°E)	Depth(km) P	pP	m_b	Ms	Source*	Number of Stations
2	7	1957	00:42:23	36.14	52.70	10			6.8	ISS	
1	9	1962	19:20:40	35.63	49.87	27			7.2	ISS	
3	1	1969	03:16:37	37.10	57.83	4		5.4		ISC	163
30	7	1970	00:52:20	37.85	55.94	22		5.7		ISC	306
14	2	1971	16:27:32	36.62	55.74	4		5.3		ISC	236
3	2	1976	16:40:41	39.93	48.41	67		5.2		ISC	226
25	5	1977	11:01:47	34.91	52.06	39	41	5.3		ISC	258
4	11	1978	15:22:19	37.71	48.95	37	36	6.0	6.1	ISC	418
1	10	1979	07:37:01	40.07	51.87	42	47	5.0	4.4	ISC	150
9	12	1979	09:12:04	35.14	56.87	23		5.2	5.5	ISC	248
4	5	1980	18:35:19	38.09	49.07	36	36	5.3	6.1	ISC	323
22	7	1980	05:17:08	37.36	50.35	37	36	5.3	5.1	ISC	238
3	12	1980	04:26:15	37.17	50.47	44	22	5.1	4.7	ISC	233
19	12	1980	01:16:56	34.50	50.67	29	43	5.5	5.8	ISC	354
22	12	1980	12:51:21	34.49	50.67	39	18	5.4	5.2	ISC	299
4	8	1981	18:35:43	38.21	49.41	40	29	5.4	5.2	ISC	358
19	11	1981	14:10:37	40.78	49.26	42	42	5.1	4.2	ISC	236
26	3	1983	04:07:19	36.06	52.28	33	25	5.4	4.9	ISC	261
22	7	1983	02:41:01	36.98	49.23	43	33	5.6	5.0	ISC	299
22	2	1984	05:44:37	39.52	54.11	0		5.1	5.8	ISC	296
29	10	1985	13:13:40	36.75	54.81	13	8	6.0	6.0	ISC	518
6	3	1986	00:05:37	40.37	51.60	28	63	6.1	6.2	ISC	614
11	6	1986	20:15:41	40.28	51.71	41	49	5.2	4.6	ISC	305
10	4	1987	06:43:20	37.21	57.70	6	35	5.0		ISC	226
7	9	1987	11:32:27	39.37	54.76	39		5.5	5.5	ISC	442
19	12	1987	08:27:36	40.72	52.05	80	67	4.9		ISC	198
23	8	1988	05:30:51	35.42	52.28	35	25	5.0	4.8	ISC	249
16	9	1989	02:05:09	40.34	51.53	55		6.4	6.5	PDE	563
17	9	1989	00:53:40	40.20	51.75	51		6.1	6.1	PDE	533
20	1	1990	01:27:10	35.83	52.95	25		5.5	5.9	PDE	348
20	6	1990	21:00:10	36.96	49.41	19		6.4	7.7	PDE	352

*ISS International Seismological Summaries (- 1963)
ISC International Seismological Center (1964 - 1988)
EDR Earthquake Data Reports (1989 - 1990)
PDE Preliminary Determination of Epicenters (1990 -)

Table 2 : Source Mechanism Data

d	m	y	Depth (km)	Mo x10^{17} Nm	M_W	Strike	Dip	Rake	Slip* Vector	P	SH
1	9	1962	10±4	367.8	7.0	$101° \pm 10°$	$52° \pm 3°$	$70° \pm 15°$	$42°$	10	4
3	1	1969	7±4	1.9	5.5	$132° \pm 15°$	$50° \pm 5°$	$95° \pm 8°$	$33°$	6	4
30	7	1970	11±4	42.9	6.3	$293° \pm 20°$	$56° \pm 5°$	$210° \pm 10°$	$23°$	23	16
14	2	1971	11±5	4.0	5.7	$336°$	$39°$	$93°$	$62°$	9	
4	11	1978	21±5	19.0	6.1	$346° \pm 15°$	$79° \pm 4°$	$95° \pm 20°$	$77°$	22	16
4	5	1980	15±5	40.2	6.3	$181° \pm 10°$	$84° \pm 10°$	$267° \pm 15°$	$91°$	21	17
19	12	1980	14±8	14.0	6.0	$115° \pm 20°$	$41° \pm 8°$	$120° \pm 15°$	$25°$	10	11
22	12	1980	15±5	2.8	5.6	$113° \pm 20°$	$56° \pm 8°$	$125° \pm 15°$	$23°$	4	8
4	8	1981	20+8	2.4	5.6	$154° \pm 15°$	$35° \pm 15°$	$32° \pm 20°$	$64°$	15	10
22	7	1983	10±8	1.9	5.6	$120° \pm 20°$	$35° \pm 8°$	$83° \pm 15°$	$30°$	10	7
22	2	1984	27±4	5.1	5.7	$106° \pm 20°$	$60° \pm 10°$	$174° \pm 20°$	$16°$	7	21
29	10	1985	13±5	21.8	6.2	$246° \pm 15°$	$66° \pm 10°$	$71° \pm 10°$	$16°$	31	14
6	3	1986a	31	25.2	6.2	$299° \pm 15°$	$88° \pm 5°$	$275° \pm 8°$	$29°$	35	15
6	3	1986b	13±4	21.8	6.2	$114° \pm 15°$	$63° \pm 5°$	$87° \pm 8°$	$23°$	35	15
7	9	1987	30±8	2.3	5.5	$305° \pm 10°$	$10° \pm 10°$	$103° \pm 20°$	$22°$	14	12
16	9	1989	31±10	68.4	6.5	$80° \pm 15°$	$26° \pm 5°$	$225° \pm 15°$	$38°$	22	14
17	9	1989	35±10	21.7	6.2	$277° \pm 15°$	$50° \pm 5°$	$249° \pm 15°$	$38°$	21	20

*Slip vector direction is for S or E side of fault relative to N or W side

Table 3 : Source Mechanisms From Other Studies.

Date d	Date m	Date y	Depth (km)[†]	M_o x10[17] Nm	M_w	Fault Plane Strike	Fault Plane Dip	Fault Plane Rake	Slip Vector	Source[*]
2	7	1957				256°	44°	259°	30°	M72
3	2	1976				298°	72°	184°	28°	JM84
25	5	1977				112°	60°	112°	22°	JM84
1	10	1979	35(F)	0.4	5.0	304°	20°	-63°	214°	HVD
9	12	1979	15(F)	2.8	5.6	350°	44°	121°	40°	HVD
22	7	1980	30	2.6	5.5	310°	70°	88°	40°	HVD
3	12	1980	16(F)	1.2	5.3	281°	57°	47°	11°	HVD
19	11	1981	33(F)	0.6	5.1	131°	73°	23°	41°	HVD
26	3	1983	10(F)	1.2	5.3	104°	61°	17°	14/96°	HVD
11	6	1986	50	0.8	5.2	291°	43°	-123°	201°	HVD
10	4	1987	15	0.5	5.1	292°	45°	30°	22°	HVD
19	12	1987	33(F)	0.3	4.9	322°	36°	110°	28°	HVD
23	8	1988	15(F)	0.6	5.1	348°	32°	-41°	204°	HVD
20	1	1990	33(F)	10.0	5.9	357°	66°	172°	0/87°	HVD
20	6	1990	14	880.0	7.2	292°	88°	-4°	112°	GW91

[†] (F) denotes fixed depth for moment sensor solution
[*] M72 first motion fault plane solution from McKenzie (1972)
JM84 first motion fault plane solution from Jackson and McKenzie(1984)
HVD Harvard Centroid Moment Tensor Catalogue
GW91 Moment tensor solution from Gao and Wallace (1991)

FIGURE CAPTIONS

Figure 21, Distribution of epicenters for earthquakes greater than magnitude 4 occurring in the region surrounding the Caspian Sea during the period 1962-1988. Epicenters are taken from the NEIS catalogue.

Figure 22. Map of the Caspian Sea region a) showing the 1,000, 2,000 and 3,000 m topographic contours, region of "oceanic-like" crust, contours of sediment thickness, and fold axes in sedimentary cover; b) showing region of "oceanic-like" crust, major fault systems, and seismicity (M $\geq$ 4) for the period 1962-1988. Geologic features and location of the "oceanic-like" crust are adapted from Shikalibeily & Grigoriants (1981), Berberian (1983) and Jackson & McKenzie (1984).

Figure 23. Lower hemisphere equal area projections of P-wave first motion polarity data. Station positions have been plotted with a velocity of 6.8 kms^{-1} beneath the source, the same as used in the waveform inversions. Filled circles are compressional first motions; open circles are dilational; nodal onsets are marked with crosses. Large symbols are polarities read on long-period WWSSN instruments, small symbols are polarities based on clear short-period seismograms whose onset displays the short-period impulse response (see Jackson & McKenzie, 1984). P- and T- axes are denoted by the letters P and T. Nodal planes are those of the minimum misfit waveform inversion solutions. Above each focal sphere is the event's date (year, month, day). Comments on individual first motion polarity plots accompany the discussion of each event in the appendix, except for 1978.11.04 and 1986.03.06 which are discussed in the main body of the text.

Figure 24. The P and SH radiation patterns of the minimum misfit solution for the 4 November 1978 (1978.11.04) earthquake are shown in the center of the upper and lower portions of this figure, respectively, and the corresponding values of strike, dip, slip (in degrees), centroid depth (in km), and seismic moment (in units of 10^{18}Nm) are listed beneath the event header. The focal spheres are shown with the P and SH nodal planes, in lower hemisphere projections. The P and T axes are marked by the solid and open circles, respectively. Surrounding the focal sphere, the observed P and SH waveforms (solid lines) are compared with synthetic waveforms (dashed lines) computed for the minimum misfit solution. For the waveform comparison, amplitudes have been normalized to that of an instrument with a gain of 3000 at an epicentral distance of 40°. The time windows for the waveform inversion are denoted by the solid, vertical lines on the waveform. The label to

the left of each waveform identifies the station code, an upper case letter corresponding
to the location on the focal sphere, and a lower case letter denoting the instrument type
(w = WWSSN LP, d = GDSN LP). The source time function is shown below the P-wave
focal sphere. Below the source time function is the waveform time scale. The waveform
amplitude scales are to the left of the focal spheres.

Figure 25. This shows the results of the source region velocity structure test for the 4
November 1978 event. To the left of the waveforms are the P and SH focal spheres and
source time function corresponding to the minimum misfit solutions for the particular test.
The strike, dip, rake, and centroid depth are listed above the focal spheres. The upper
row (A) of the observed (solid line) - synthetic (dashed line) comparison is for the velocity
structure used in determining the minimum misfit solution shown in Figure 24. Rows (B
- D) shows waveforms for minimum misfit solutions obtained for velocity structures B -
D below; all of which might represent reasonable crustal velocity models. These synthetic
waveforms are indistinguishable from those in Row A and the source orientations have
hardly changed. Rows E - F compare minimum misfit synthetics for more radical changes
in the source velocity structure, neither of which is probably reasonable for the Caspian
region. Row F is for a mantle source, but the centroid depth resulting from the inversion
is at the base of the crust. We conclude from these tests that the focal parameters strike,
dip, and rake are insensitive to reasonable variations in the velocity structure.

Velocity Structure	Depth To Interface (km)	V_p (kms^{-1})	V_s (kms^{-1})	density kgm-3
A	0.0	5.6	3.2	2600
	12.0	6.8	3.9	2900
B	0.0	6.2	3.6	2700
	13.2	6.8	3.9	2900
C	0.0	6.2	3.6	2700
	18.0	6.8	3.9	2900
D	0.0	6.5	3.8	2800
E	0.0	5.6	3.2	2500
F	0.0	6.2	3.6	2700
	25.0	8.1	4.7	3300

Figure 26. This figure summarizes the tests we have made to assess the uncertainties for the strike, dip, rake, and centroid depth for the 4 November 1978 earthquake. The format for this figure is the same as for Figure 25. Row A compares selected waveforms for the minimum misfit solution shown in Figure 24. Row B shows the comparison for the minimum misfit solution obtained when the depth is held fixed at 13 km but all other parameters are free. Rows C, D, and E show the similar comparison except when the strike, dip, and rake, respectively, are held fixed at the values shown after the source time function. The rake for this event is poorly constrained.

Figure 27. The minimum misfit solution for the 6 March 1986 earthquake in the central Caspian Sea. The figure format is the same as that for Figure 24. a) single source solution; b) double source solution.

Figure 28. This figure compares observed waveforms and synthetic waveforms computed for various inversion solutions for the 1986.03.06 earthquake. The figure format is the same as for Figure 25. Row A compares waveforms for the single source inversion solution; row B compares waveforms for the double source inversion solution. Note the improvement in the fits for the four nodal P-wave seismograms (SHL, KOD, PTO, STU). Rows C and D show the contribution of the two individual sources of the double source solution.

Figure 29. Comparison of waveforms at same common seismograph stations for the three largest central Caspian Sea earthquakes (1986.03.06, 1989.09.16, 1989.09.17). Dotted lines denote the synthetic seismograms computed for these from the minimum misfit solutions shown in Figures 27b, A13, A14 and given in Table 2. The amplitude scale (d-GDSN, w-WWSSN) is to the left of each row and all seismograms have a common time scale. All ststions are WWSSN except GDH which is a GDSN station.

Figure 30. Minimum misfit fault plane solutions of the earthquakes analyzed in this paper (Table 2) (a), and fault plane solutions for other earthquakes that we did not study (Table 3), from Jackson & McKenzie (1984), Gao & Wallace (1991), and the Harvard CMT catalogue (b). Focal spheres are lower hemisphere equal area projections, with compressional quadrants shaded. Next to each sphere is the date of the event (year, month, day). In (a) the centroid depth in km is noted near the epicenter. The focal mechanism of the 1990.06.20 event is denoted by the larger fault plane solution in 10b and its depth is noted near the epicenter.

Figure 31. Horizontal projection of the slip vectors for earthquakes whose focal mechanisms are shown in Figure 30. Heavy solid arrows are slip vectors from events whose P- and SH-waveforms we analyzed in this study (Fig. 30a) and from the 1990.06.20 earthquake (Gao & Wallace, 1991). Light open arrows are slip vectors from first motion solutions of Jackson & McKenzie (1984) or from Harvard CMT solutions (Fig. 30b). The sense of slip shown is of the south or east side of the fault relative to the north or west side. We have shown the slip vector implied by our minimum misfit solution for 1971.02.14 and labeled it 62° (?) to indicate that we do not have a great deal of confidence in this solution. The inset in the upper right-hand corner of the figure shows the orientation of the T axes of the normal faulting events in the central Caspian Sea

FIGURE 21

91

Topograpy

| | < 1000 m | | < 2000 m | | < 3000 m | | < 4000 m |

—— "Oceanic-like crust"

✓✓ Folds in Sedimentary Cover

·····20····· Sediment isopahs (km)
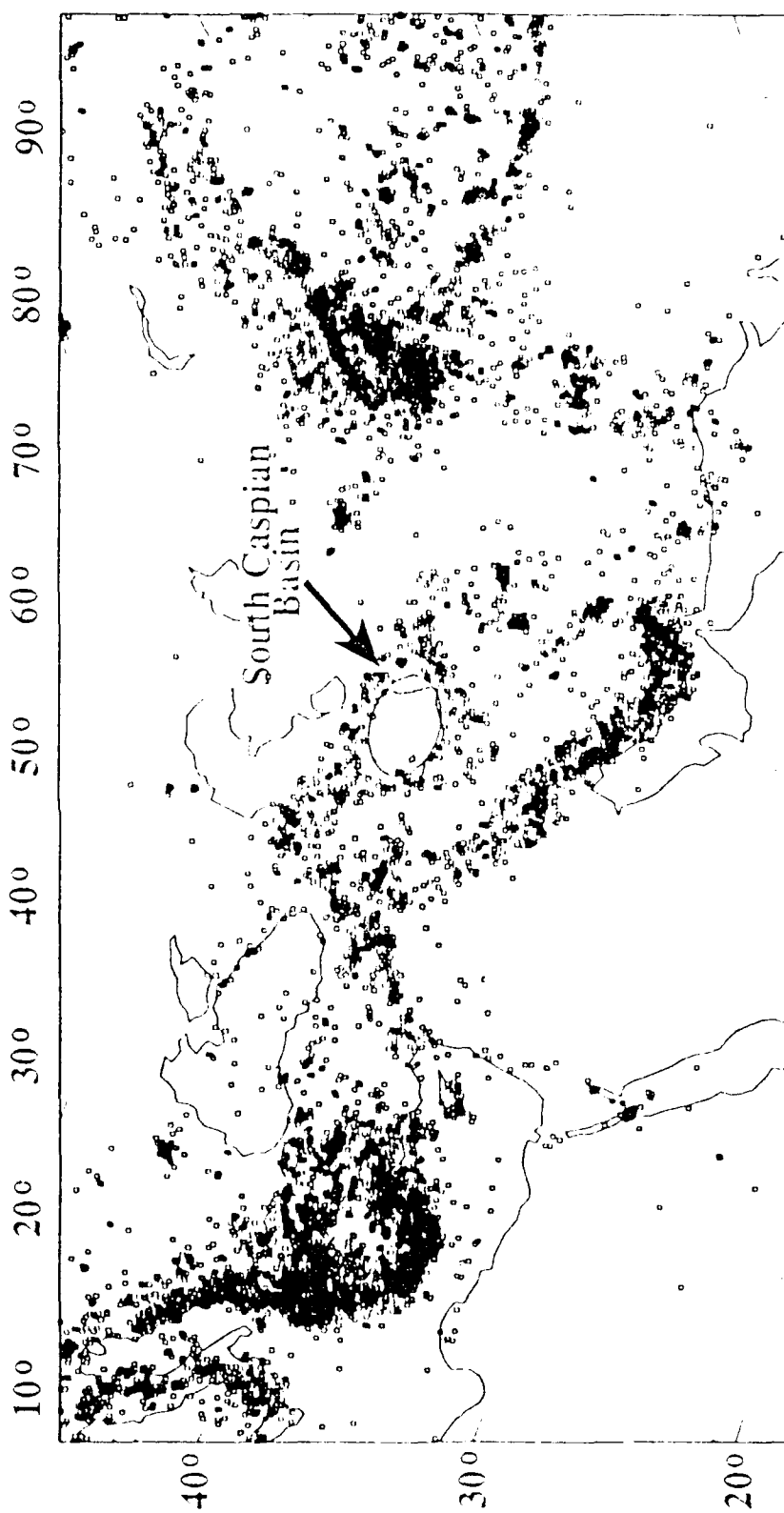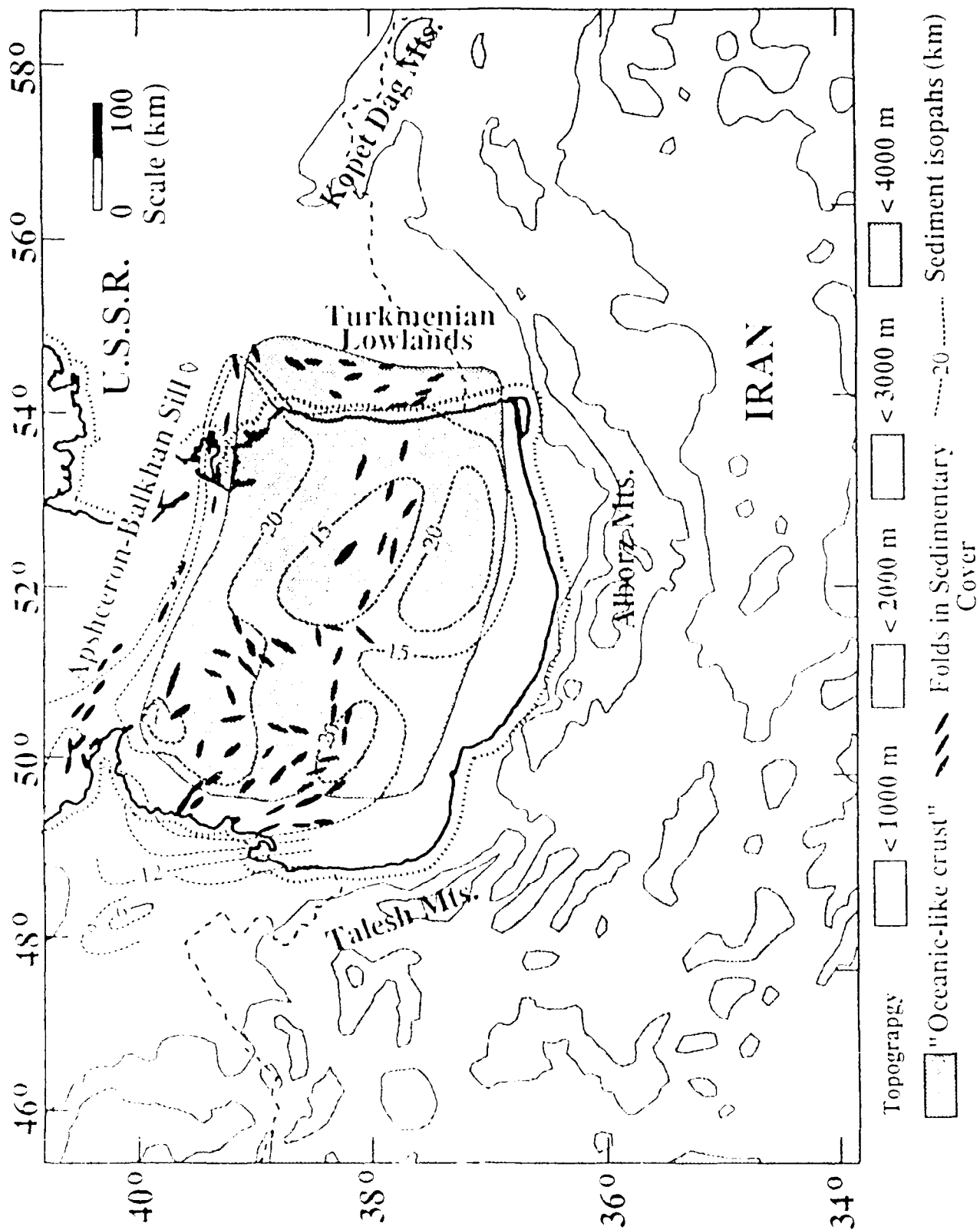
FIGURE 22a

AD-A255 667

STUDIES IN SEISMIC VERFICATION(U) MACKAY SCHOOL OF
MINES RENO NV SEISMOLOGICAL LAB   K PRIESTLEY 5 MAY 92
PL*-TR-92-2128 F19628-89-K-0022

1/2

NL

END
FILMED

DTIC

FIGURE 22b

U.S.S.R.

IRAN

Scale (km)

1962

1721

1786
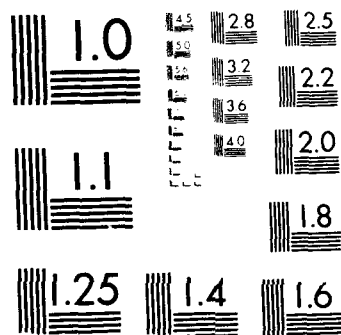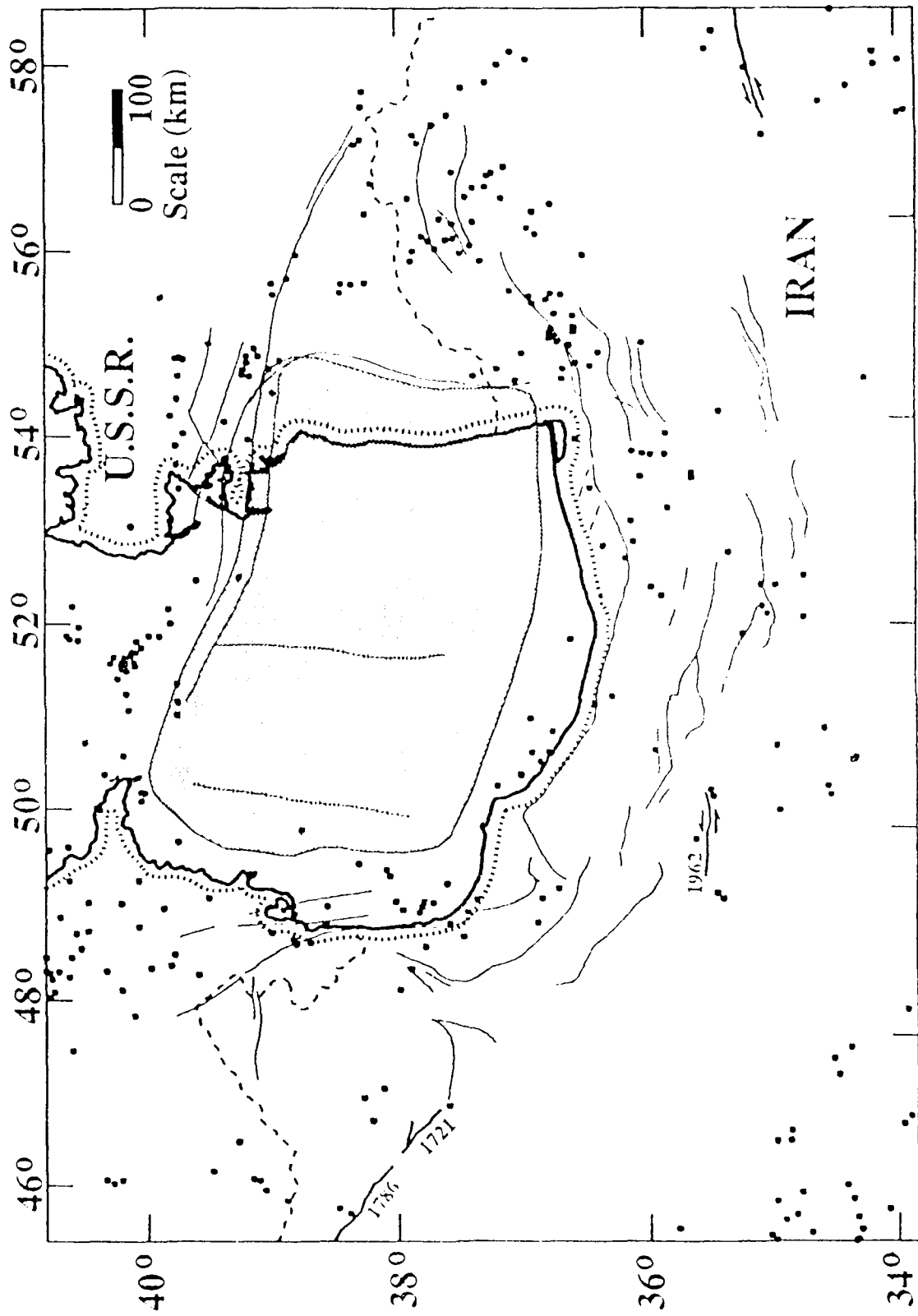
620901
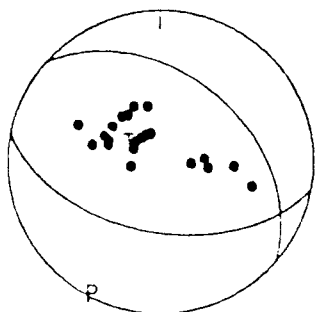
690103
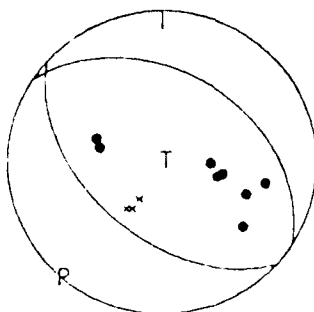
700730
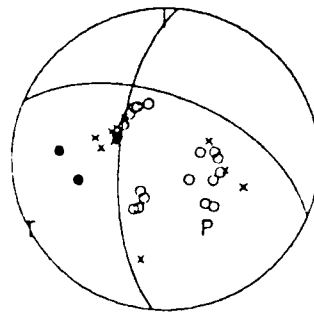
710214
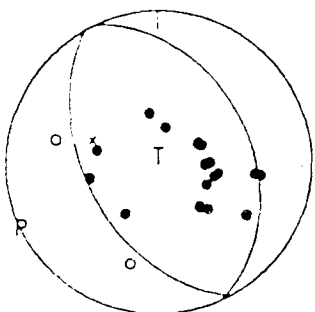
781104
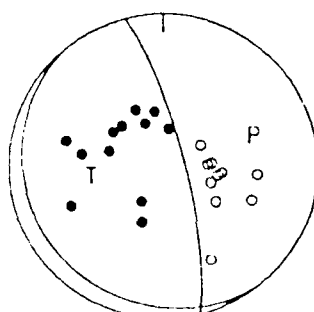
800504
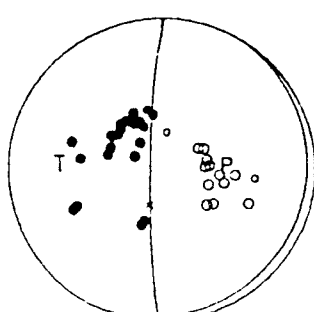
801219
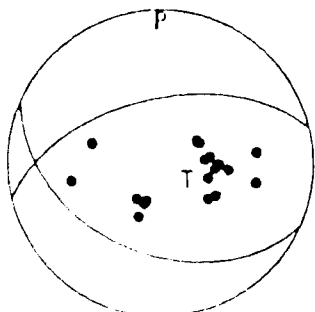
801222
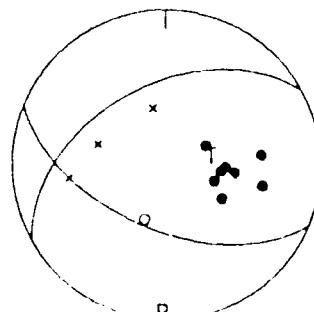
810804

FIGURE 23 Part 1

94
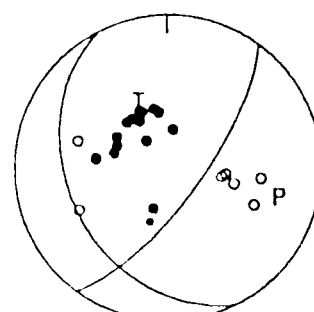
830722
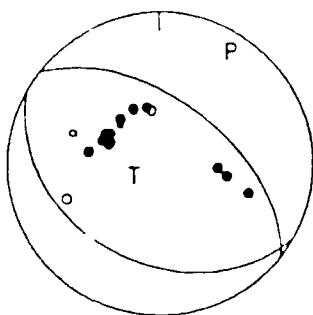
851029
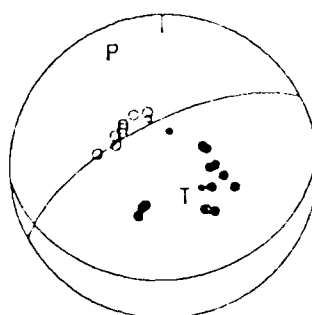
860306
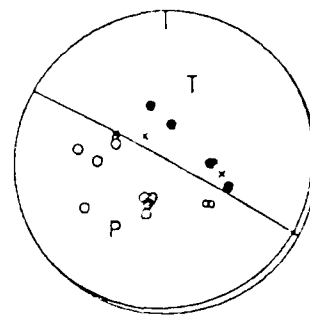
870907
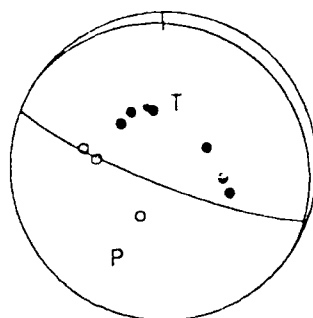
890916
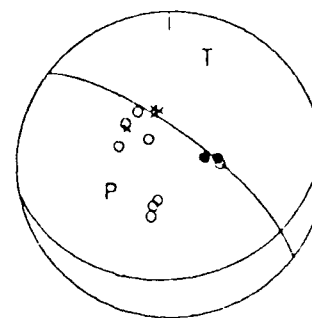
890917
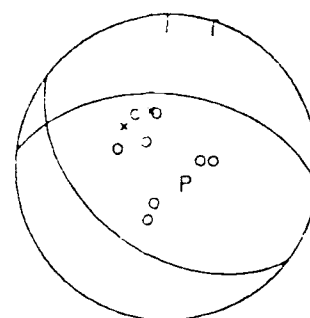
FIGURE 23 Part II

4 November, 1978
$346/79/95/21/1.90 \times 10^{18}$

FIGURE 24

FIGURE 25

346/79/95/21/1.902E18

346/80/97/23/1.729E18

346/80/97/22/1.737E18

346/81/98/23/1.468E18

346/81/100/25/1.165E18

346/83/100/25/2.093E18

A

B

C

D

E

F

TOL-S

AAE-S

TOL-P

SHK-P

14s STF

97

COL-P MAT-P POO-P KEV-P TOL-S MAL-S

Minimum Misfit Solution

Depth Test

Strike Test

Dip Test

Rake Test

13 km

6°

89°

105°

FIGURE 26

98
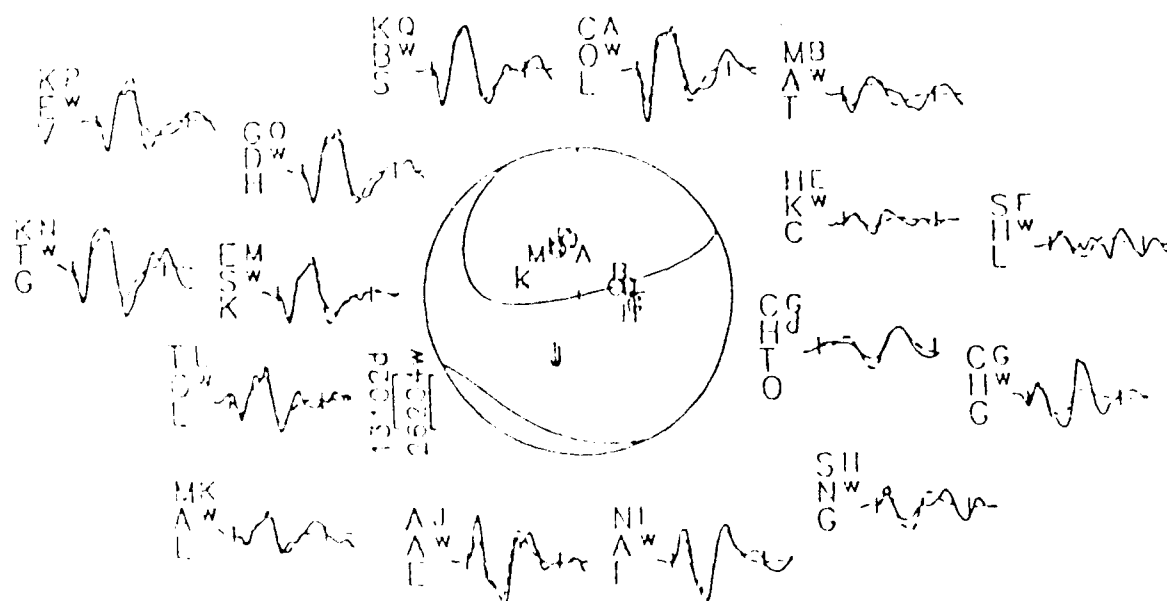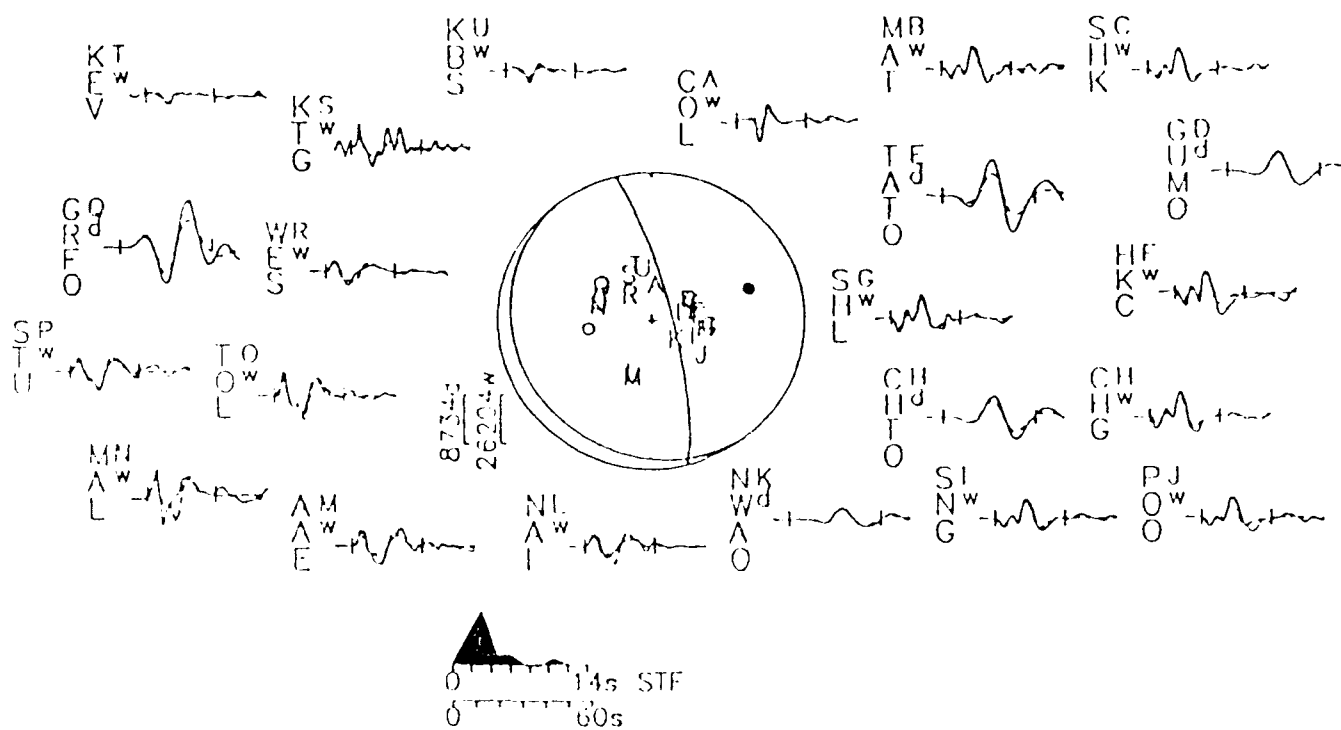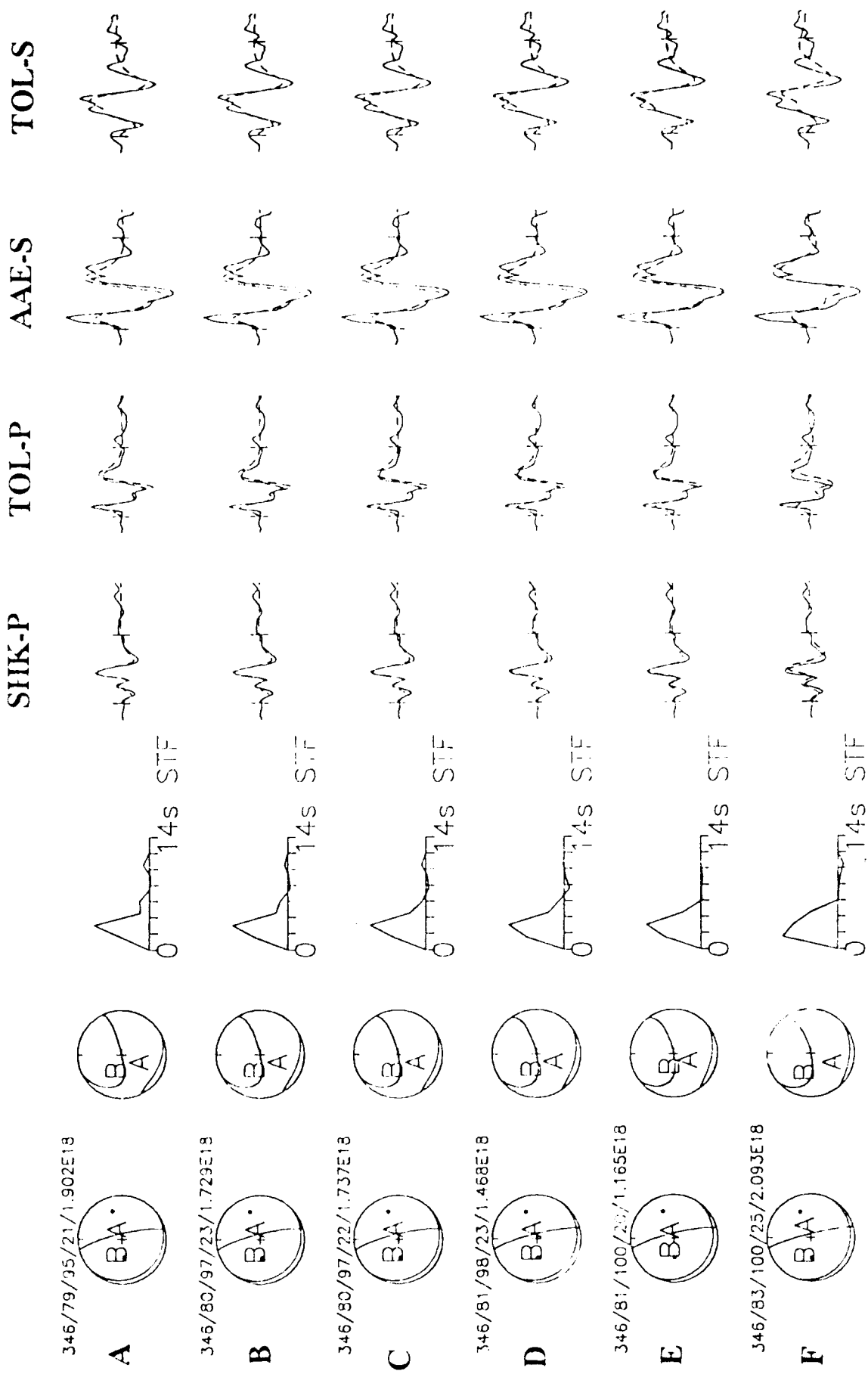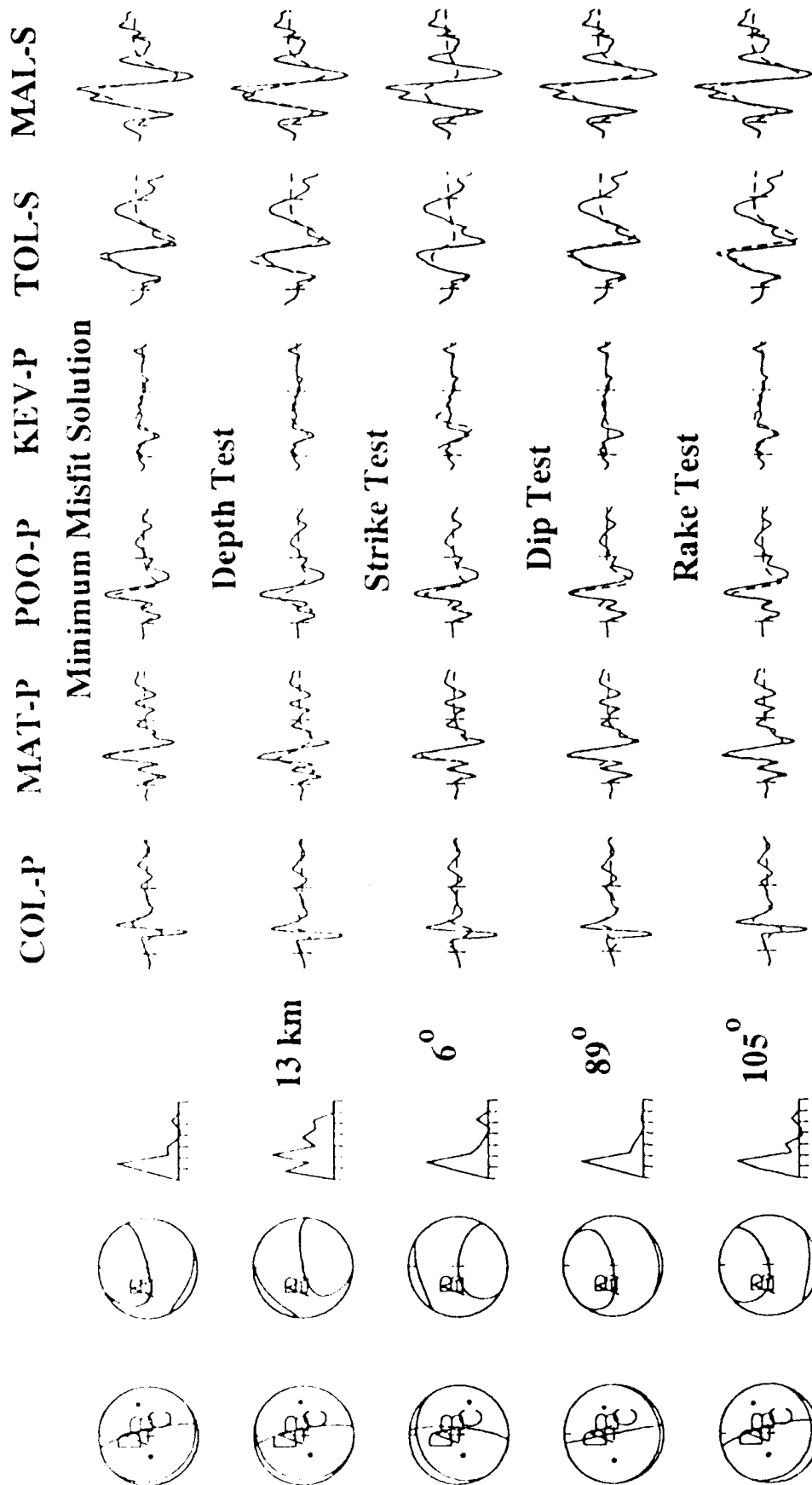
March 6, 1986
303/81/268/35/2.435E18

FIGURE 27a

99
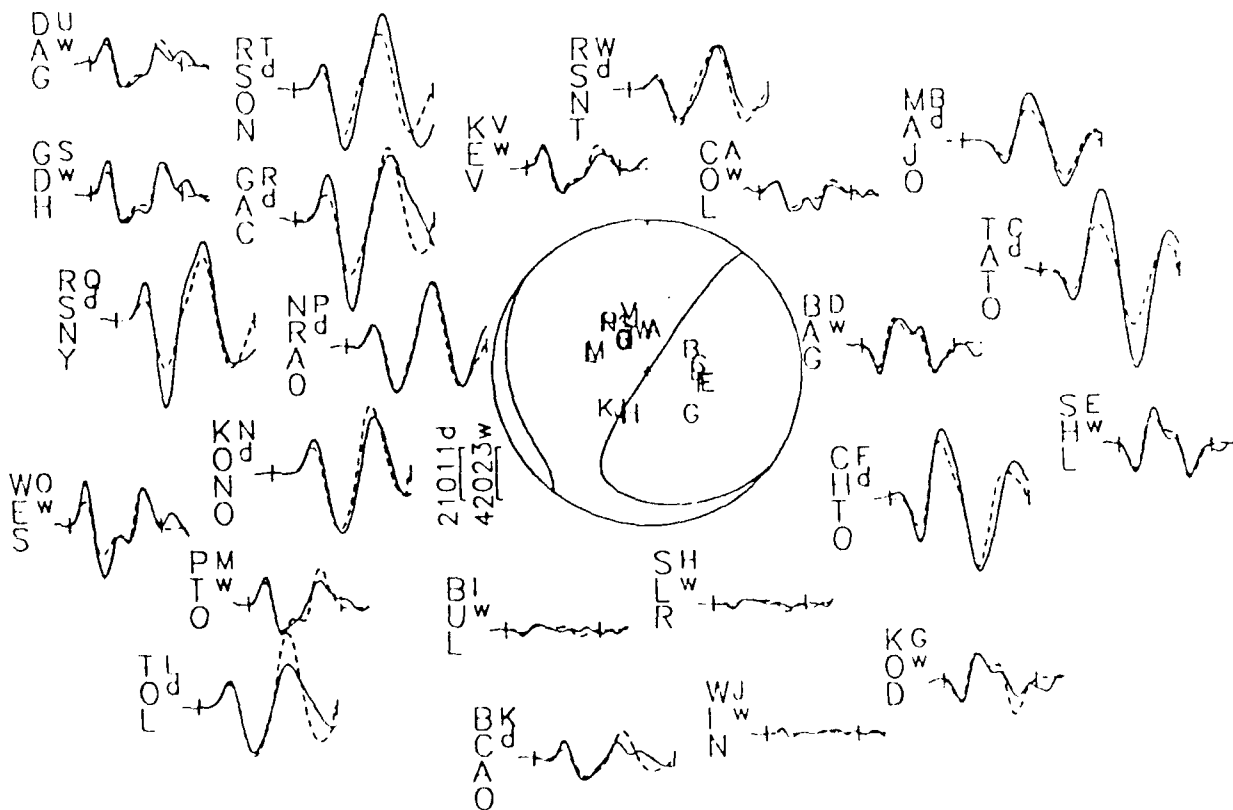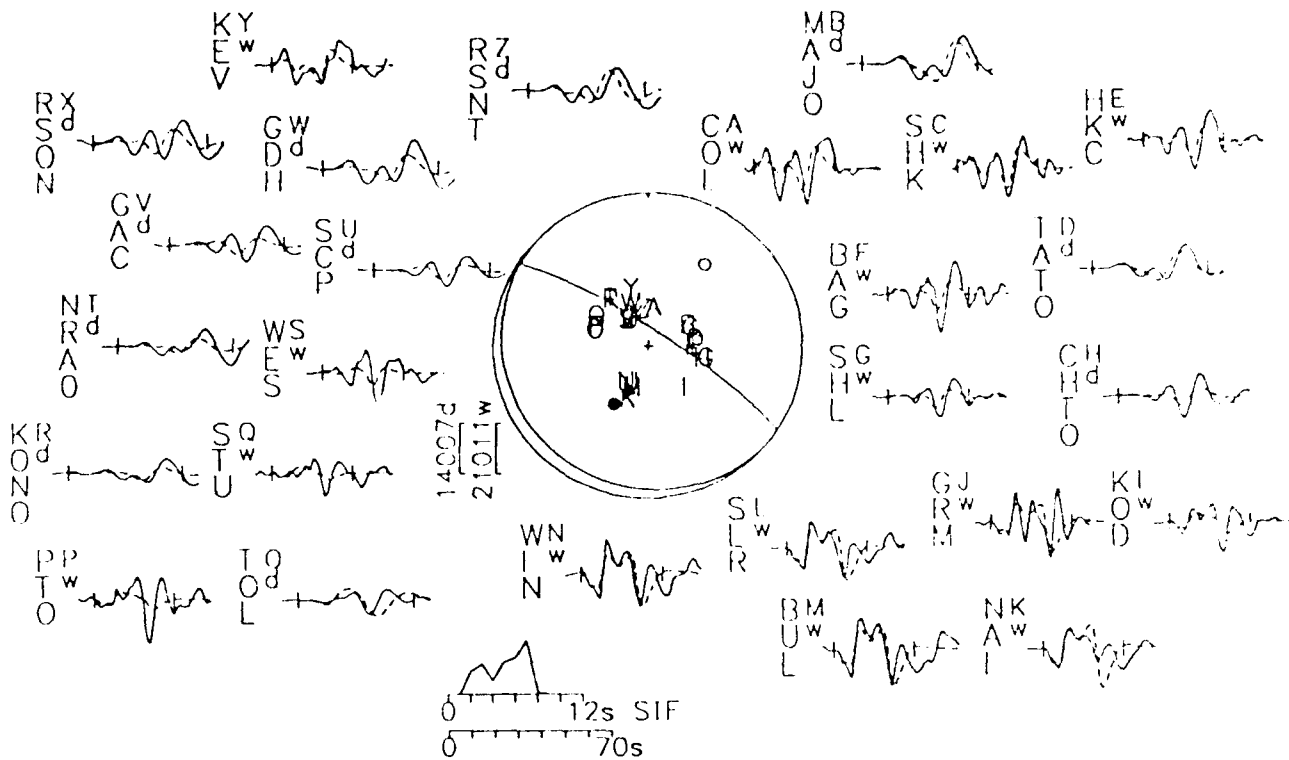
March 6, 1986
1:299/88/275/31/2.523E18
2:114/63/87/13/2.177E18

FIGURE 27b

100

FIGURE 28

SHL-P KOD-P SRL-P PTO-P STU-P KOD-S WIN-S

101
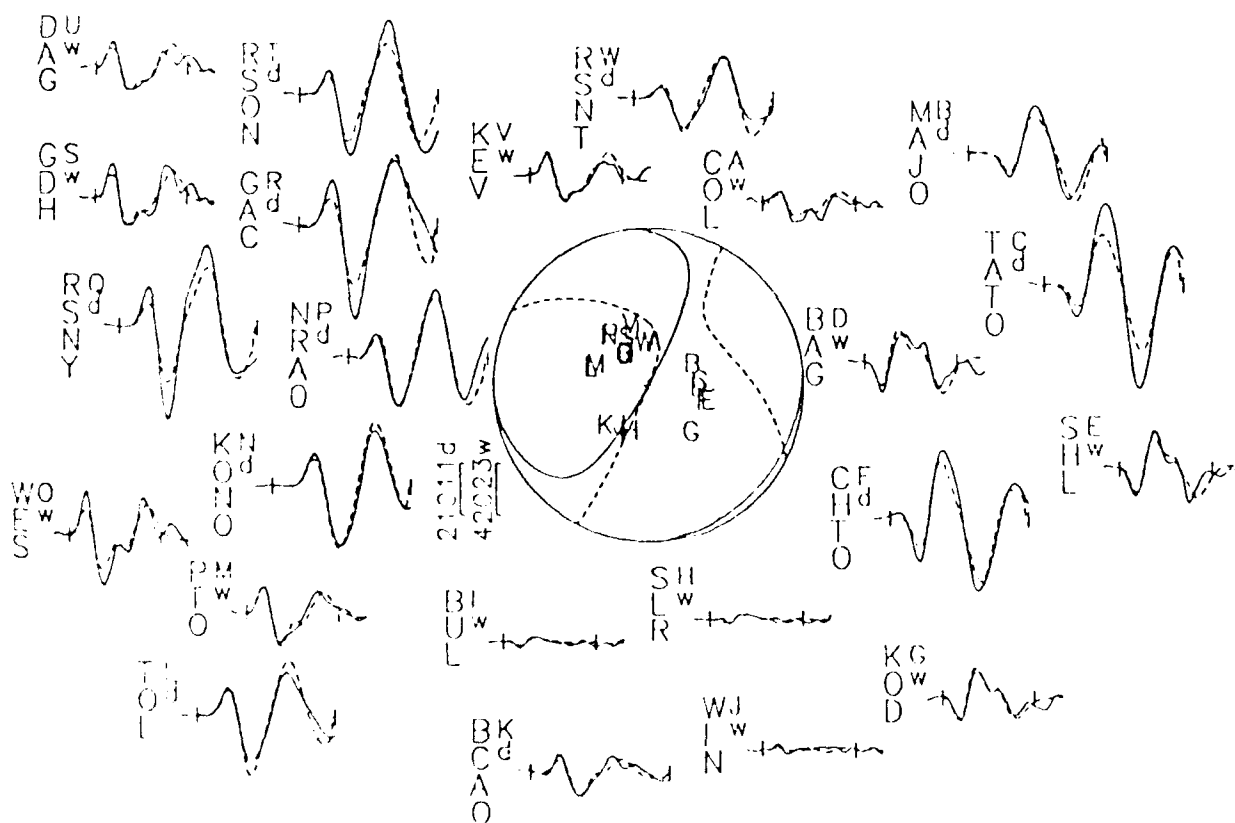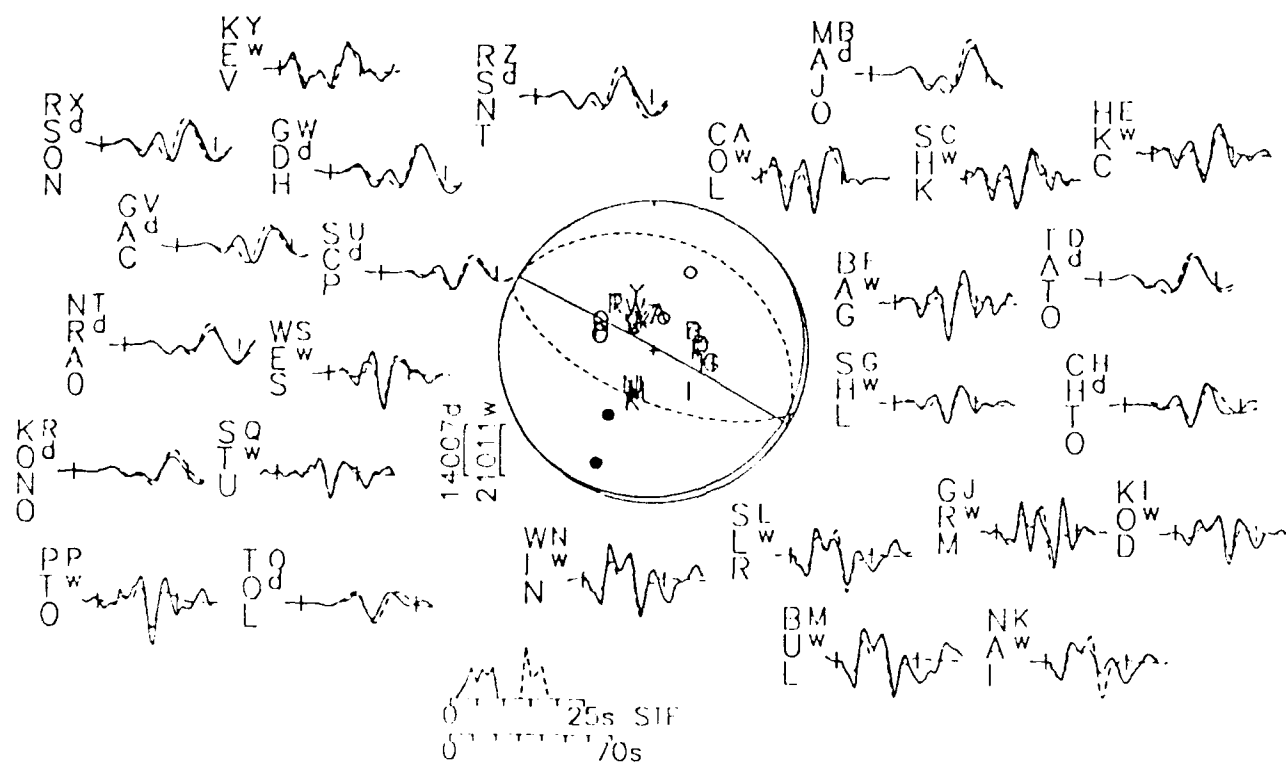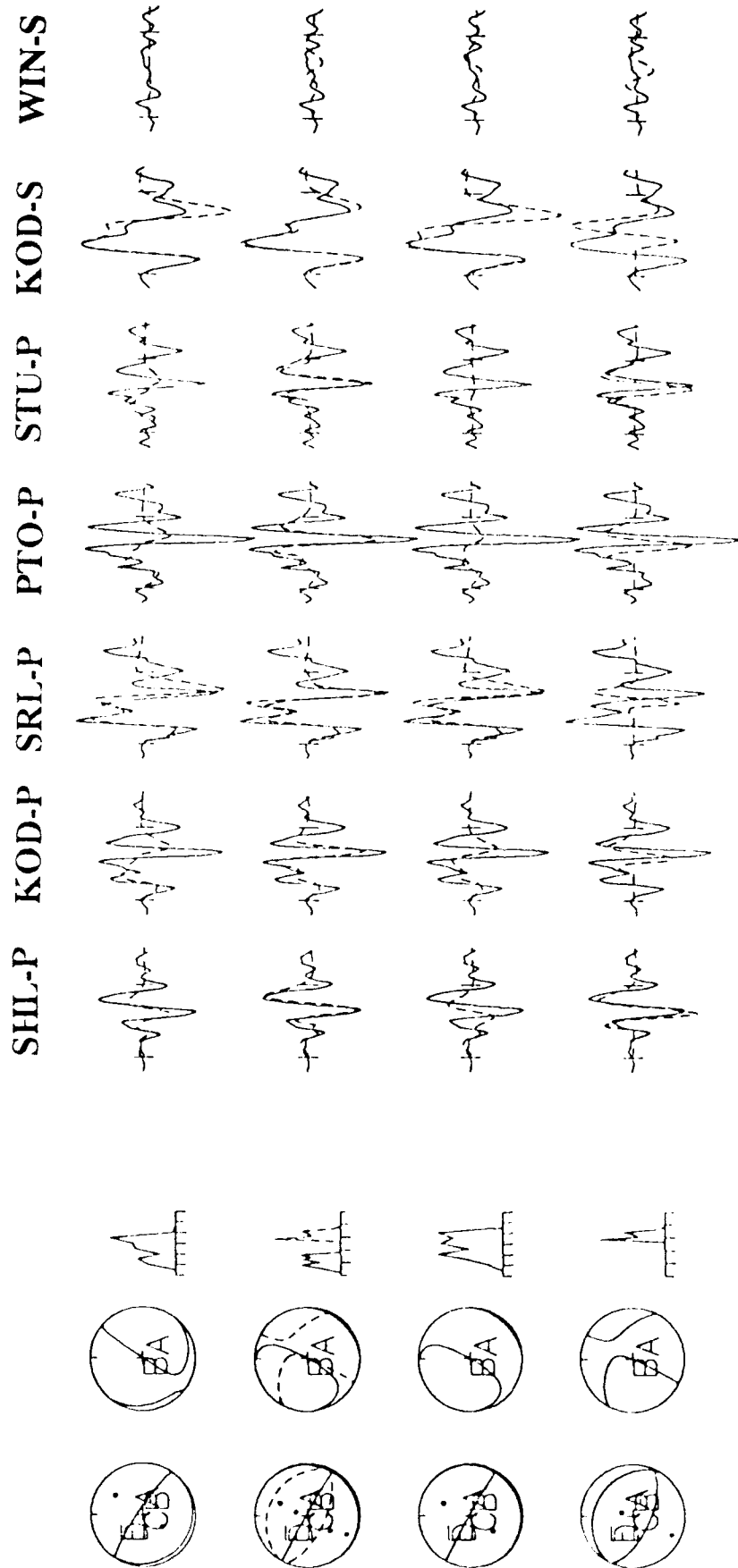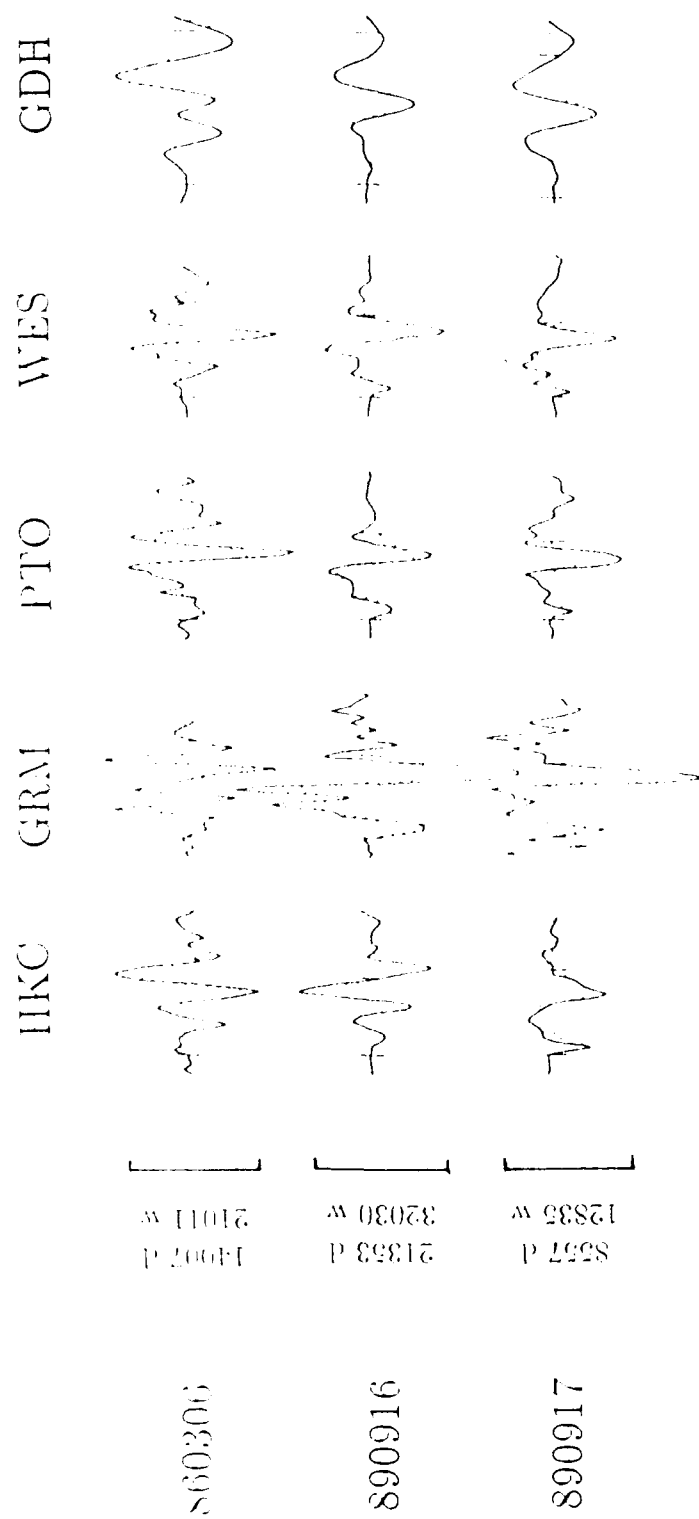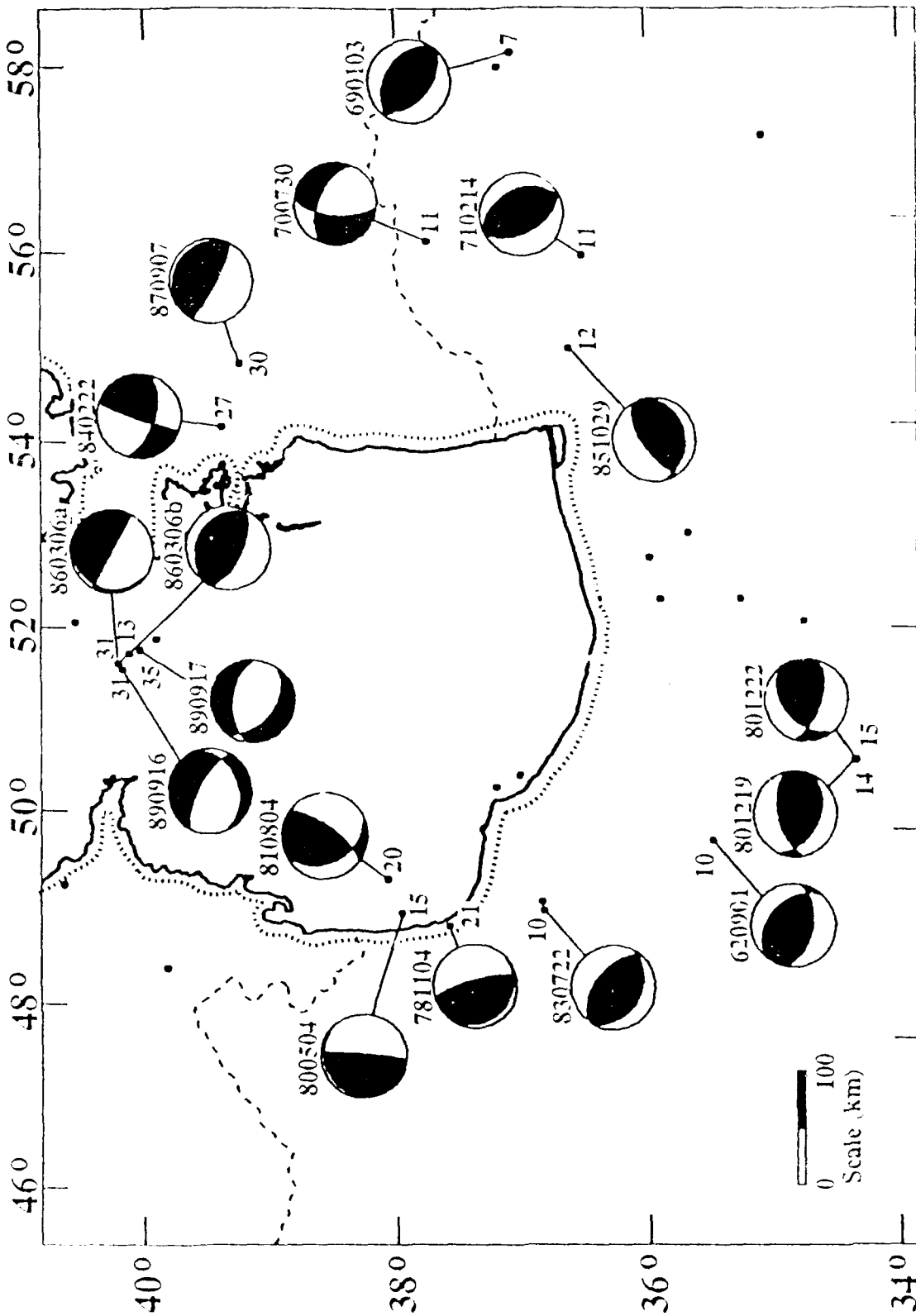
FIGURE 29

FIGURE 30a

FIGURE 30b

104
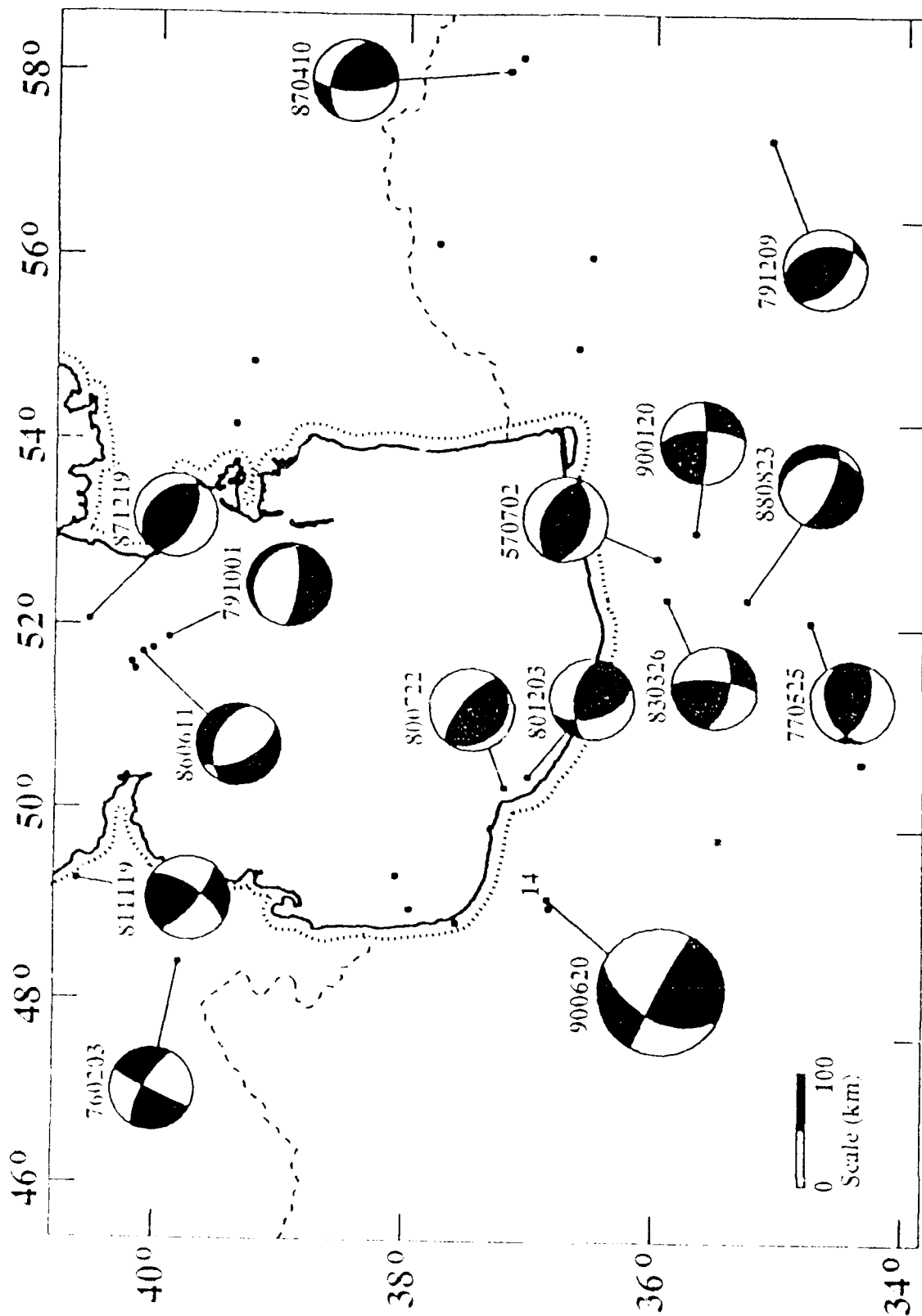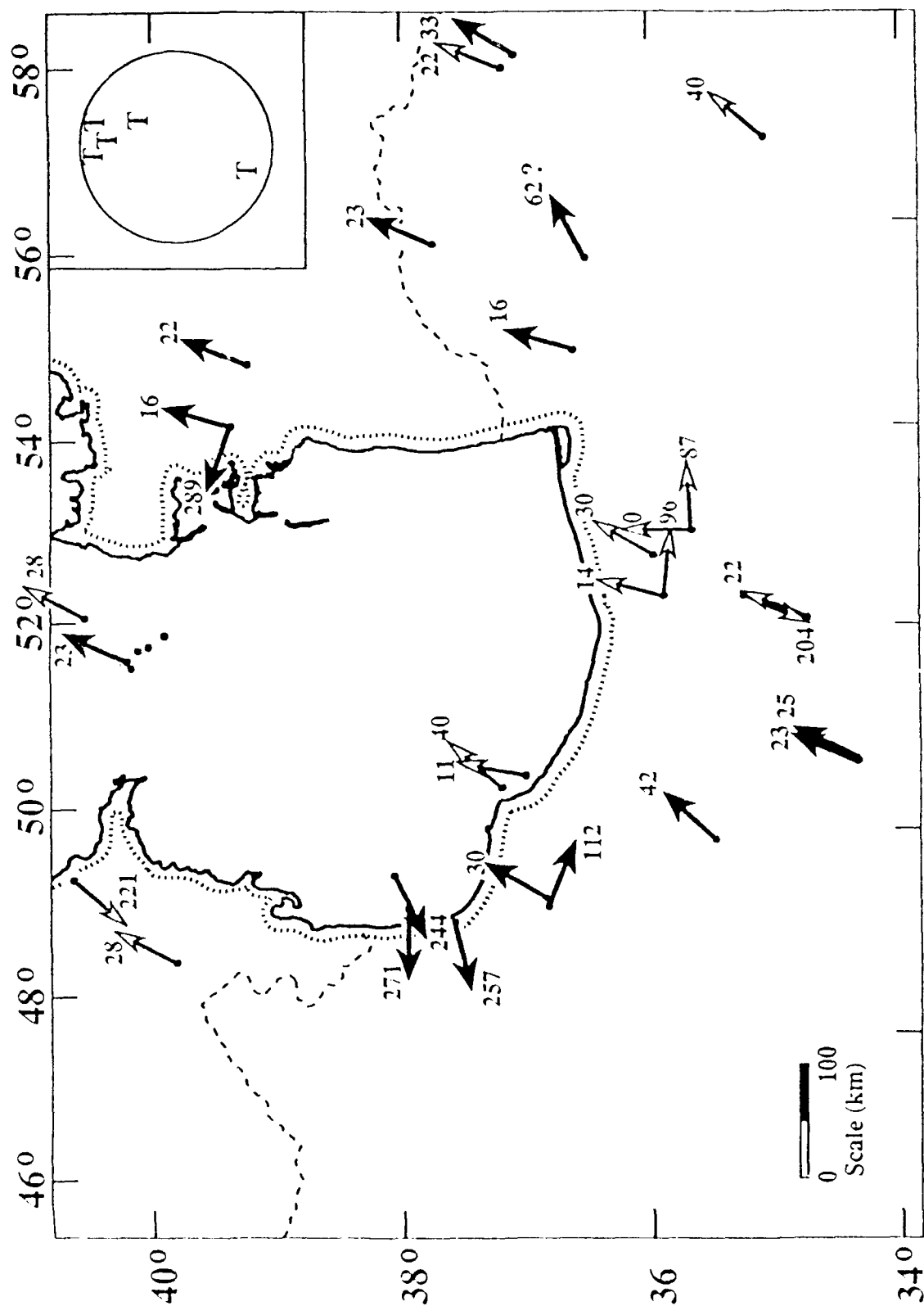
FIGURE 31

APPENDIX

In this appendix we show the observed seismograms for the events not discussed in detail in the main text, and compare them with synthetic seismograms computed for the minimum misfit inversion solution. For each one of these events we have conducted a series of tests identical to those shown in Figure 26 to place bounds on the strike, dip, slip, and centroid depth. Focal parameters for the minimum misfit solution from the inversion and bounds on these parameters from the test are given in Table 2. The format of each figure is the same as in Figure 24.

Figure A1. 1962 September 1 - The Buyin Zara earthquake (M_S 7.2, m_b 6.9) devastated the area south of Qazvin in northern Iran, killing around 12,200 people. Faulting was discontinuous, but was observed in a zone striking $103°$ over a distance of about 80 km (Ambraseys 1962; Ambraseys & Melville 1982). Displacements generally involved both thrusting on planes dipping south and also left-lateral strike slip. Fault segments typically had a strike of around $100°$. Average amplitudes were about 1.4 m vertical displacement and 0.6 m strike-slip.

Many of the seismograms of this earthquake were off-scale, and, because it occurred in the early days of the WWSSN, not many seismograms were available anyway. Those we were able to obtain are shown in Figure A1a. The coverage of the focal sphere is not very good, with most stations in the NW and only two in the SE. The first motions are better distributed (Fig. 23), and require a large reverse slip component. To obtain the minimum misfit solution, shown in Figure A1a, we used only three SH waveforms: at BAG, PMG, and STU. We gave the PMG SH waveform only half the weight it would normally have, because of its distance ($101°$), at which the ScS phase might be expected to interfere. We justified its retention because of its similarity to the SH waveform at BAG (distance $65°$, at which ScS does not interfere with S). We did not use the MDS SH waveform in the inversion because of its distance ($93°$), and because we had no independent check on the ScS contamination; it is shown because the polarity of its onset suggests an SH nodal plane between its position and that of STU on the focal sphere. By comparing the amplitude of the seismograms at BAG with those of other stations, we deduced that its gain was erroneously given as 1500 on the WWSSN film chip, and that it should have been 3000: the inversion was not sensitive to this change, which we have corrected.

The fit to observed waveforms in Figure A1a is reasonable, and demonstrates a long time function of about 24 seconds. At a rupture velocity of 3 kms^{-1} this can account for 72 km of faulting, which is compatible with what was observed (Ambraseys & Melville

1982). The moment of 3.68×10^{19} Nm (M_W 7.0) can account for 1.4 m of displacement on a fault 72 km long, extending to a depth of 10 km with a dip of $52°$. This amount, its sense (which is predominantly reverse with a smaller left-lateral component), and its strike, are also compatible with surface observations.

We were particularly interested in the slip vector of this earthquake, and so carried out tests on the resolution of the rake, which controls the strike of the auxiliary (north-dipping) plane, and hence slip vector. These tests are shown in Figure A1b.

The minimum misfit solution (rake = $70°$) is shown in row 2. In rows 1,3 and 4 the rake was fixed at some other value, and the other parameters were allowed to change in the inversion. The rake cannot have a value below $60°$ without producing the wrong polarity for SH at STU, thus limiting the maximum left-lateral component. The minimum left-lateral component is less well resolved: the SH fit at STU improves if the rake exceeds $70°$, and a value of $100°$ produces a better fit than the minimum misfit solution (row 4): but it requires a right-lateral component, which is incompatible with surface observations. The minimum misfit slip vector is $42°$, but we conclude it could have a value between $30°$ and $50°$ (corresponding to a rake of $70° - 10/ + 15°$). Note that there is some trade-off between strike and rake in this case. The dip, depth, and moment change little when the strike and rake are perturbed. We estimate the mechanism of this event to be: strike $101° \pm 10°$; dip $52° \pm 3°$; rake $70° - 10°/ + 15°$; depth 10 ± 4 km.

Figure A2. 1969 January 3 - P-wave first motion polarities (Fig. 23) require high angle reverse faulting, but cannot constrain the strike and rake well. Waveform inversion and testing constrain the focal depth to 7 ± 4 km. The SH waveforms at SHL, CHG, and NAI constrain the strike to $132° \pm 15°$, dip $50° \pm 5°$, and rake to $95° \pm 8°$.

Figure A3. 1970 July 30 - P-wave first motion polarities for this event were studied by Jackson and McKenzie (1984). They plotted first motions of this event with a mantle source velocity of V_p 8.1 kms^{-1} because they could not fit orthogonal nodal planes otherwise. We suspect that some of the polarities at European stations, which they gave as dilatational, are in fact, nodal. With these changes, the nodal planes for the minimum misfit solution are consistent with the first motion polarities plotted with the focal velocity of 6.8 kms^{-1}. We estimate the centroid depth to be 11 ± 4 km.

Figure A4. 1971 February 14 - P-wave first motions and P-wave waveform inversion require this event to result from high-angle reverse faulting. First motion data suggest a nodal

plane roughly as shown. P-waveforms constrain the centroid depth to 11 ± 5 km but do not greatly aid in constraining other focal parameters, particularly strike and slip vector azimuth. No suitable SH waveforms were available for this event.

Figure A5. 1980 May 4 - First motion polarities require this event to have one almost vertical nodal plane and this is confirmed by the waveform inversion. Inversion and testing constrain the centroid depth to 15 ± 5 km, the strike to $28^\circ \pm 10^\circ$, the dip to $7^\circ \pm 10^\circ$, and the rake to $297^\circ \pm 15^\circ$.

Figure A6. 1980 December 19 - First motion P-wave polarities require high angle reverse faulting, but do not constrain the strike and rake well. Waveform inversion and testing constrain the centroid depth to 14 ± 8 km, the strike to $115^\circ \pm 20^\circ$, the dip to $41^\circ \pm 8^\circ$, and the rake to $120^\circ \pm 15^\circ$.

Figure A7. 1980 December 22 - First motion P-wave polarities require high angle reverse faulting, but do not constrain the strike and rake well. Waveform inversion and testing constrain the centroid depth to 15 ± 5 km, the strike to $113^\circ \pm 20^\circ$, the dip to $56^\circ \pm 8^\circ$, and the rake to $125^\circ \pm 15^\circ$. The first motion at NAI is incompatible with the planes as shown (Fig. 23) but lies very close to a nodal plane and within the acceptable error in its dip.

Figure A8. 1981 August 4 - First motion data constrain the steeply dipping plane (Fig. 23). Two first motion polarities (JER, IST) are inconsistent with the minimum misfit solution (strike $154^\circ \pm 15^\circ$, dip $35^\circ \pm 15^\circ$, rake $32^\circ \pm 20^\circ$). Both are near a nodal plane and are at regional distances, so that their precise position on the focal sphere is uncertain. For comparison with our results, the Harvard CMT solution gives strike 159°, dip 26°, rake 40°, and centroid depth of 25 km for this event, which is within the uncertainty bounds, identical to our solution.

Figure A9. 1983 July 22 - This event occurred one minute prior to the 1983 Coalinga earthquake (M_W 5.75) in California, whose seismograms caused interference at some stations. We chose seismograms from stations where the Coalinga P- or SH- phases do not arrive within the inversion window. P-wave first motion polarities (Fig. 23) require high angle reverse faulting, but do not constrain the strike and rake well. Waveform inversion constrains the strike to $120^\circ \pm 20^\circ$, the dip to $35^\circ \pm 8^\circ$, and the rake to $82^\circ \pm 15^\circ$. The nodal planes shown in Figure 23 are for the minimum misfit solution and violate the first

motion data for JER and IST. Both of these stations are at regional distances and their precise position on the focal sphere is uncertain.

Figure A10. 1984 February 22 - We could not read any reliable first motion polarities for this event. Only a limited number of P-waveforms are available and all but one of these are from the GDSN. The mechanism (strike $106° \pm 20°$, dip $60° \pm 10°$, rake $174° \pm 20°$) is primarily constrained by the SH-waveforms. The depth is $27 \pm 4km$. The Harvard CMT solution is: strike $109°$; dip $83°$; rake $175°$, and centroid depth 40 km. Except for the depth, this is indistinguishable from our waveform inversion solution.

Figure A11. 1985 October 29 - First motion polarities (Fig. 23) require this event to have a relatively steep nodal plane dipping NW. The source orientation (strike $106° \pm 15°$, dip $30° \pm 10°$, rake $126° \pm 10°$) is well constrained by the abundant P- and SH-waveforms. The depth is $13 \pm 5km$. The Harvard CMT solution for 1985.10.29 is strike $97°$, dip $31°$, rake $72°$, and centroid depth 15 km. The strike and dip of the CMT solution is indistinguishable from our waveform inversion solution; however, the rake is significantly different. We are more confident in our waveform inversion results.

Figure A12. 1987 September 7 - First motion polarities constrain a WNW striking, steeply dipping nodal plane. Waveform inversion and testing constrain the centroid depth to 30 ± 8 km, the strike to $305° \pm 10°$, dip $10° \pm 10°$, and rake $103° \pm 20°$. The Harvard CMT solution for 1987.09.07 is strike $312°$, dip $14°$, rake $106°$, and centroid depth 29 km, indistinguishable from our waveform inversion solution.

Figure A13. 1989 September 16 - First motion polarities imply normal faulting for this event but poorly constrain the mechanism. Waveform inversion for a single source gives a mechanism involving either faulting on a WNW striking, steeply-dipping plane, or on a ENE striking, shallow-dipping plane. Because of the similarity of the waveforms of this event and 1986.03.06 (Fig. 29), we also inverted waveforms of this event for a second, delayed source. This cannot be as definitive as in the case of 1986.03.06 because the GDSN instrument response tends to blur source details and because of the lack of WWSSN stations which have a higher frequency response. The inversion with a second source produced marginally better fit to the waveforms than the single source solution, and gave a moment for the second source that was approximately 10% of the moment of the first event. Our preferred single source solution from the waveform inversion is strike $80° \pm 15°$,

dip 26° ± 5°, rake 225° ± 15° and depth 31 ± 10km. For comparison, the Harvard CMT solution is strike 104°, dip 36°, rake 228°, and centroid depth 34 km. The strike and dip of the CMT solution is slightly different from our waveform inversion solution, which we have more confidence in.

Figure A14. 1989 17 September - Waveforms of this event are similar those of to the 1989.09.16 earthquake. First motion polarities imply normal faulting but poorly constrain the orientation. Waveform inversion for a single source yields a mechanism that corresponds either to faulting on a WNW striking, steeply dipping plane, or on a ENE striking, shallow dipping plane. Figure 29 compares P-waveforms of this event and the 1986.03.06 and 1989.09.16 earthquakes at common stations. Because of the scarcity of WWSSN seismograms, we have only inverted this event assuming a single source. The resulting orientation is strike 128° ± 15°, dip 44° ± 5°, and rake 295° ± 15° and depth 35 ± 10km. The Harvard CMT solution for 1989.09.17 is strike 142°, dip 58°, rake 287°, and centroid depth 34 km. The dip of the CMT solution is different from our waveform inversion solution, however, we are more confident in our result.

1 September, 1962
$101/52/70/10/3.68 \times 10^{19}$
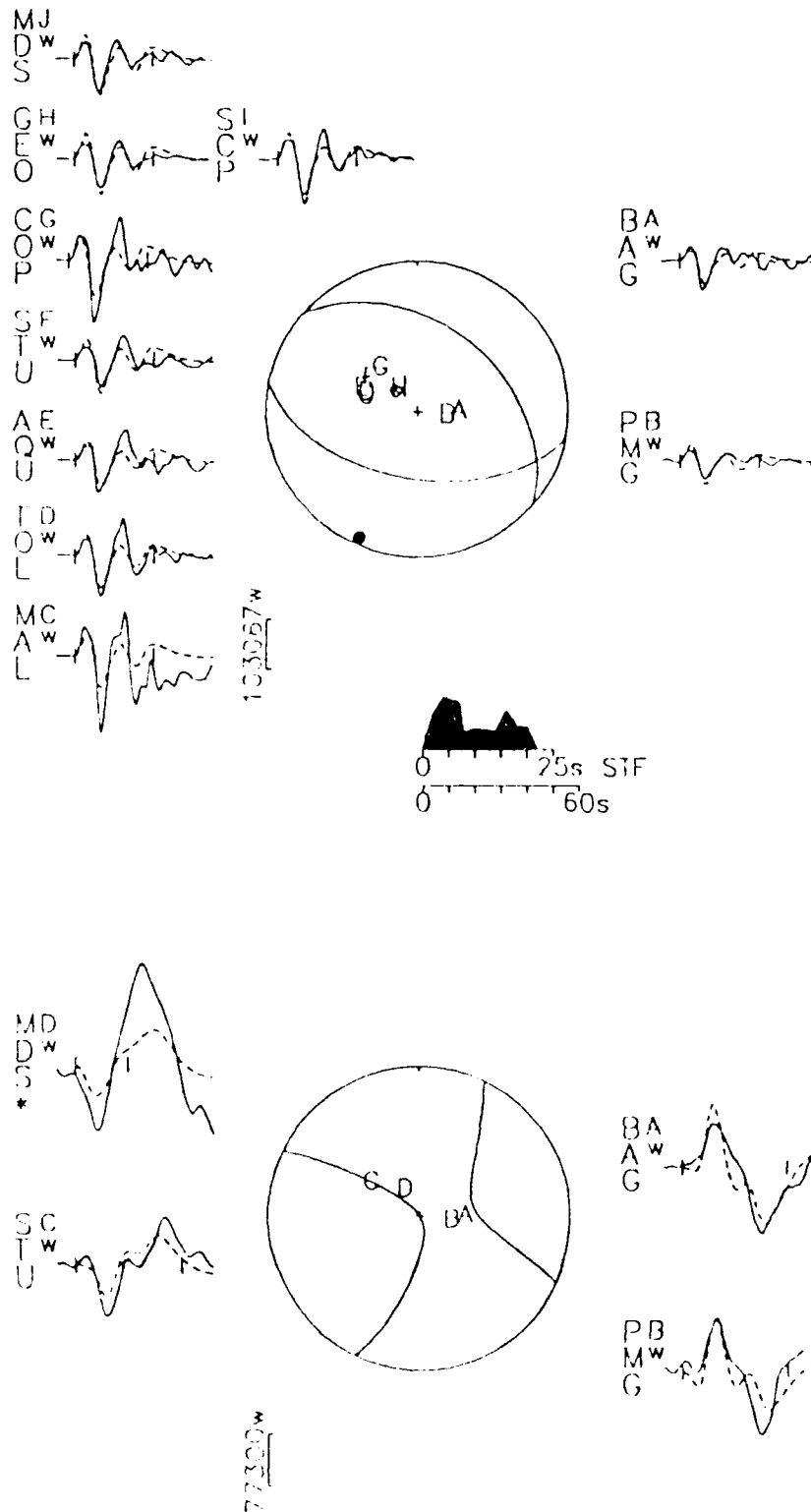
FIGURE A1a

FIGURE A1b

113
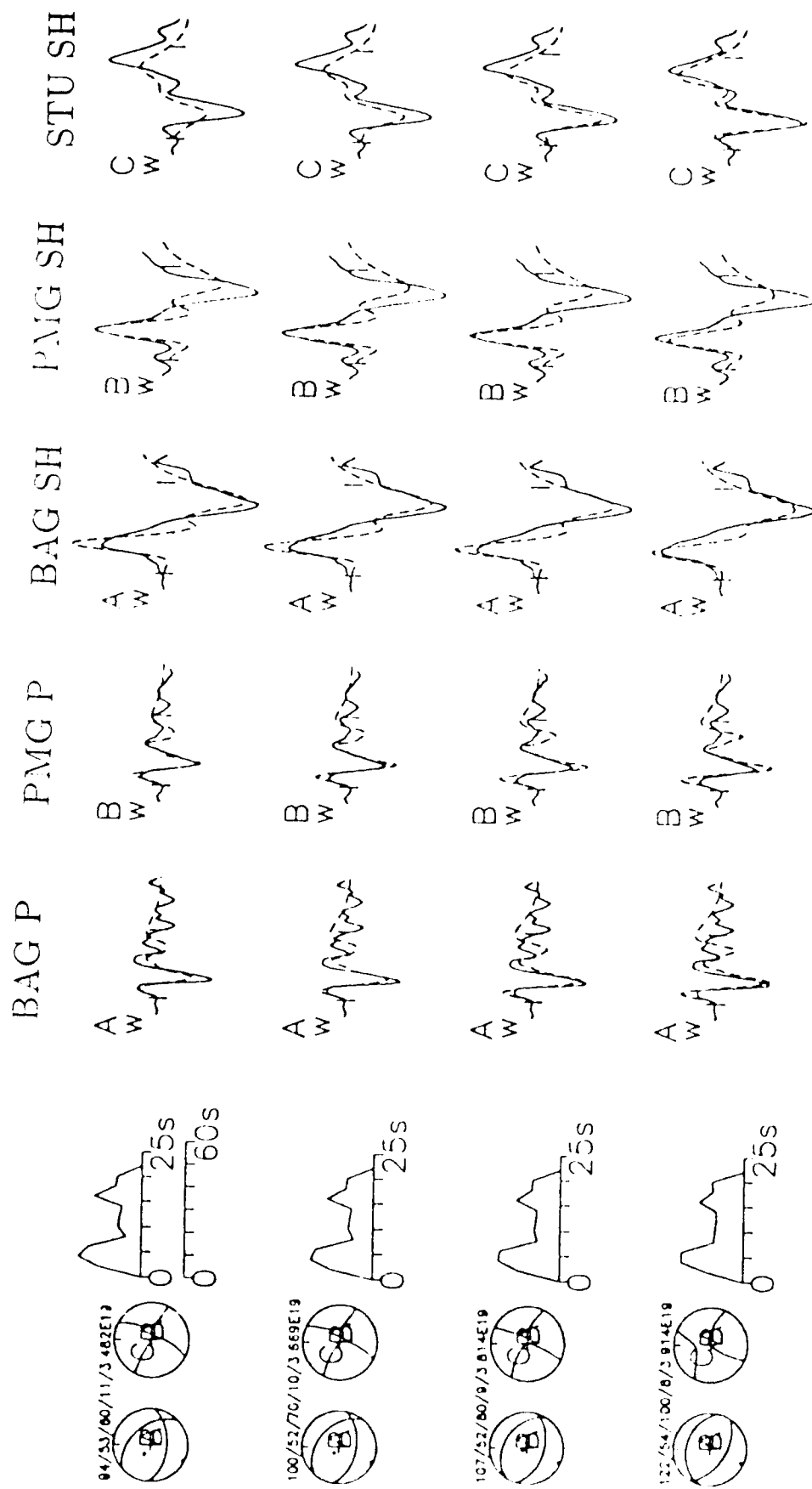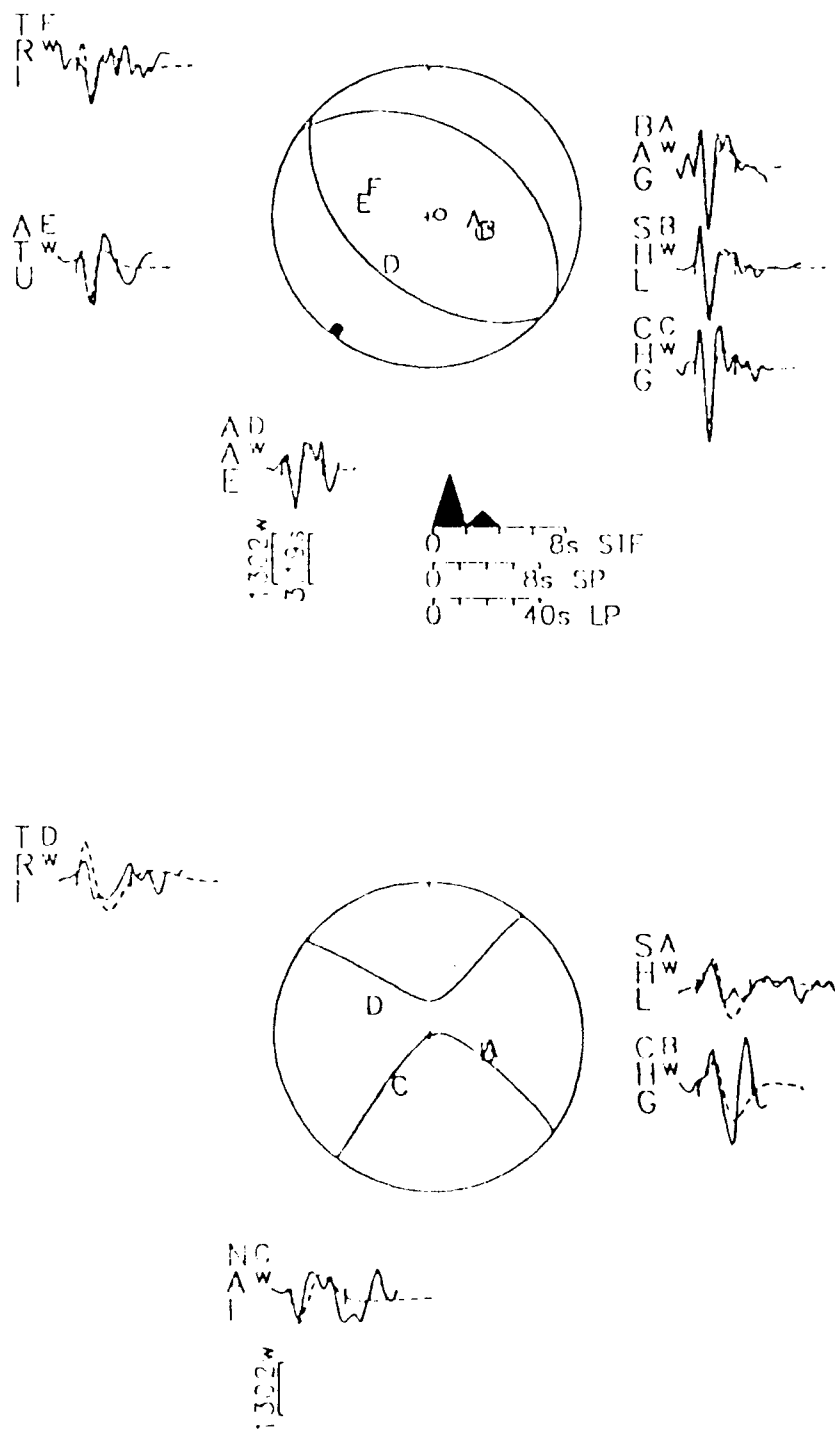
FIGURE A2

30 July, 1970
$293/56/210/11/4.29 \times 10^{18}$
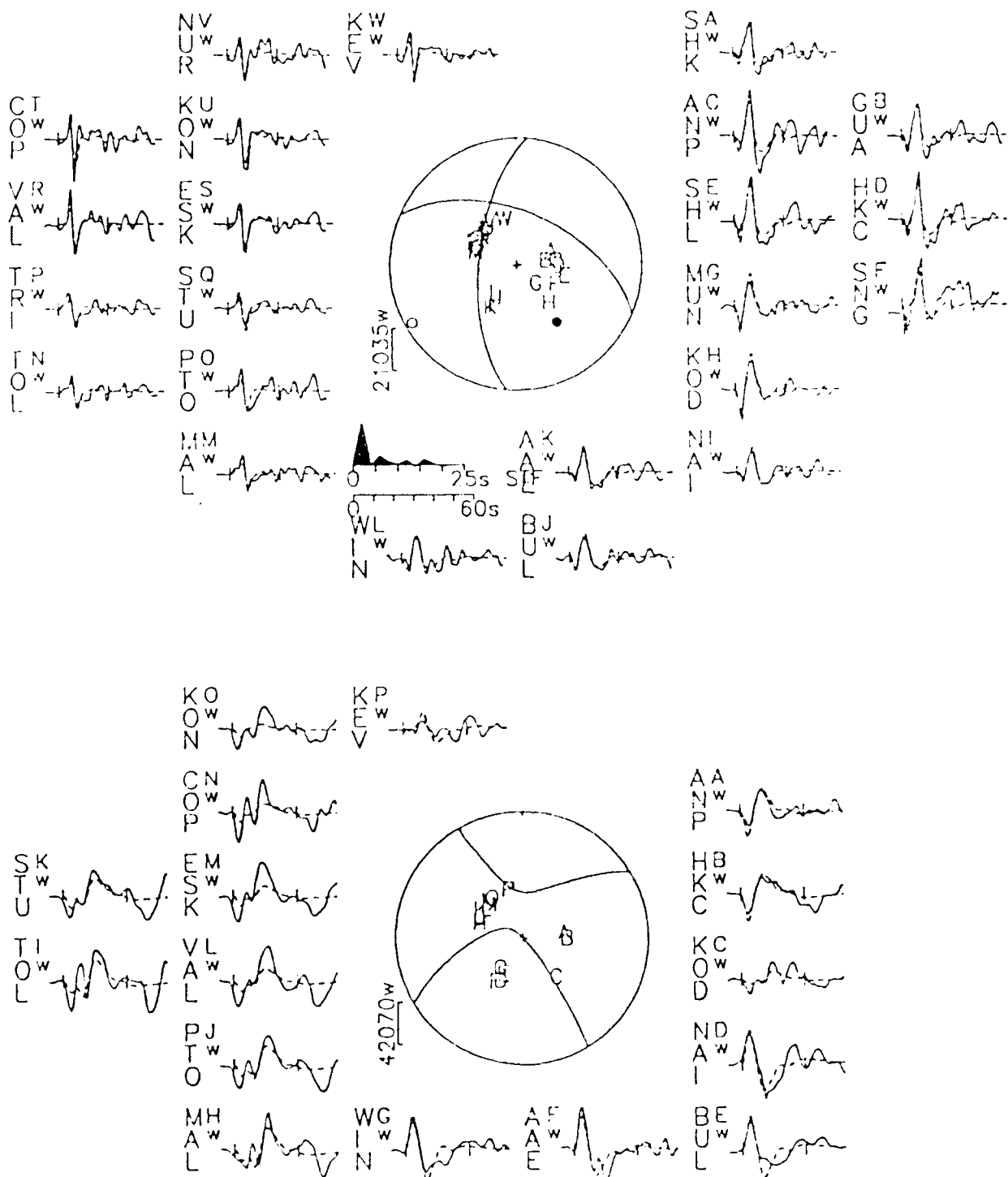
FIGURE A3

14 February, 1971

$336/39/93/11/4.05 \times 10^{17}$
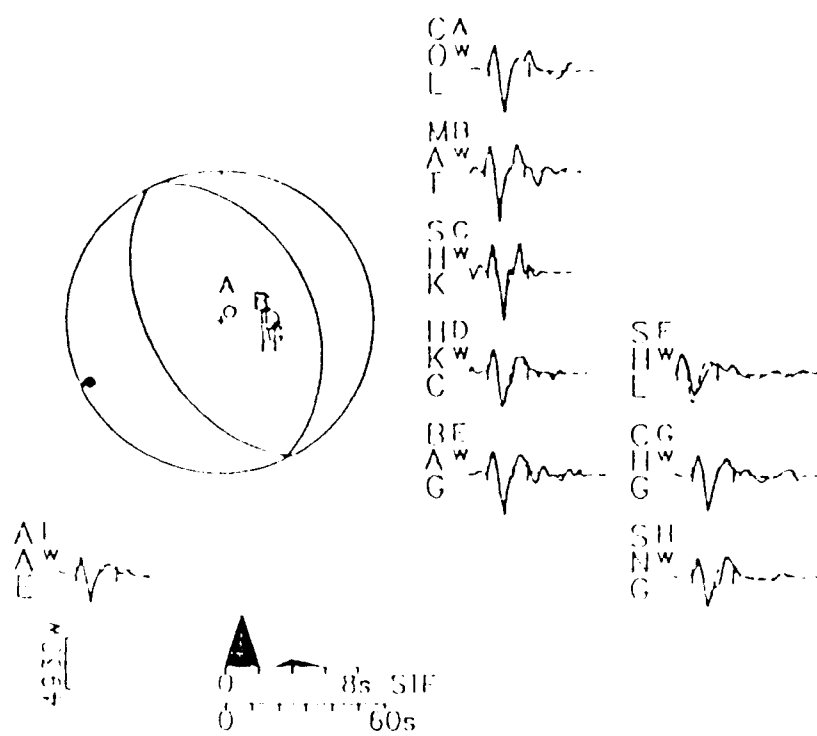
FIGURE A4

4 May, 1980
$181/84/267/15/4.02 \times 10^{18}$
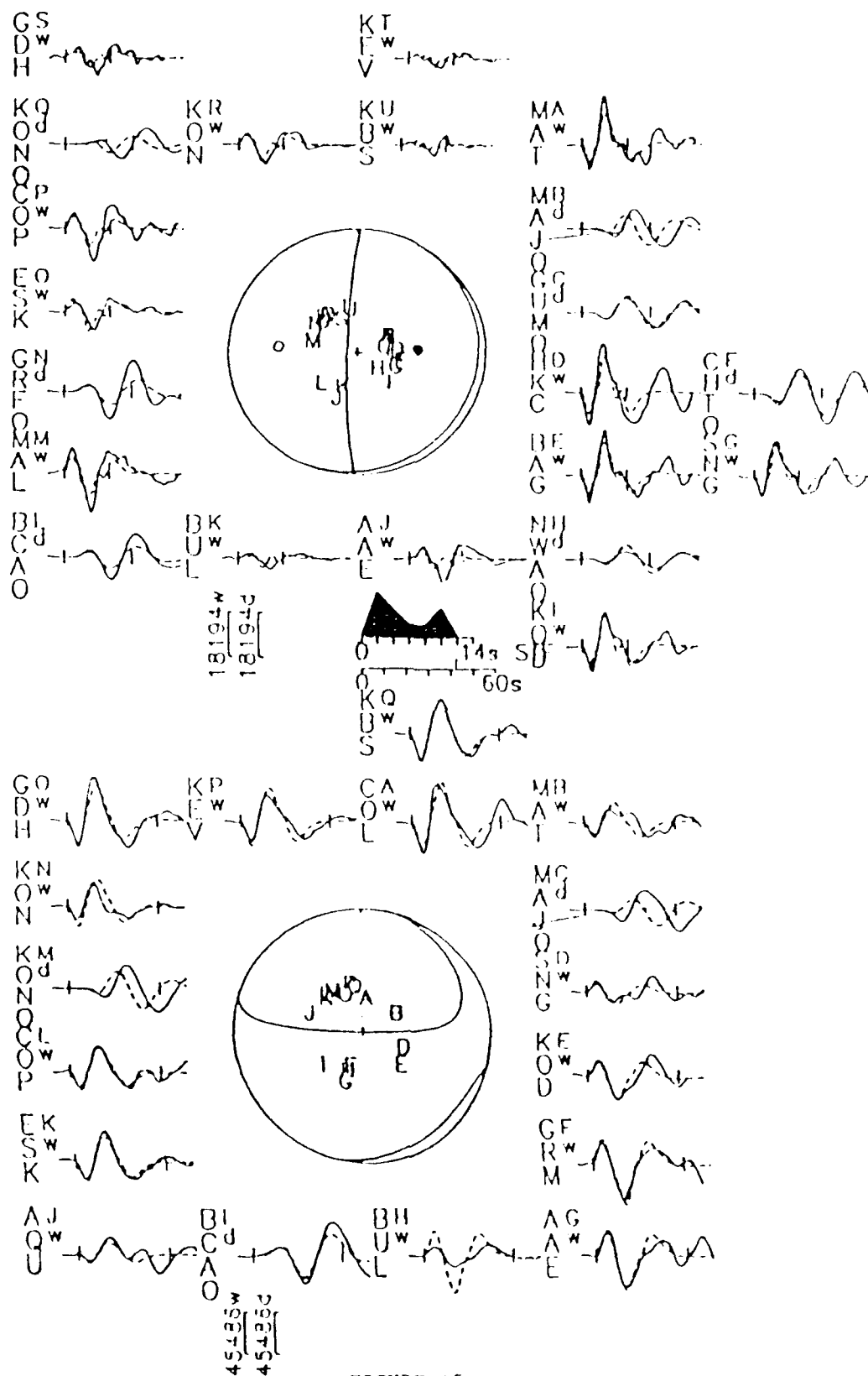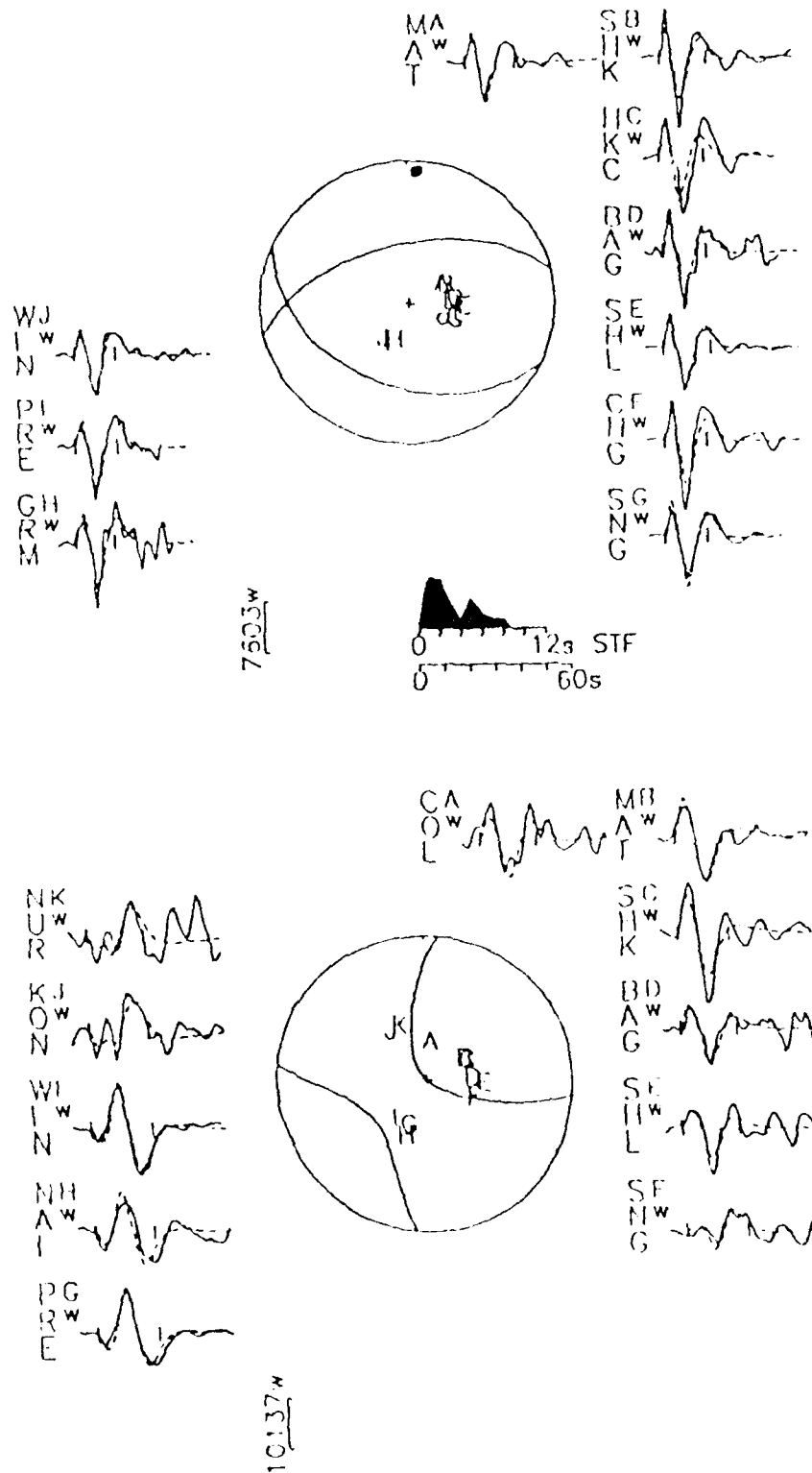
FIGURE A5

19 December, 1980
$115/41/120/14/1.40 \times 10^{18}$

FIGURE A6

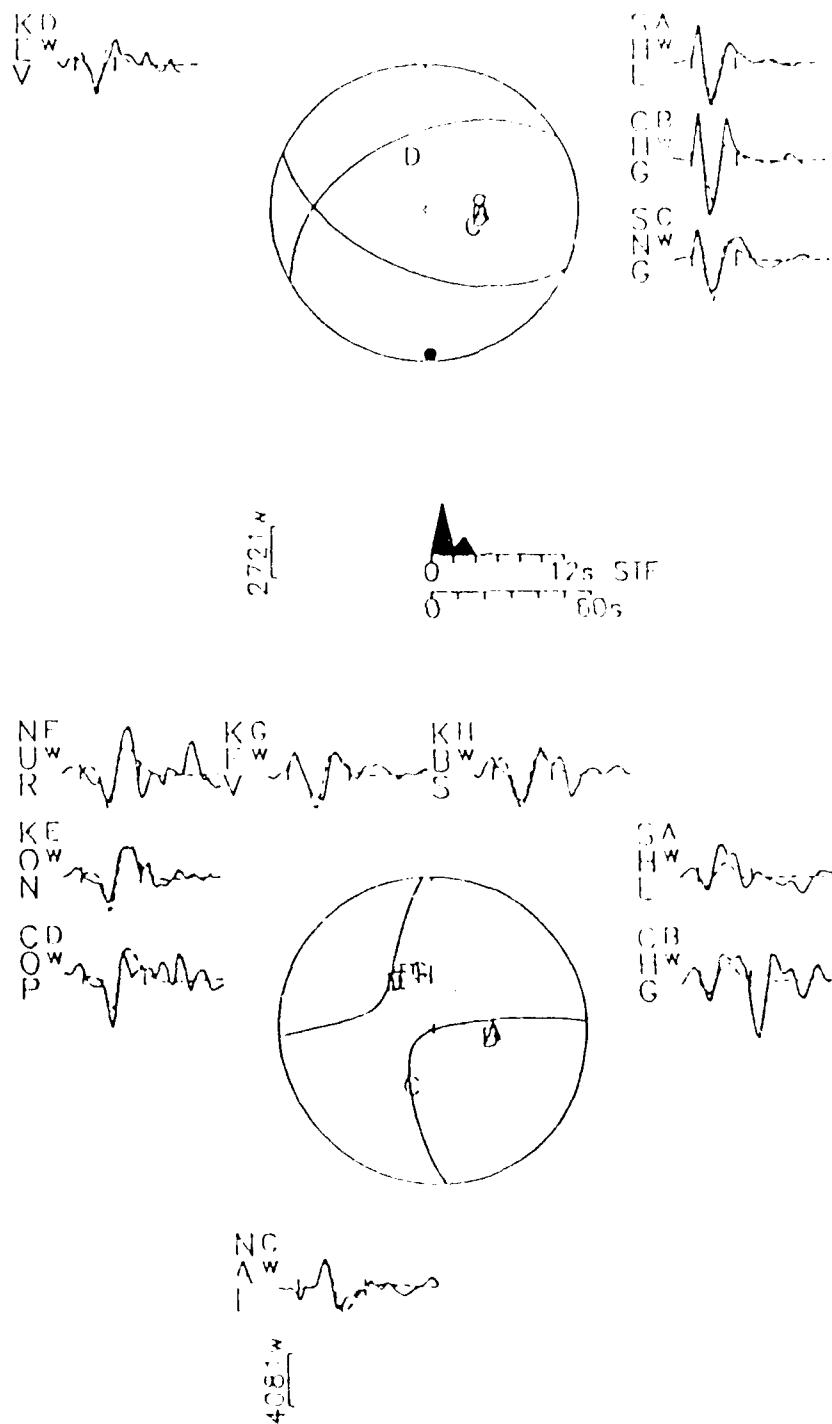## 22 December, 1980
$113/56/125/15/2.81 \times 10^{17}$

FIGURE A7

4 August, 1981
$154/35/32/20/2.38 \times 10^{17}$
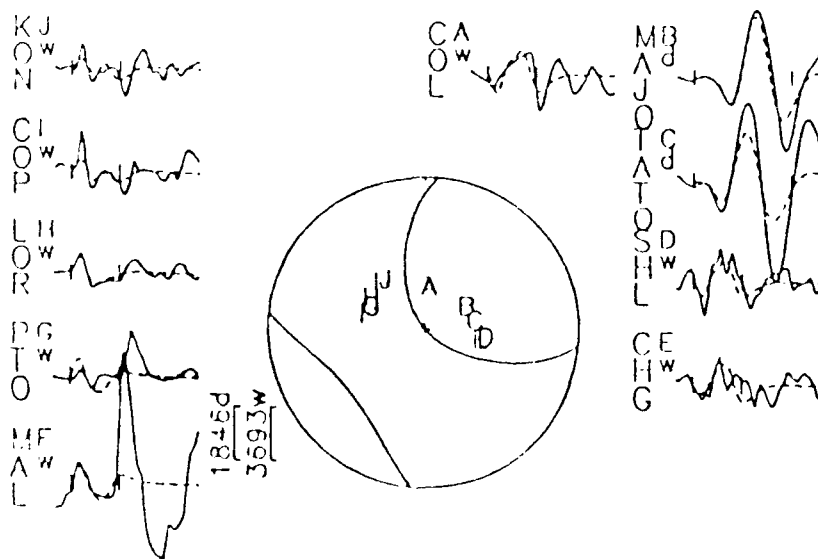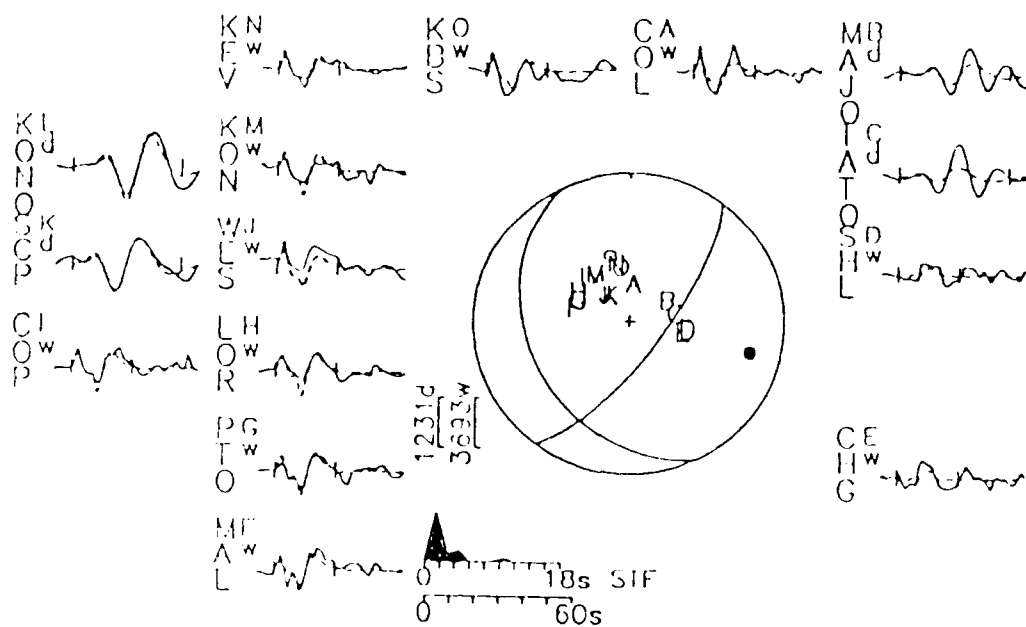
FIGURE A8

22 July, 1983
$120/35/83/10/1.88 \times 10^{17}$
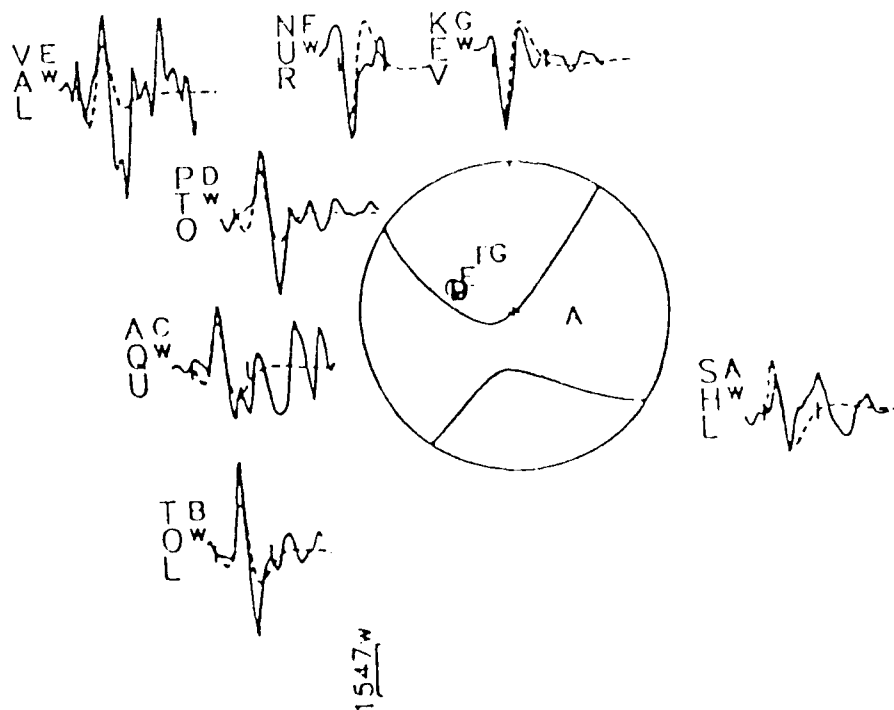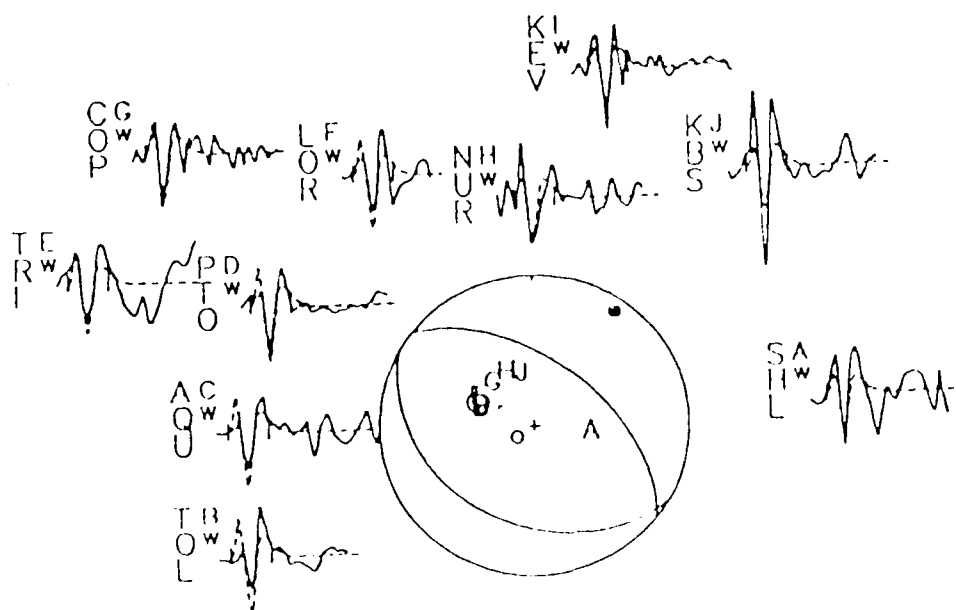
22 February, 1984
$106/60/174/27/5.10 \times 10^{17}$
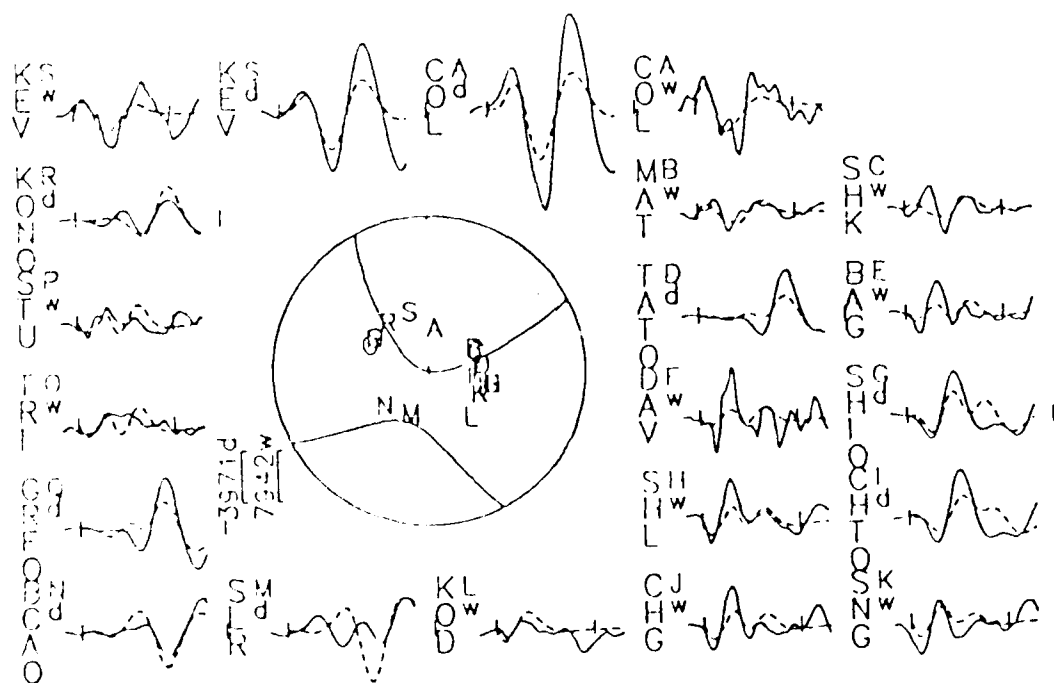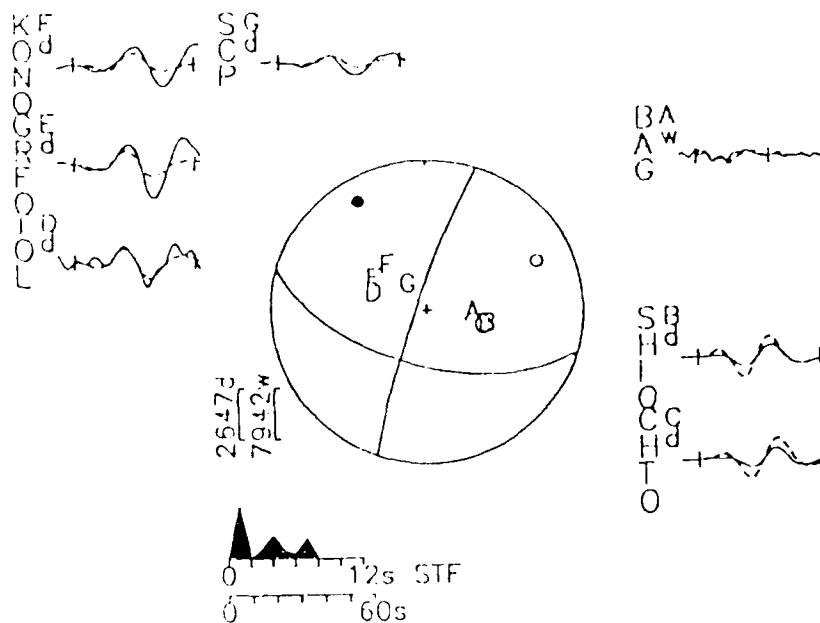
FIGURE A10

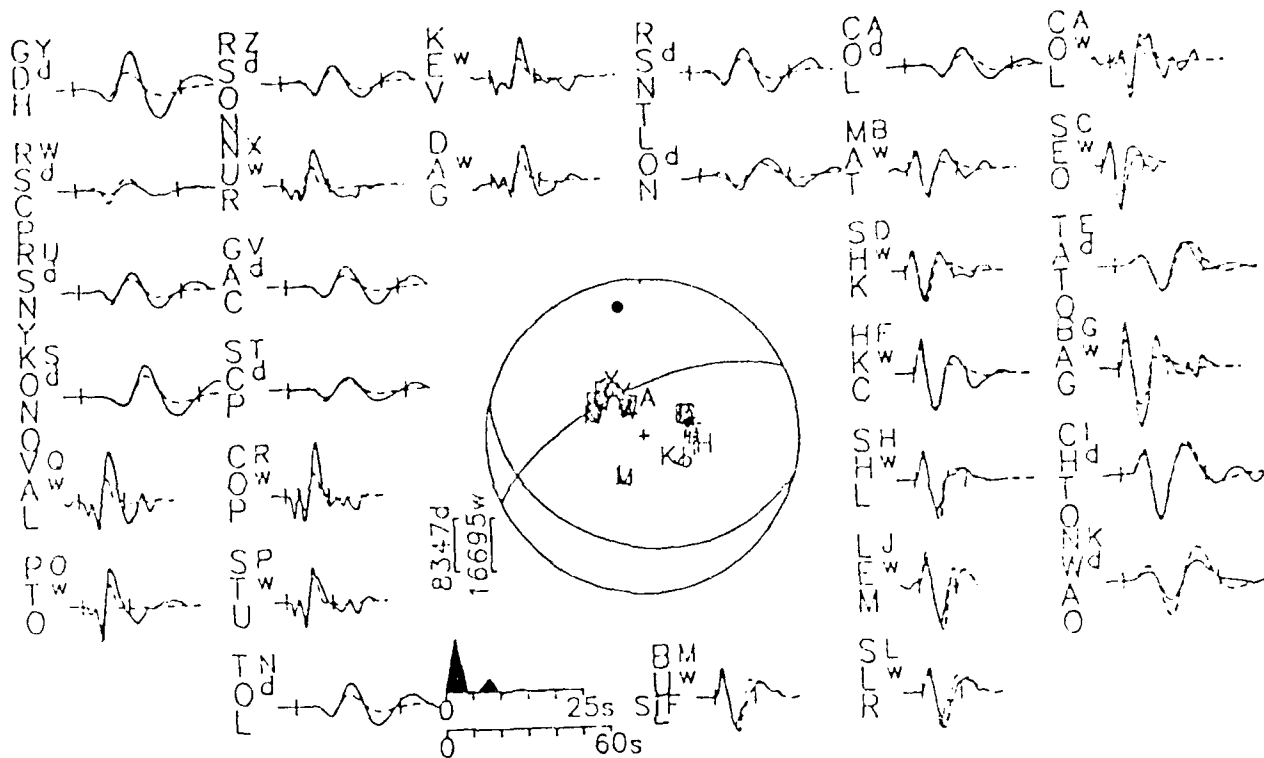# 29 October, 1985
$246/66/71/13/2.18 \times 10^{18}$
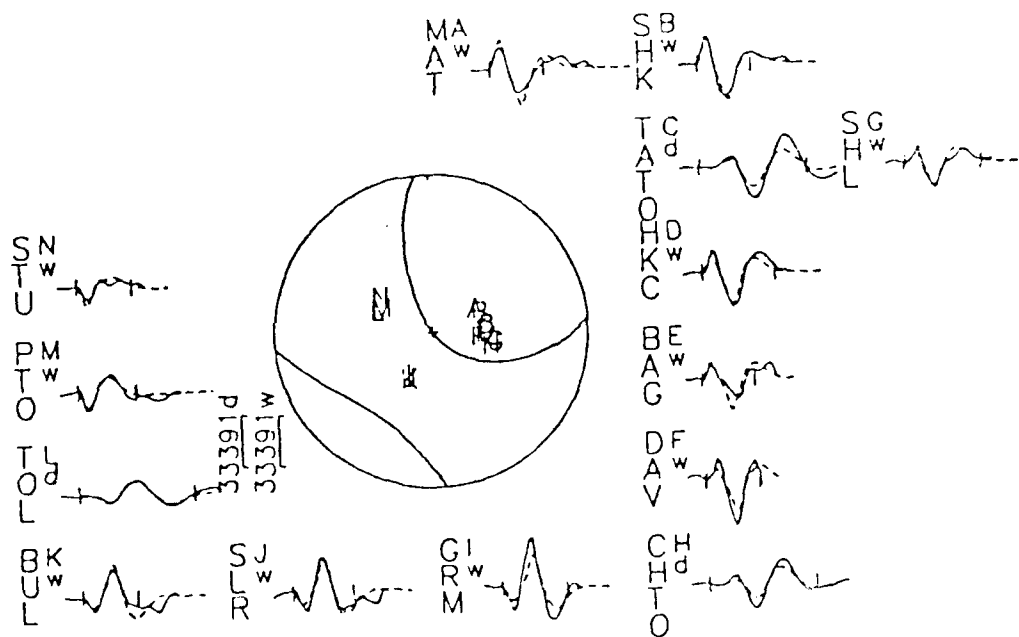
FIGURE A11
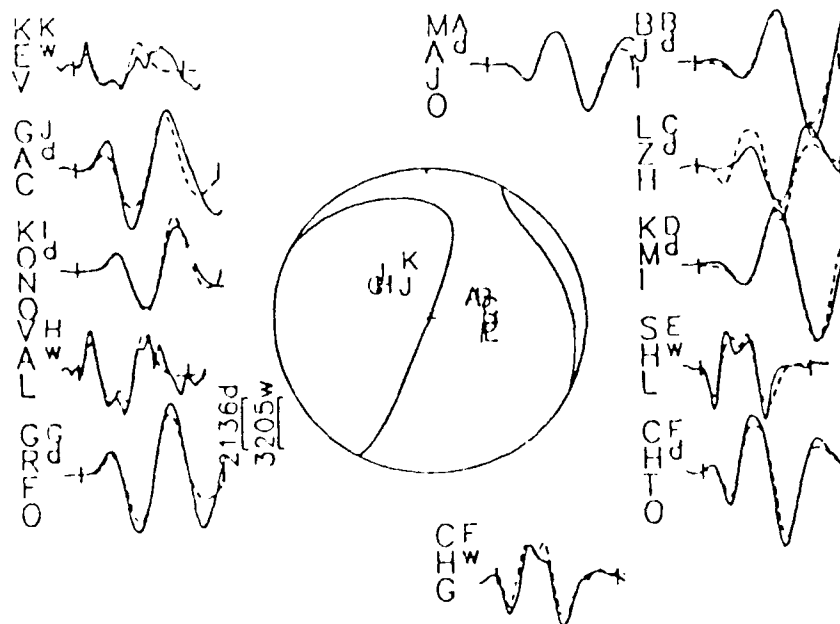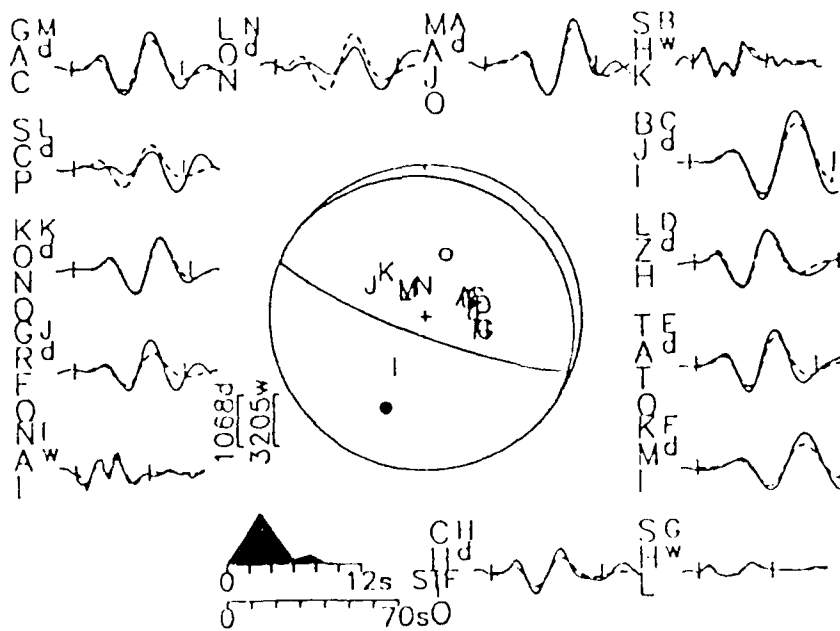
FIGURE A12

FIGURE A13

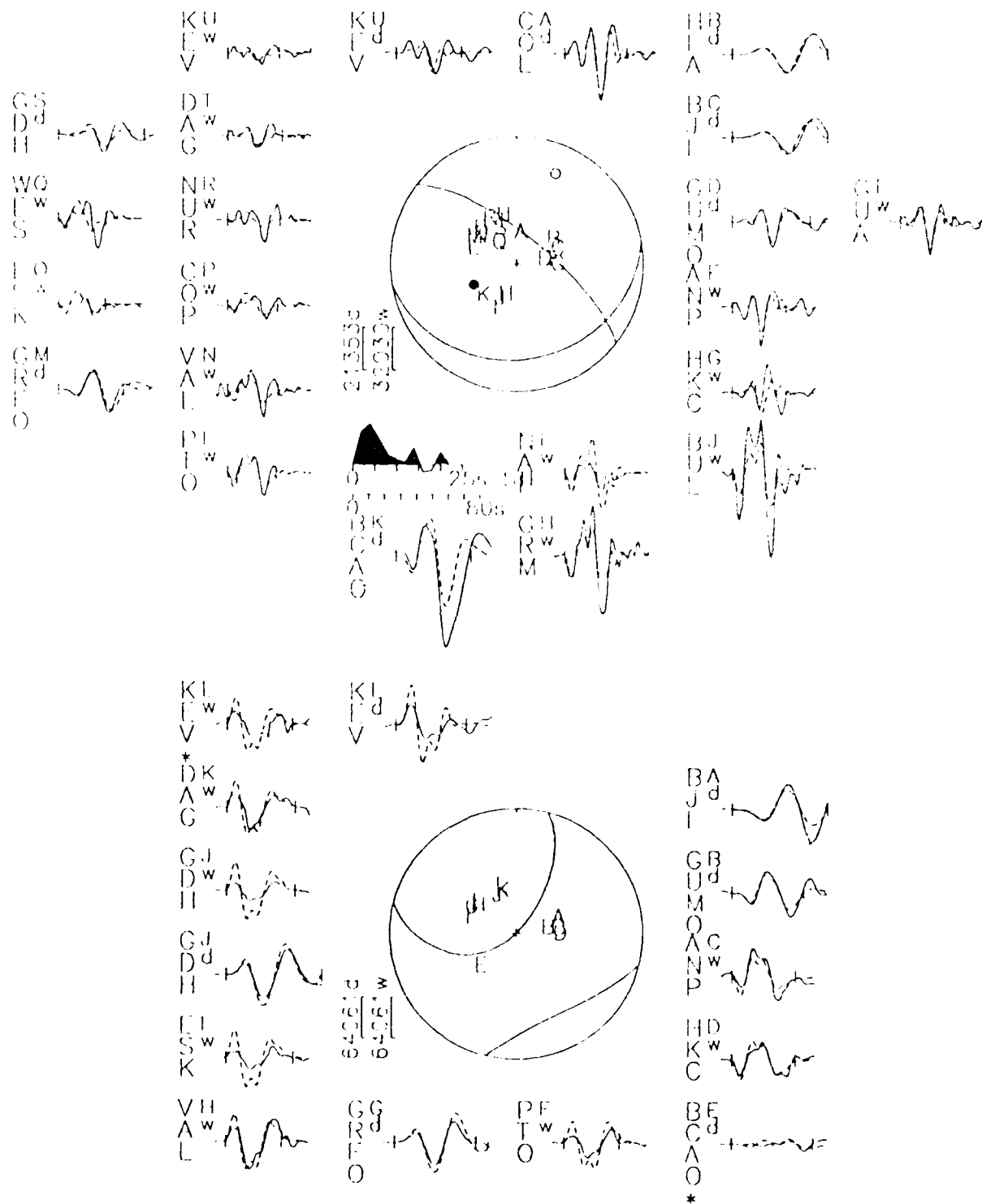# 17 September, 1989
$277/50/249/35/2.17 \times 10^{18}$
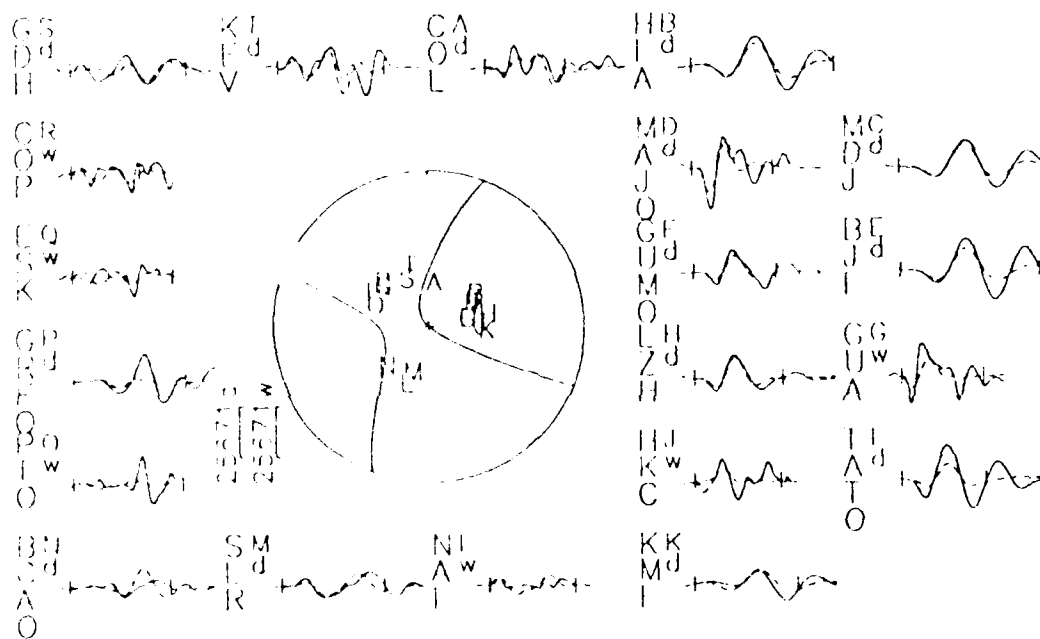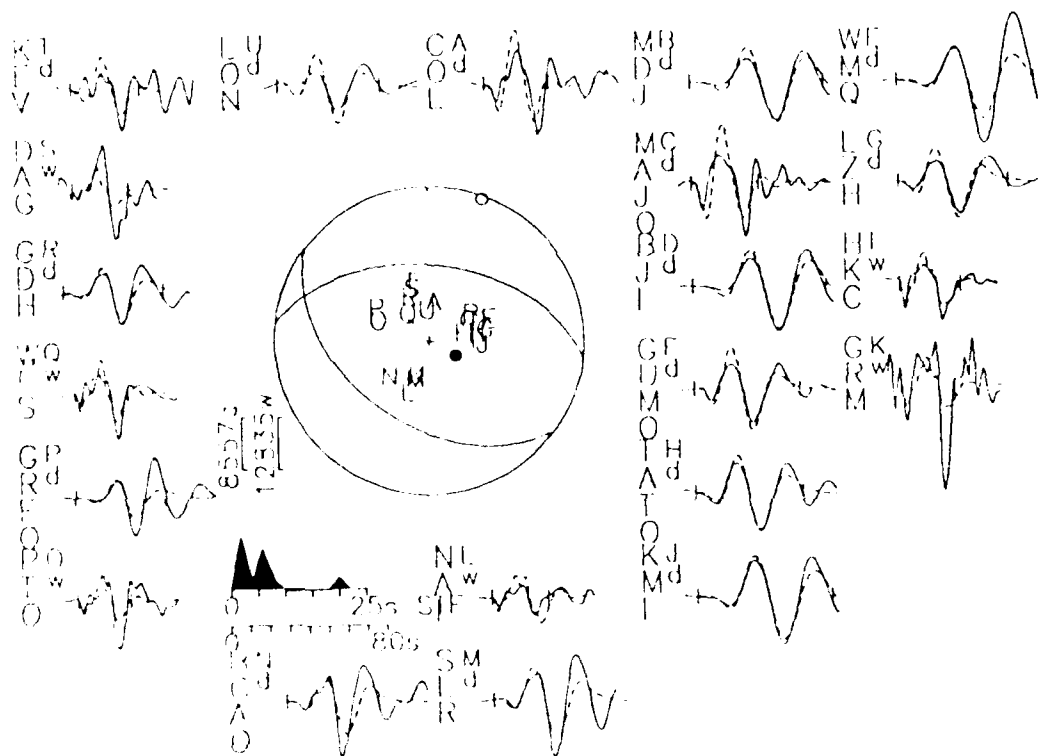

FIGURE A14

Prof. Thomas Ahrens
Seismological Lab, 252-21
Division of Geological & Planetary Sciences
California Institute of Technology
Pasadena, CA 91125

Prof. Keiiti Aki
Center for Earth Sciences
University of Southern California
University Park
Los Angeles, CA 90089-0741

Prof. Shelton Alexander
Geosciences Department
403 Deike Building
The Pennsylvania State University
University Park, PA 16802

Dr. Ralph Alewine, III
DARPA/NMRO
3701 North Fairfax Drive
Arlington, VA 22203-1714

Prof. Charles B. Archambeau
CIRES
University of Colorado
Boulder, CO 80309

Dr. Thomas C. Bache, Jr.
Science Applications Int'l Corp.
10260 Campus Point Drive
San Diego, CA 92121 (2 copies)

Prof. Muawia Barazangi
Institute for the Study of the Continent
Cornell University
Ithaca, NY 14853

Dr. Jeff Barker
Department of Geological Sciences
State University of New York
 at Binghamton
Vestal, NY 13901

Dr. Douglas R. Baumgardt
ENSCO, Inc
5400 Port Royal Road
Springfield, VA 22151-2388

Dr. Susan Beck
Department of Geosciences
Building #77
University of Arizona
Tuscon, AZ 85721

Dr. T.J. Bennett
S-CUBED
A Division of Maxwell Laboratories
11800 Sunrise Valley Drive, Suite 1212
Reston, VA 22091

Dr. Robert Blandford
AFTAC/TT, Center for Seismic Studies
1300 North 17th Street
Suite 1450
Arlington, VA 22209-2308

Dr. G.A. Bollinger
Department of Geological Sciences
Virginia Polytechnical Institute
21044 Derring Hall
Blacksburg, VA 24061

Dr. Stephen Bratt
Center for Seismic Studies
1300 North 17th Street
Suite 1450
Arlington, VA 22209-2308

Dr. Lawrence Burdick
Woodward-Clyde Consultants
566 El Dorado Street
Pasadena, CA 91109-3245

Dr. Robert Burridge
Schlumberger-Doll Research Center
Old Quarry Road
Ridgefield, CT 06877

Dr. Jerry Carter
Center for Seismic Studies
1300 North 17th Street
Suite 1450
Arlington, VA 22209-2308

Dr. Eric Chael
Division 9241
Sandia Laboratory
Albuquerque, NM 87185

Prof. Vernon F. Cormier
Department of Geology & Geophysics
U-45, Room 207
University of Connecticut
Storrs, CT 06268

Prof. Steven Day
Department of Geological Sciences
San Diego State University
San Diego, CA 92182

Marvin Denny
U.S. Department of Energy
Office of Arms Control
Washington, DC 20585

Dr. Zoltan Der
ENSCO, Inc.
5400 Port Royal Road
Springfield, VA 22151-2388

Prof. Adam Dziewonski
Hoffman Laboratory, Harvard University
Dept. of Earth Atmos. & Planetary Sciences
20 Oxford Street
Cambridge, MA 02138

Prof. John Ebel
Department of Geology & Geophysics
Boston College
Chestnut Hill, MA 02167

Eric Fielding
SNEE Hall
INSTOC
Cornell University
Ithaca, NY 14853

Dr. Mark D. Fisk
Mission Research Corporation
735 State Street
P.O. Drawer 719
Santa Barbara, CA 93102

Prof Stanley Flatte
Applied Sciences Building
University of California, Santa Cruz
Santa Cruz, CA 95064

Dr. John Foley
NER-Geo Sciences
1100 Crown Colony Drive
Quincy, MA 02169

Prof. Donald Forsyth
Department of Geological Sciences
Brown University
Providence, RI 02912

Dr. Art Frankel
U.S. Geological Survey
922 National Center
Reston, VA 22092

Dr. Cliff Frolich
Institute of Geophysics
8701 North Mopac
Austin, TX 78759

Dr. Holly Given
IGPP, A-025
Scripps Institute of Oceanography
University of California, San Diego
La Jolla, CA 92093

Dr. Jeffrey W. Given
SAIC
10260 Campus Point Drive
San Diego, CA 92121

Dr. Dale Glover
Defense Intelligence Agency
ATTN: ODT-1B
Washington, DC 20301

Dr. Indra Gupta
Teledyne Geotech
314 Montgomery Street
Alexanderia, VA 22314

Dan N. Hagedon
Pacific Northwest Laboratories
Battelle Boulevard
Richland, WA 99352

Dr. James Hannon
Lawrence Livermore National Laboratory
P.O. Box 808
L-205
Livermore, CA 94550

Dr. Roger Hansen
HQ AFTAC/TTR
Patrick AFB, FL 32925-6001

Prof. David G. Harkrider
Seismological Laboratory
Division of Geological & Planetary Sciences
California Institute of Technology
Pasadena, CA 91125

Prof. Danny Harvey
CIRES
University of Colorado
Boulder, CO 80309

Prof. Donald V. Helmberger
Seismological Laboratory
Division of Geological & Planetary Sciences
California Institute of Technology
Pasadena, CA 91125

Prof. Eugene Herrin
Institute for the Study of Earth and Man
Geophysical Laboratory
Southern Methodist University
Dallas, TX 75275

Prof. Robert B. Herrmann
Department of Earth & Atmospheric Sciences
St. Louis University
St. Louis, MO 63156

Prof. Lane R. Johnson
Seismographic Station
University of California
Berkeley, CA 94720

Prof. Thomas H. Jordan
Department of Earth, Atmospheric &
 Planetary Sciences
Massachusetts Institute of Technology
Cambridge, MA 02139

Prof. Alan Kafka
Department of Geology & Geophysics
Boston College
Chestnut Hill, MA 02167

Robert C. Kemerait
ENSCO, Inc.
445 Pineda Court
Melbourne, FL 32940

Dr. Max Koontz
U.S. Dept. of Energy/DP 5
Forrestal Building
1000 Independence Avenue
Washington, DC 20585

Dr. Richard LaCoss
MIT Lincoln Laboratory, M-200B
P.O. Box 73
Lexington, MA 02173-0073

Dr. Fred K. Lamb
University of Illinois at Urbana-Champaign
Department of Physics
1110 West Green Street
Urbana, IL 61801

Prof. Charles A. Langston
Geosciences Department
403 Deike Building
The Pennsylvania State University
University Park, PA 16802

Jim Lawson, Chief Geophysicist
Oklahoma Geological Survey
Oklahoma Geophysical Observatory
P.O. Box 8
Leonard, OK 74043-0008

Prof. Thorne Lay
Institute of Tectonics
Earth Science Board
University of California, Santa Cruz
Santa Cruz, CA 95064

Dr. William Leith
U.S. Geological Survey
Mail Stop 928
Reston, VA 22092

Mr. James F. Lewkowicz
Phillips Laboratory/GPEH
Hanscom AFB, MA 01731-5000(2 copies)

Mr. Alfred Lieberman
ACDA/VI-OA State Department Building
Room 5726
320-21st Street, NW
Washington, DC 20451

Prof. L. Timothy Long
School of Geophysical Sciences
Georgia Institute of Technology
Atlanta, GA 30332

Dr. Randolph Martin, III
New England Research, Inc.
76 Olcott Drive
White River Junction, VT 05001

Dr. Robert Masse
Denver Federal Building
Box 25046, Mail Stop 967
Denver, CO 80225

Dr. Gary McCartor
Department of Physics
Southern Methodist University
Dallas, TX 75275

3

Prof. Thomas V. McEvilly
Seismographic Station
University of California
Berkeley, CA 94720

Prof. John A. Orcutt
IGPP, A-025
Scripps Institute of Oceanography
University of California, San Diego
La Jolla, CA 92093

Dr. Art McGarr
U.S. Geological Survey
Mail Stop 977
U.S. Geological Survey
Menlo Park, CA 94025

Prof. Jeffrey Park
Kline Geology Laboratory
P.O. Box 6666
New Haven, CT 06511-8130

Dr. Keith L. McLaughlin
S-CUBED
A Division of Maxwell Laboratory
P.O. Box 1620
La Jolla, CA 92038-1620

Dr. Howard Patton
Lawrence Livermore National Laboratory
L-025
P.O. Box 808
Livermore, CA 94550

Stephen Miller & Dr. Alexander Florence
SRI International
333 Ravenswood Avenue
Box AF 116
Menlo Park, CA 94025-3493

Dr. Frank Pilotte
HQ AFTAC/TT
Patrick AFB, FL 32925-6001

Prof. Bernard Minster
IGPP, A-025
Scripps Institute of Oceanography
University of California, San Diego
La Jolla, CA 92093

Dr. Jay J. Pulli
Radix Systems, Inc.
2 Taft Court, Suite 203
Rockville, MD 20850

Prof. Brian J. Mitchell
Department of Earth & Atmospheric Sciences
St. Louis University
St. Louis, MO 63156

Dr. Robert Reinke
ATTN: FCTVTD
Field Command
Defense Nuclear Agency
Kirtland AFB, NM 87115

Mr. Jack Murphy
S-CUBED
A Division of Maxwell Laboratory
11800 Sunrise Valley Drive, Suite 1212
Reston, VA 22091 (2 Copies)

Prof. Paul G. Richards
Lamont-Doherty Geological Observatory
 of Columbia University
Palisades, NY 10964

Dr. Keith K. Nakanishi
Lawrence Livermore National Laboratory
L-025
P.O. Box 808
Livermore, CA 94550

Mr. Wilmer Rivers
Teledyne Geotech
314 Montgomery Street
Alexandria, VA 22314

Dr. Carl Newton
Los Alamos National Laboratory
P.O. Box 1663
Mail Stop C335, Group ESS-3
Los Alamos, NM 87545

Dr. George Rothe
HQ AFTAC/TTR
Patrick AFB, FL 32925-6001

Dr. Bao Nguyen
HQ AFTAC/TTR
Patrick AFB, FL 32925-6001

Dr. Alan S. Ryall, Jr.
DARPA/NMRO
3701 North Fairfax Drive
Arlington, VA 22209-1714

Dr. Richard Sailor
TASC, Inc.
55 Walkers Brook Drive
Reading, MA 01867

Prof. Charles G. Sammis
Center for Earth Sciences
University of Southern California
University Park
Los Angeles, CA 90089-0741

Prof. Christopher H. Scholz
Lamont-Doherty Geological Observatory
 of Columbia University
Palisades, CA 10964

Dr. Susan Schwartz
Institute of Tectonics
1156 High Street
Santa Cruz, CA 95064

Secretary of the Air Force
(SAFRD)
Washington, DC 20330

Office of the Secretary of Defense
DDR&E
Washington, DC 20330

Thomas J. Sereno, Jr.
Science Application Int'l Corp.
10260 Campus Point Drive
San Diego, CA 92121

Dr. Michael Shore
Defense Nuclear Agency/SPSS
6801 Telegraph Road
Alexandria, VA 22310

Dr. Matthew Sibol
Virginia Tech
Seismological Observatory
4044 Derring Hall
Blacksburg, VA 24061-0420

Prof. David G. Simpson
IRIS, Inc.
1616 North Fort Myer Drive
Suite 1440
Arlington, VA 22209

Donald L. Springer
Lawrence Livermore National Laboratory
L-025
P.O. Box 808
Livermore, CA 94550

Dr. Jeffrey Stevens
S-CUBED
A Division of Maxwell Laboratory
P.O. Box 1620
La Jolla, CA 92038-1620

Lt. Col. Jim Stobie
ATTN: AFOSR/NL
Bolling AFB
Washington, DC 20332-6448

Prof. Brian Stump
Institute for the Study of Earth & Man
Geophysical Laboratory
Southern Methodist University
Dallas, TX 75275

Prof. Jeremiah Sullivan
University of Illinois at Urbana-Champaign
Department of Physics
1110 West Green Street
Urbana, IL 61801

Prof. L. Sykes
Lamont-Doherty Geological Observatory
 of Columbia University
Palisades, NY 10964

Dr. David Taylor
ENSCO, Inc.
445 Pineda Court
Melbourne, FL 32940

Dr. Steven R. Taylor
Los Alamos National Laboratory
P.O. Box 1663
Mail Stop C335
Los Alamos, NM 87545

Prof. Clifford Thurber
University of Wisconsin-Madison
Department of Geology & Geophysics
1215 West Dayton Street
Madison, WS 53706

Prof. M. Nafi Toksoz
Earth Resources Lab
Massachusetts Institute of Technology
42 Carleton Street
Cambridge, MA 02142

5

Dr. Larry Turnbull
CIA-OSWR/NED
Washington, DC 20505

DARPA/RMO/SECURITY OFFICE
3701 North Fairfax Drive
Arlington, VA 22203-1714

Dr. Gregory van der Vink
IRIS, Inc.
1616 North Fort Myer Drive
Suite 1440
Arlington, VA 22209

HQ DNA
ATTN: Technical Library
Washington, DC 20305

Dr. Karl Veith
EG&G
5211 Auth Road
Suite 240
Suitland, MD 20746

Defense Intelligence Agency
Directorate for Scientific & Technical Intelligence
ATTN: DTIB
Washington, DC 20340-6158

Prof. Terry C. Wallace
Department of Geosciences
Building #77
University of Arizona
Tuscon, AZ 85721

Defense Technical Information Center
Cameron Station
Alexandria, VA 22314 (2 Copies)

Dr. Thomas Weaver
Los Alamos National Laboratory
P.O. Box 1663
Mail Stop C335
Los Alamos, NM 87545

TACTEC
Battelle Memorial Institute
505 King Avenue
Columbus, OH 43201 (Final Report)

Dr. William Wortman
Mission Research Corporation
8560 Cinderbed Road
Suite 700
Newington, VA 22122

Phillips Laboratory
ATTN: XPG
Hanscom AFB, MA 01731-5000

Prof. Francis T. Wu
Department of Geological Sciences
State University of New York
 at Binghamton
Vestal, NY 13901

Phillips Laboratory
ATTN: GPE
Hanscom AFB, MA 01731-5000

AFTAC/CA
(STINFO)
Patrick AFB, FL 32925-6001

Phillips Laboratory
ATTN: TSML
Hanscom AFB, MA 01731-5000

DARPA/PM
3701 North Fairfax Drive
Arlington, VA 22203-1714

Phillips Laboratory
ATTN: SUL
Kirtland, NM 87117 (2 copies)

DARPA/RMO/RETRIEVAL
3701 North Fairfax Drive
Arlington, VA 22203-1714

Dr. Michel Bouchon
I.R.I.G.M.-B.P. 68
38402 St. Martin D'Heres
Cedex, FRANCE

Dr. Michel Campillo
Observatoire de Grenoble
I.R.I.G.M.-B.P. 53
38041 Grenoble, FRANCE

Dr. Jorg Schlittenhardt
Federal Institute for Geosciences & Nat'l Res.
Postfach 510153
D-3000 Hannover 51, GERMANY

Dr. Kin Yip Chun
Geophysics Division
Physics Department
University of Toronto
Ontario, CANADA

Dr. Johannes Schweitzer
Institute of Geophysics
Ruhr University/Bochum
P.O. Box 1102148
4360 Bochum 1, GERMANY

Prof. Hans-Peter Harjes
Institute for Geophysic
Ruhr University/Bochum
P.O. Box 102148
4630 Bochum 1, GERMANY

Prof. Eystein Husebye
NTNF/NORSAR
P.O. Box 51
N-2007 Kjeller, NORWAY

David Jepsen
Acting Head, Nuclear Monitoring Section
Bureau of Mineral Resources
Geology and Geophysics
G.P.O. Box 378, Canberra, AUSTRALIA

Ms. Eva Johannisson
Senior Research Officer
National Defense Research Inst.
P.O. Box 27322
S-102 54 Stockholm, SWEDEN

Dr. Peter Marshall
Procurement Executive
Ministry of Defense
Blacknest, Brimpton
Reading FG7-FRS, UNITED KINGDOM

Dr. Bernard Massinon, Dr. Pierre Mechler
Societe Radiomana
27 rue Claude Bernard
75005 Paris, FRANCE (2 Copies)

Dr. Svein Mykkeltveit
NTNT/NORSAR
P.O. Box 51
N-2007 Kjeller, NORWAY (3 Copies)

Prof. Keith Priestley
University of Cambridge
Bullard Labs, Dept. of Earth Sciences
Madingley Rise, Madingley Road
Cambridge CB3 OEZ, ENGLAND